Characterizing the spatial and temporal frequency tuning properties in mouse visual cortex with calcium imaging

Natalia Mesa

A dissertation
submitted in partial fulfillment of the
requirements for the degree of

Doctor of Philosophy

University of Washington
2021

Reading committee:
David Jack Waters, Chair
Frederick Martin Rieke
John Neitz

Program Authorized to grant degree:
Neuroscience

University of Washington

Abstract

Characterizing the spatial and temporal frequency tuning properties in mouse visual cortex with calcium imaging

Natalia Mesa

Chair of Supervisory Committee:
David Jack Waters
Department of Physiology and Biophysics

In the neocortex, neurons with similar functional properties are clustered together. While incompletely understood, this feature of cortical organization is conserved across a variety of species and sensory systems. In the visual cortex, neurons with similar receptive field properties lie close by in cortical space.

The mouse has become an increasingly popular model organism to study vision. While mice lack the visual acuity of primates, there are unparalleled genetic tools available in mice that allow us to dissect the functional properties and connectivity of specific cell types. Mice use vision perform complex behavioral tasks, like hunt, and, like primates, their visual areas are organized hierarchically. While it is likely that mouse visual areas specialized to aid mice in performing visual tasks, there is also evidence that visual computation is different in mice and primates. In particular, visual tuning properties are mapped differently in primates and mice and this likely has relevant functional consequences.

A hallmark of primate vision is the specialization of visual areas. The primate visual system is organized hierarchically such that receptive fields of neurons in higher visual areas become increasingly complex and specific. It is unknown to what extent a similar organization exists in mice. The functional role of mouse higher visual areas, and their homology to primate visual areas, is an active area of investigation. Understanding the differences and similarities between mice and primates is crucial to establishing the mouse as a relevant model organism for primate vision.

Five previous studies have revealed that mouse higher visual areas have distinct spatial and temporal frequency tuning properties than primary visual area, V1. However, their findings have varied widely. Similarly, previous studies have also revealed that functional properties, mainly spatial frequency tuning and coherent motion tuning, change across the visual field, but this is under-characterized. The primary aim of my thesis was to study how receptive field properties are mapped across the mouse visual cortex and how tuning properties change across the visual field. The next is to understand how experimental conditions and experimental design choices can lead to different tuning measurements between studies.

In my first project, I used a combination of widefield and 2-photon (2P) calcium imaging to investigate how spatial frequency (SF) and temporal frequency (TF) tuning properties are mapped in the mouse visual cortex. I found evidence of functional specialization at different receptive field altitude locations in V1 and higher visual areas. Neurons in anterior V1 (lower visual field of view) have lower average TF and SF tuning than posterior V1 (upper visual field of view). I measured whether tuning gradients, gradual changes in tuning properties across a visual area or areas, in V1 and higher visual areas were consistent across cortical layers and in thalamic (dLGN) axons. In most visual areas, gradients had the same slope with respect to altitude. Interestingly, I found TF gradients that did not change abruptly across areal borders. While TF tuning differed across cortical layers, the relationship between TF and altitude was consistent across laminar populations and in dLGN axons. Therefore, gradients in V1 and some higher visual areas likely result from input from dLGN axons.

In my second project, I examined how different inclusion criteria can impact reported tuning properties. Neurophysiology studies require the use of inclusion criteria to identify neurons responsive to the experimental stimuli. Five recent studies used calcium imaging to measure the preferred tuning properties of layer 2/3 pyramidal neurons in mouse visual areas. These five studies used different experimental designs that employed different inclusion criteria and report different, sometimes conflicting results. Experimental design choices and inclusion criteria both affect the subpopulation of neurons that are selected for. Here, I examined how different inclusion criteria can impact reported tuning properties, modifying inclusion criteria to select different sub-populations from the same dataset of almost 17,000 layer 2/3 neurons from the Allen Brain Observatory. The choice of inclusion criteria greatly affected the mean tuning properties of the resulting sub-populations; indeed, the differences in mean tuning due to inclusion criteria were often of comparable magnitude to the differences between studies. In particular, the mean preferred TFs of visual areas changed markedly with inclusion criteria, such that the rank ordering of visual areas based on their TF preferences changed with the percentage of neurons included. These results demonstrate that the current understanding of the functional organization of the mouse visual cortex obtained from previous experiments critically depends on the inclusion criteria used.

Collectively, my research has advanced our understanding of visual processing in the mouse.

To my family and friends

TABLE OF CONTENTS

1. INTRODUCTION

An organizing principle of the neocortex is that cells with similar response properties are clustered together in cortical space. While incompletely understood, these maps likely serve some role in processing sensory information. The goal of my thesis is to characterize functional maps in the mouse visual cortex.

In this introduction, I will first provide a brief overview of the mammalian visual system and visual cortex (section 1). Then, I will describe the functional maps in visual cortex (section 2), address how these maps come about (section 3) and their purpose (section 4), before introducing my aims (section 5).

1.1 VISUAL INFORMATION IS PROCESSED IN THE VISUAL SYSTEM

1.1.1 DEFINITION OF 'VISUAL AREA'; RETINOGENICULATE AND RETINOCOLLICULAR PATHWAYS.

The mammalian visual system is responsible for encoding, synthesizing, and distributing visual information. In most mammals, information travels from the retina to early visual cortical areas via two routes. In the retinogeniculate pathway, the retina converts light into electrical signals, which travel to the lateral geniculate nucleus (LGN) of the thalamus, then to the primary visual cortical area, V1, then to the extrastriate visual areas (Merrigan & Maunsell, 1990). In the retinocollicular pathway cells in the retinal signal to the superior colliculus in the tectum, which then signal to the lateral pulvinar (LP) nucleus of the thalamus (Abrahamson & Chalupa, 1988). In primates, this information is then passed via a disynaptic pathway to some extrastriate visual areas: MT and V3 (Lyon et al., 2010). Similarly, in mice, only extrastriate visual areas receive pulvinar projections (Tohmi et al., 2010).

Historically, researchers have used a combination of lesioning, electrical stimulation, and electrophysiological recording experiments to describe which cortical regions are visually responsive. Brain areas are considered visual areas if they: (1) contain cells that respond to light and (2) produce the sensation of light if they are stimulated. Researchers first observed that lesions in the caudal part of the brain, in the occipital lobe, resulted in visual deficits (Munk, 1881; Henschen, 1890), leading them to the conclusion that the occipital lobe is necessary for processing visual information. Later, electrical stimulation and electrical recording of visual activity in primary visual cortex areas and extrastriate visual areas lead researchers to map the representation of the visual field in various parts of cortex (Bard, 1938; Daniel and Whitteridge, 1961). This led to the discovery that visual space is topographically organized in the cortex.

The visual cortex is divided into several visual areas, defined as groups of retinotopographically organized somata (Van Essen, 1970), meaning that cells that are physically close together receive input from regions close by in the visual field. Neurons are also organized functionally, such that neurons with similar functional properties are clustered together in space (Van Essen & Felleman, 1997; Desimone & Gross, 1979).

1.1.2 HISTORICAL DEVELOPMENT AND BASIS OF VISUAL AREAS

Most of what is known about vision comes from studies in primates and domesticated cats. In primates, the first maps delineating visual areas were based on section drawings published by Brodmann (1905). Further studies divided the visual cortex based on connectivity patterns and myeloarchitecture (Van Essen & Felleman, 1991). A combination of architecture (chemoarchitecture, cytoarchitecture, and myeloarchitecture), topographic organization, connectivity, and visual responsiveness (Van Essen et al., 1986; Roland et al., 1997; Saad et al., 2001) has advanced the contemporary understanding of visual area borders in cats and primates. Human cortical areas are broadly thought to be similar to non-human primate cortical areas, but since scientists are limited in the methods that are typically used to describe these areas, they are typically defined using fMRI. Considerable homologies have been found between human and primate areas (Orban et al., 2004).

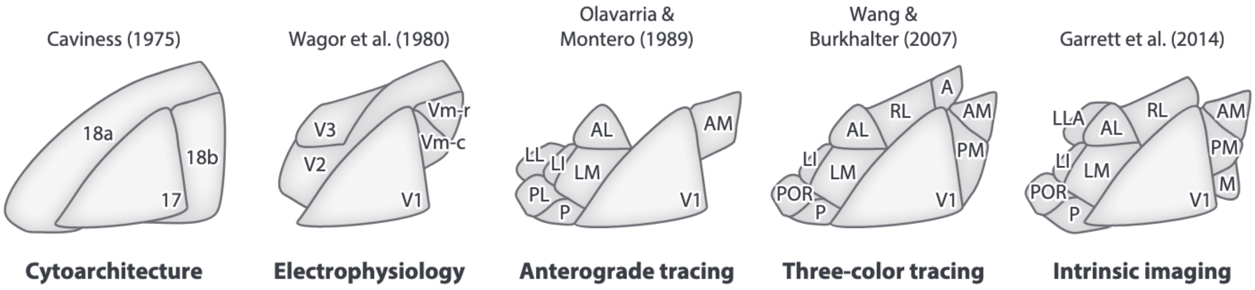

Figure 1. Schematic of landmarks in the parcellation of the mouse higher-order visual areas. Author(s), year, and method used to define the map are noted for each map. Abbreviations: A, anterior; AL, anterolateral; AM, anteromedial; LI, laterointermediate; LL, laterolateral;LLA, laterolateral anterior; LM, lateromedial; M, medial; P, posterior; PL, posterolateral; PM, posteromedial; POR, postrhinal; RL,rostrolateral; V1, primary visual cortex; V2, visual area 2; V3, visual area 3; Vm-c, medial visual area, caudal subdivision; Vm-r, medialvisual area, rostral subdivision. From Glickfeld & Olsen (2017).

Early on, mouse higher visual areas were defined cytoarchitectonically (See **Figure 1**). This technique parcellated cortex coarsely into ~5 visual areas (Caviness et al., 1975; Paxinos & Franklin, 2000). Later, electrophysiological recordings and tracer injections were used to further describe the map of visual areas. Multi-color tracer injections in multiple parts of V1 revealed the retinotopic organization of V1, the way in which this map reversed at the border of V1 and extrastriate or higher visual areas (HVAs), the retinotopically organized connectivity between V1 and higher visual areas, and the retinotopic organization of eight higher visual areas (Wang et al., 2011, Wang et al., 2012, Olivarria and Montero, 1989). Higher visual areas are visual areas outside of V1 that contain maps of retinotopic space. Recently, mesoscale imaging techniques, such as widefield calcium imaging and intrinsic imaging, have afforded researchers higher signal and resolution and therefore the ability to sample all visual space, allowing them to more accurately describe borders between visual areas. Currently, 12 mouse visual areas, each with a map of the retinotopic field, have been described.

1.1.3 RECEPTIVE FIELD PROPERTIES ARE MAPPED IN CORTEX

Neurons with similar functional properties are clustered in the mammalian visual cortex. Spatial frequency (SF), temporal frequency (TF), and orientation are fundamental stimulus features that are often used to classify response properties of neurons. For periodic stimuli, SF, measured in cycles per degree, is a measure of the spatial period. TF, measured in cycles/second, describes the time taken for a stimulus to move through one complete cycle (Robson, 1966). Orientation selectivity is the preference for where a stimulus is radially oriented in space, typically measured in degrees from 0 to 360 degrees. Neurons in V1 are thought to be specialized to detect these features, but these features have also been useful for interrogating the function of extrastriate visual areas in primates and mice (Forster et al., 1985). Therefore, I will focus the majority of this introduction on how SF, TF, and orientation change across and between cortical visual areas.

Maps in the visual cortex can be characterized into two types: those which respect retinotopic borders, wherein tuning changes abruptly at the border between areas, and those that exist independent of retinotopic borders, such as local maps or tuning properties that change gradually across the visual cortex. I will describe each type of map in this context further in this introduction.

1.2 MAPS OF FUNCTIONAL PROPERTIES

1.2.1 NEURONS WITH DIFFERENT FUNCTIONAL PROPERTIES ORGANIZED BY STREAMS IN PRIMATES

How are functional properties, such as SF, TF, and orientation mapped across cortex in primates and other higher mammals? Neurons encode information that is related to the stream they belong to. The ventral stream areas function primarily to detect and encode form and color information, while dorsal stream areas function primarily to detect and encode motion (Ungerleider and Mishkin, 1992). For example, area V4, a ventral stream area, is primarily thought to detect contour and shape (Popovkina et al., 2019), while MT, a dorsal stream area, is primarily thought to detect speed and has a large number of direction-selective neurons (Born & Bradley, 2005). Dorsal stream areas tend to have a higher TF tuning, and less SF and TF separability (Priebe et al., 2006; Perrone & Thiele, 2001). This means the preferred TF of the stimulus changes depending on SF of the stimulus, and the preferred speed decreases as a function of SF. The SF-TF combinations that elicit an equal response in this case fall along a tilted axis where speed remains constant. There is a higher number of pattern selective cells in dorsal stream area MT (Rust et al., 2006). I go into the parallel structure of the primate visual cortex in detail in section **1.2.2.**

In the ventral stream, mapping the SF tuning preferences of neurons is more involved. Since the visual receptive field properties of these neurons are more complex, simple sine wave static grating stimuli may not readily drive robust responses in these neurons. The complex images that drive responses in ventral stream cells contain a combination of SFs. Nevertheless, human fMRI recordings of ventral stream visual areas reveal that visual areas have unique SF preferences that can be correlated to their purported function. This group presented images such as faces and trees with the high and low SF information filtered out and found that face and body selective regions show a preference for low SFs while general object selective regions show a preference for high SFs (Canário et al., 2016). Macaque laminar recordings have shown that in V4, high SF information is preserved, and there exist high SF functional domains which violate the inverse relationship between retinal eccentricity and SF, indicating that high SF information is preserved in V4, and that these cells are clustered together (Lu et al., 2018).

1.2.2 HOW PARALLEL AND HIERARCHICAL ORGANIZATION ARISES IN PRIMATES

In primates, the parallel organization begins at the retina. In the primate retina, there are 15-20 RGC types (Rodieck & Watanabe, 1993; Dacey et al., 2003) that communicate parallel representations of the visual field to the brain via the LGN of the thalamus. The most numerically dominant types are retinal ganglion cell types (RGC) are midget retinal ganglion cells (also known as P cells), parasol cells (also known as M cells), and small bistratified cells. Less than half the morphologically-identified cells in the primate retina have been characterized physiologically, but constitute only a small fraction (1-4% of all primate retinal ganglion cells [Dacey et al., 2004]). Midget cells are the basis of the parvocellular pathway and synapse primarily onto neurons in the parvocellular layers of the thalamus (layers one through four) (Jusuf et al., 2006). Parasol cells are the basis for the magnocellular pathway and synapse primarily onto neurons in the magnocellular layers of the thalamus (layers five and six) (Dacey & Peterson, 1992). Small bistratisfied cells synapse onto koniocellular neurons in the LGN, onto the intercalated layers of the LGN. The parvocellular pathway is hypothesized to primarily innervate ventral stream areas while the magnocellular pathway is hypothesized to primarily innervate the dorsal stream areas (Maunsell et al., 1990). Cats are thought to have a similar magnocellular/parvocellular distinction, where the magnocellular-like Y cells and parvocellular-like X cells carry parallel representations of the visual field to the cat visual cortex, although homology between the two species remains contentious (Shapley, 1986).

Parasol cells tend to have larger dendritic field sizes and larger responses to luminance changes than midget ganglion cells (Dacey & Peterson, 1992; Watanabe & Rodieck, 1989). Midget ganglion also get more input from fewer-color sensitive cones in the retina (and at the fovea, only one cone), while individual parasol cells get more input from comparably more cones (Dacey, 1993; Maunsell et al., 1990). Further, midget cells sum linearly over their receptive fields, while some parasol cells sum nonlinearly over their receptive fields. It is hypothesized that midget cells contain form and red-green color information (Schiller et al., 2010), while parasol cells contain more precise temporal information to aid in the processing of motion signals (Manookin et al., 2018).

Koniocellular cells of the LGN are thought to receive more heterogeneous input and have heterogenenous receptive field properties than parvocellular or magnocellular cells, including color-coding blue-on and blue-off cells, suppressed by contrast cells, and orientation selective cells, and on/off cells (Szamajda et al., 2005; Solomon et al., 2010).

Magnocellular and parvocellular pathways have different response properties and remain functionally segregated throughout multiple stages of cortical processing. Magnocellular cells have a higher cutoff TF and lower SF preferences than parvocellular neurons (Skottun et al., 2016; Skottun et al. 2000, 2015; Skottun & Skyles, 2007), which has led researchers to believe that Layer 4B and downstream projections are specialized to detect motion. Layer 4B projects to CO interblobs and thick stripes, both of which are characterized by the presence of cytochrome oxidase, in V2, while Layer 2/3 projects to largely thin stripes in area V2, which are thought to be specialized to detect color and form information. The segregation continues as thick stripes of area V2 project to dorsal stream areas such as MT and MST, and thin Stripes of area V2 project to ventral stream areas, mainly V4, and IT cortex.

There is thought to be a similar parallel organization in the cat. The magnocellular and parvocellular retinal ganglion cells of the primate have been likened to X and Y cells in the cat, due to their morphology and some similarities between their receptive field properties. X cells are comparably smaller than Y cells and sum linearly over their receptive fields, while in Y cells the summation is largely nonlinear (Shapley, 1981). However, whether X and Y cells are homologous to M and P cells remains contentious.

1.2.3 SF AND TF TUNING DIFFERS BETWEEN AND ACROSS MOUSE VISUAL AREAS

There are five studies that have established that spatiotemporal frequency tuning properties of neurons in higher visual areas are different than those of neurons in V1. The tuning properties of HVAs also differ between one another.

Five studies have sampled the center of gaze of up to seven visual areas, though most studies have sampled three or less. All studies used 2-photon (2P) calcium imaging and measured responses to drifting gratings (Tohmi et al., 2014; Roth et al., 2012; Marshel et al., 2011; Andermann et al., 2011; Glickfeld et al., 2013).

There are some consistencies across studies. All studies that measured the tuning of higher visual areas AL and RL found that neurons in these areas prefer higher average TF and a lower SF than those in V1. TF values in AL range from 1.2-fold (3 Hz vs 4 Hz) to roughly 3-fold (1.2 Hz vs 3 Hz) higher than V1 (Tohmi et al., 2014; Roth et al., 2012; Marshel et al., 2011; Andermann et al., 2011; Glickfeld et al., 2013).

Area PM, for example, has a similar spatiotemporal tuning to V1 in two studies: 0.25 and 0.69 Hz V1 versus 0.5 and 0.8 Hz in PM, respectively, and two-fold higher TF tuning than V1 in one study. PM has been found to have similar SF tuning to V1. There is a putative hierarchy in TF and SF tuning, where V1 and PM have low TF tuning, and higher visual areas AL, RL, and LM have higher TF tuning.

However, the reported values of the average TF tuning in a visual area differ by up to six-fold across studies; for example, the mean TF tuning in V1 ranges from 0.5 to 3 Hz. This may be because of a combination of the different anesthesia states, calcium indicators, and stimulus parameters, and inclusion criteria used in these studies. The topic of inter-study differences is addressed at length in **CHAPTER 3** of this thesis.

The distinct spatiotemporal tuning properties of mouse visual areas might suggest that extrastriate areas are functionally specialized. For instance, areas may be specialized to detect stimuli which move faster across the visual space (high TF) or larger, more coarse stimuli (low SF).

There are maps of SF tuning across elevation in the mouse. The upper portion of the visual field has higher SF tuning than the lower portion of the visual field (Rhim et al., 2017). It is not currently known whether different portions of the mouse visual fields are tuned to different temporal frequencies or speeds, or whether they exhibit larger degrees of speed tuning.

There is an implicit assumption that different visual areas have different functional tuning, and therefore that functional properties change across areal borders (Tohmi et al., 2014; Roth et al., 2012; Marshel et al., 2011; Andermann et al., 2011; Glickfeld et al., 2013). This assumption is consistent with primate studies.

Although the primate visual cortex has not been sampled uniformly for SF and TF properties, the central and peripheral portions of V1 perform similar hierarchical computations (Levy et al., 2001). In addition, retinotopy and receptive field size change abruptly in area borders in both primates and mice (Pettett & Gilbert, 1992; Pinon et al., 1998).

1.2.4 IN MICE, PARALLEL STRUCTURE HAS NOT BEEN FOUND

In the mouse retina, no clear magnocellular/parvocellular distinction has been observed. There are 38 classes of retinal ganglion cells. Many mouse RGC types have not been observed in the primate, including direction selective, local edge detectors, and orientation selective cells. There are also chromatically sensitive in the mouse retina and cells center-surround opponent structure commonly observed in primates, cats, rabbits, and several other species: alpha and beta retinal ganglion cells (O'Brien et al., 2002; Coombs et al., 2006). These cell types were first observed in the cat, but the homology between cat and mouse alpha and beta ganglion cells in unclear. In the mouse, currently alpha RGC are classified into four types based on morphology and physiological properties (Pang et al., 2003): sustained ON, sustained OFF, transient ON, and transient OFF RGCs (Krieger et al., 2017). So far, it is unclear whether these two morphological types, alpha and beta retinal ganglion cells, perform similar functions of the other species, and whether they have any substantial effect on the visual properties downstream.

There is some evidence of parallel information flow in the mouse dLGN. As in the optic nerves of cats and primates, mice have multiple conduction velocity groups after optic chiasm stimulation. There is a subpopulation of mouse dLGN neurons that exhibit nonlinear spatial summation, like parasol cells/Y cells, while most show linear spatial summation, like midget cells/X cells (Piscopo et al., 2013; Gao et al., 2010). However, these two groups do not show differences in stimulus selectivity, and linearity of spatial summation does not correlate with spatial or temporal selectivity or contrast sensitivity as it does in primates and cats (distinguishing this way requires controlling for receptive field eccentricity, which is difficult to do afoveate animals such as mice).

Initial evidence for parallel organization of the mouse cortex comes from architectonic studies. Wang et al. (2012) examined the network connectivity of the HVAs and their downstream projections across the cortex. By clustering the connectivity profiles of the HVAs, the authors identified two major submodules. One module, analogized to the ventral stream, includes areas LM, LI, P, and POR. In addition to being strongly interconnected, these areas provide strong output to ventral regions of the cortex, including temporal association areas and the entorhinal cortex, implicated in memory and object identification functions. The other, dorsal module includes areas AL, RL, PM, AM, and A and provides outputs to areas involved in navigation, spatial processing, and movement, including the retrosplenial, anterior cingulate, and secondary motor cortices.

Recent work on connectivity and timing differences has refined this hierarchy. The most comprehensive study to date (Harris et al. 2019) used data from the Allen mouse connectivity Atlas, which involved a thousand experiments in cortex and thalamus in conjunction with Cre driver lines to comprehensively and selectively label brain wide connections by the layer and cross of the project in neuron. This study assigned a hierarchy score using an optimization algorithm that considers the set of distinct axonal termination patterns of connectivity between areas, assigns interconnection as either feedforward or feedback, finding the most self – consistent network architecture. Unsurprisingly, LGN is at the bottom of this hierarchy, followed by its major target structure, V1. Higher-order visual areas LM, RL LP and AL are intermediate in the hierarchy. Areas PM and AM occupy the top level of the hierarchy. Still, Harris at all went on to say that this was a relatively shallow hierarchy where the lowest and highest levels are separated only by a few rungs., A similar data intensive study (Siegel et al., 2021)) sought to confirm the existence of the functional hierarchy using dense multiunit recordings and eight cortical and subcortical visual areas, using a combination of response metrics traditionally used design hierarchy and primates (latency of responses, receptive field size, modulation index, and temporal scales the response) to assign hierarchy. This analysis indicated distinct hierarchical levels starting with LGN in V1, followed by LM and RL, then LP, AL, and finally PM and AM at the highest level, agreeing somewhat the results from Harris et al. 2019. Siegel et al. (2021) found functional evidence of a hierarchy, there is still substantial overlap in the distribution of response properties across areas: some neurons in LGN spiked after those in AM for example.

Though there is evidence for a hierarchy of visual areas in mouse visual cortex, it is clearly different from the parallel and hierarchical processing performed in primate visual cortex. Instead, the mouse visual cortex is a highly interconnected structure with relatively ‘shallow’ hierarchy compared to primates, wherein V1 projects to all HVAs, which in turn are all interconnected (Harris et al., 2019). The shallowness of this hierarchy might be due to incomplete information in the mouse. Researchers have failed to find physiological evidence that certain areas in mouse visual cortex are specialized to make the types of hierarchical computations found in the ventral stream such as form and color processing. There is currently evidence that mouse visual cortex does make some hierarchical computations akin to those found in the dorsal stream, this processing seems to be distributed across multiple visual areas (Juavinett & Callaway, 2015). As such, there are two options: either functional hierarchy exists I have not interrogated with current methods, or hierarchical computations are processed in a distributed manner.

1.2.5 FUNCTIONAL SPECIALIZATION OF MOUSE VISUAL AREAS COULD BE DUE TO FUNCTIONALLY SPECIFIC PROJECTIONS FROM V1, OR FROM COLLICULAR INPUT

TF tuning provides an example of functional specialization of mouse visual areas. Currently, there are two competing theories for how mouse higher visual areas develop their unique TF tuning characteristics. One theory posits that functionally specialized projections from V1 to higher visual areas are responsible (Glickfeld et al., 2012). Glickfeld et al. made targeted injections of a viral vector containing GCaMP6 into V1 and imaged projections in higher visual areas with 2P calcium imaging. They found that projections were target specific — projections into higher visual areas with high TF tuning had high TF tuning. Thus, in this model, V1 neurons have a large range of tuning preferences. Only neurons with higher TF tuning in V1 project to areas with higher TF tuning and vice versa for low TF tuning. The same is true for SF tuning. Another theory posits that the high TF tuning found in higher visual areas is due to input from the lateral posterior nucleus of the thalamus (LP). When LP is lesioned, higher visual areas lose their higher TF tuning properties. Thus, in this model, the main source of functional specialization in mouse visual cortex is hypothesized to be LP (Tohmi et al., 2010). If input from LP was the main reason why neurons in extrastriate visual areas have higher TF tuning, this might suggest that these areas are specialized to guide visually-guided movements and movement of the animal in space, as this is the primary function of LP.

These two hypotheses are fundamentally incompatible since they posit that the higher TF tuning in mouse visual cortex is primarily due to input either the retinogeniculate pathway via V1 or the retinocurricular pathway via LP. The hypothesis given by Glickfeld et al. (2012) is more compelling, due to the Tohmi et al. (2010) hypothesis relying on the complete ablation of V1, which may drastically alter the circuit in mouse visual cortex and alter functional properties.

1.2.6 HIERARCHICAL COMPUTATIONS IN MOUSE

In primates, there are higher visual areas that are specialized for hierarchical transformations. Evidence that there are distinct areas in the mouse visual cortex that are specialized to perform hierarchical computations found in primate visual cortex, such as form encoding, is scarce. Still, there is evidence that some mouse visual areas are specialized. For example, area RL is tuned for binocular disparity (La Chioma et al., 2020). Area PM is thought to be specialized to encode global features of the visual scene since neurons in PM have significantly larger receptive field sizes and surround-suppression than V1, LM, or AL. These studies suggest that some stimulus features may be processed specifically by some mouse extrastriate visual areas and not others.

While there may be specialized visual areas in the mouse extrastriate cortex, in the mouse, neurons that perform hierarchical transformations are found in many visual areas. Pattern selective receptive fields like those typically found in MT have been found in small numbers in V1 and other HVAs. Pattern-selective receptive fields are spatiotemporally inseparable — they respond selectively to the vector sum of two overlapping gratings rather than to the individual components. Thus, in mice, no individual higher visual area appears to be specialized for encoding pattern motion (Douglas et al., 2006; Juavinett & Callaway, 2015). Other hierarchical transformations, such as areas that are specialized for shapes, have yet to be found. Possibly, these transformations are distributed across multiple areas and visual information processing is more distributed across areas in mice than in primates.

Further evidence for distributed rather than discrete mapping of functional properties comes from the extensive interconnectivity of mouse visual cortical areas: essentially all visual areas project to all other visual areas (Gamamut et al., 2018). Evidence of stark differences between higher visual areas has eluded researchers and in fact during navigational behavioral tasks, all visual areas encode all behaviorally relevant variables (Minderer et al., 2019). This is again evidence for distributed encoding of stimulus features.

1.2.7 DIFFERENCES IN THE FUNCTIONAL PROPERTIES IN DIFFERENT PARTS OF THE VISUAL FIELD

The previous sections have addressed the functional organization of stimulus properties in the visual cortex, with particular attention given to functional specialization of visual areas. However, there are differences in functional properties within visual areas (Rosenholtz et al., 2002). This section focuses on maps of functional properties on this smaller scale.

In primates, acuity and therefore SF preference changes across V1 due to the presence of the fovea. In the center of the visual field, at the fovea, a very large number of neurons process information from a small number of degrees of visual angle (Brinkmann et al., 2018; Krebs & Krebs, 1989). This area is specialized to detect fine spatial detail, compared to the relatively coarse acuity of the periphery of the visual field.

There are functional differences across visual areas that aren’t related to the fovea. Studies in marmoset have shown no difference in the TF tuning and preferred SF preference between central and peripheral V1 once cortical magnification (the factor that describes how many neurons are responsible for processing a stimulus of a given size or how many millimeters of cortical surface correspond to a degree of visual angle) is accounted for (Chaplin et al., 2013). However, SF tuning curves in the periphery of V1 cells have a narrower bandwidth than those in the center. In addition, the number of cells displaying significant spatiotemporal interactions is greater in the periphery (Yu et al., 2010).

In other mammals, such as cats, dogs, ferrets, and other carnivores, there is no fovea but there is an area of high acuity called a visual streak, which is a high-density line of vision which contains roughly 2 times as many rods and five times as many cones of the peripheral visual field. Some rodents such as the rabbit also have a visual streak (Habot-Wilner et al., 2011; Beltran et al., 2014). This similarly translates to regions of comparably high SF tuning in V1 and HVAs.

In the diurnal rodent, *Octodon degus,* which has a high proportion of cones and a visual streak, RGCs with peripheral receptive fields are larger, faster, and show more transient responses. Peripheral RGCs also show higher sensitivity to high TF stimuli and at a full frequency bandwidth when compared to the central retina.

In the mouse different RGC types are clustered at different retinal locations, while in primates, cats, and other mammals with a fovea or visual stream, all RGC types are concentrated in one location. Mice do not have a fovea or visual streak (Drager & Hubel, 1976), the distribution of some retinal ganglion subclasses differs depending on the retinotopic location. For example, mouse ON-sustained alpha-like retinal ganglion cells are more densely expressed in the upper nasal retina (Bleckert et al., 2014). The higher sampling frequency by retinal ganglion cells in this area may give neurons downstream higher SF to properties. Several other ganglion cell classes are similarly unequally distributed across the retina. Directionally selective RGCs and W3 cells are more densely expressed in the ventral retina (upper visual field).

Besides the functional specialization caused by differences in the density of photoreceptors at the level of the retina, another example of specialization of certain parts of the visual field is the mouse binocular zone (Scholl et al., 2013; Haworth et al., 2014). Unlike primates, cats, and ferrets, the binocular zone in mice occupies only 10 degrees of visual angle in the most nasal portion of the visual field (Bhamuk & Shah, 2014). In the mouse binocular zone, responses to visual stimulation in the contralateral visual field are more directionally selective that ipsilateral responses and are more strongly biased to cardinal directions. They are also strongly biased toward high SF tuning (Salinas et al., 2017).

Features beyond orientation tuning and spatiotemporal tuning exist within visual areas. For example, maps of disparity tuning also exist within V1 and RL. Disparity is also related to visual field elevation, wherein neurons with receptive fields in the upper visual field are tuned for more positive (far) disparities, while the opposite is true for lower elevations (La Chioma et al., 2019).

1.2.8 LOCAL FUNCTIONAL MAPS EXIST IN PRIMATES AND CATS

There are maps in the visual cortex that do not depend on where in the retinotopic field visual responses are sampled from, creating a local microarchitecture that tiles across the visual field. Sampling from the entire visual field has revealed this microarchitecture in primates. One example is orientation and SF maps. In the visual cortex, primates (Hubel el al., 1978), ungulates, cats (Wood, 1999; Sengpiel et al., 1999), and tree shrews, response properties such as orientation, direction, and SF preference change gradually across the cortical surface, forming two-dimensional maps (Bonhoeffer et al., 1991; Obermayer et al.,1997; Garg et al., 2019). In these animals, patches of cortex respond best to one orientation, and these iso-orientation patches are organized around “orientation centers,” producing pinwheel-like patterns on the cortical surface. In the axis perpendicular to the cortical surface, neurons are also clustered by their functional properties; throughout the cortical layers, neurons have the same orientation preference. These organization modules are called cortical orientation columns and have been described in carnivores and primates (Hubel & Wiesel 1972; Payne & Berman, 1983).

Another canonical example of functional clustering in cortex are ocular dominance columns in V1. In the primary visual cortex, neurons preferring visual stimulation coming into one eye are grouped into columns (Hubel & Wiesel, 1962). These columns do not seem to be present in rodents (Gordon et al. 1996; Flogel et al., 2007), likely do to the fact that they have little binocular vision.

In cats and primates, functionally distinct columnar modules are often described in relation to cytochrome oxidase (CO) staining. Cytochrome oxidase (CO) is a marker of neural activity and is spatially and functionally related to a number of cortical features. Cytochrome oxidase staining is thought to be one of the features of the parallel organization in primate and carnivore visual cortex. In primate visual cortex, the receptive field properties of neurons within blobs (cylindrical sections of the visual cortex that are stained by cytochrome oxidase and a sensitive to color) are less orientation selective and prefer lower SFs (Horton, 1984, Horton & Hocking, 1996; Livingstone & Hubel, 1984a; Tootell et al., 1988, Born & Tootell, 1991). Similarly, in cats, neurons within blobs tend to have low SF, high TF, and low orientation selectivity (Hübener et al., 1997). The same modules have not been found in rodents, potentially signifying a lack of parallel processing of form and motion.

1.2.9 LOCAL FUNCTIONAL MAPS IN RODENTS

Initial experiments sampling continuously across visual areas has revealed that, at least on a local scale, orientation is arranged in an apparently random manner, a so-called salt and pepper fashion. Curiously, this feature cannot be attributed to how visual these animals are, as the grey squirrel (which relies on vision for navigation and localization of food sources and has relatively high visual acuity) doesn't possess orientation maps (Van Hooser, 2005). This has left the purpose of orientation maps unclear. However, spatial clustering of orientation tuning has been found on the cortical surface as well as across different cortical depths in mice at a larger spatial scale than in primates and not in the same pinwheel-like structure as in primates (Ringach et al., 2016). Likewise, SF tuning depends on receptive field elevation, wherein neurons in the upper portion of the visual field have higher SF tuning. The functional organization in mice, rather than consisting of cortical columns, is more spatially diffuse and gradual across the visual field. This again points to the fact that gradual changes in tuning across the mouse visual cortex, rather than discrete regions that have specific tuning properties, are common in mice.

Sampling continuously across the visual cortex has revealed maps of functional properties that change gradually across the visual cortex, and do not change abruptly across area borders. A few studies in mice have done this. In mice, the lower part of the visual field shows comparably larger responses of the upper part of the visual field to coherent motion stimuli. There is a global map of motion in the mouse visual cortex such that anterior has higher visual areas of higher sensitivity for coherent motion (Minderer et al., 2019). There is also evidence that behaviorally relevant variables during visually guided navigation are functionally mapped in posterior cortex, but do not follow previously identified retinotopic borders. These behaviorally relevant variables included features of the stimulus, such as the time since last reward or the linear and angular optic flow of the stimulus. Other groups have also found that visual features such as orientation discrimination and contrast detection are distributed across multiple visual areas, as silencing multiple visual areas can affect both (Jin & Glickfeld, 2019). Thus, neurons that encode certain visual features may be distributed throughout the cortex across multiple visual areas. Which properties in mouse visual cortex change abruptly across area borders and which do not?

1.2.10 DIFFERENCES IN THE FUNCTIONAL PROPERTIES ACROSS THE MOUSE VISUAL FIELD MIGHT BE DUE TO DIFFERENCES IN DENSITY OF CONES, RETINAL GANGLION CELLS ACROSS VISUAL CORTEX

SF and TF tuning has been used to distinguish between and interrogate the parallel streams of information in primates and cats (Kristensen et al., 2016; Mahon et al., 2013). As little is known about the parallel and hierarchical organization of mouse visual cortex, many groups have investigated whether different mouse visual areas are tuned to SF and TF frequencies. Although differences have been found, the same columnar architecture found in primates has not (Ringach et al., 2016). However, stimulus features such as orientation tuning are grouped in the cortex although in a more diffuse way than in primates. Are other fundamental stimulus features that have been found to be grouped in cortical hypercolumns in other species, mainly SF and TF, also functionally clustered in mice?

Differences in the functional properties across primate visual cortex are due to the presence of the fovea, and this directly translates to differences in SF tuning across V1. In other carnivores and rabbits, the region known as the visual streak serves a homologous function (Vaney et al., 1980). There is some evidence that mice have a fovea like region as well, which could result in parts of the mouse visual fields having higher acuity in some parts of the visual field. The population receptive field size of neurons in V1 are smaller in the binocular zone. Also, there are different distributions of retinal ganglion cell types across the retina. On and off alpha retinal ganglion cells are more densely expressed in the nasal portion of the visual fields, also corresponding to the mouse binocular zone (Bleckert et al., 2014).

Gradual changes in SF and TF frequency tuning across the visual field may be due to differences in the distribution of color opsins in the mouse retina. Based on the distribution of opsins in the mouse retina, one sees that cells in V1 have different response properties to different colors of light. Although mice have many retinal ganglion cell types, they only have two cone types: the UV sensitive S cone and the visible light sensitive M cones (Umino et al., 2008). One might predict that neurons in the one region may have different functional properties based on their corresponding cone type and distinct functional properties. For example, S cones have higher temporal frequency tuning than M cones (Wang et al., 2011).

1.2.11 GLOBAL MAPS MAY COME FROM SMOOTH ANATOMICAL AND CYTOARCHITECTONIC GRADIENTS

Although retinotopic maps in different mouse visual areas suggest discrete areas, there are cases where smooth anatomical and cytoarchitectonic gradients have been found in mouse visual cortex (Allen Institute, 2017; Gamaut et al., 2018). These are likely the basis of maps of functional properties in the mouse visual cortex that do not obey area borders. Such maps have not been described in primates but may give us a clue as to why and how certain regions of the visual cortex are functionally specialized.

1.3 PURPOSE OF MAPS

1.3.1 FUNCTIONAL SPECIALIZATION OF MOUSE VISUAL AREAS COULD AID IN VISUAL BEHAVIORS

Though the visual abilities of primates far surpass those of mice, mice engage in a number of visual behaviors including orientation toward prey (Hoy et al., 2016), distinguishing between stationary and moving objects (Braida et al., 2013), distinguishing signals embedded in noise (Stirman et al, 2016), and can make associations between visual stimuli and reward (Burgess et al, 2016). It is feasible that mouse higher-order visual areas are specialized to allow them to perform these behaviors and though the functions of mouse HVAs remain largely unknown, there is evidence for functional specificity of HVAs.

1.3.2 FUNCTIONAL SPECIALIZATION ACROSS THE VISUAL FIELD COULD AID IN DETECTION OF PREDATORS, NAVIGATION

The anterior region of visual cortex, which corresponds to the upper part of the visual field, has higher SF tuning than the anterior portion and might be specialized for predator detection (detection of animals such as birds in the visual field) (Rhim et al., 2017).

Certain parts of the visual field may also be specialized to aid the mouse with certain behaviors and navigation. Responses in the mouse visual cortex are modulated by spatial context. Neurons in V1 are not just modulated by the visual stimuli but are also modulated by the location and animal is in the environment, like hippocampal place cells (Saleem et al., 2016). The primary routes through which the hippocampus receives visual information are the two internal cortices, which encode information related to self-motion (MEC) and object related motion (LEC). This has led some scientists to theorize that visual field information in V1 is processed in parallel based on visual field coverage. The center of the visual field, in this case, would be specialized for detecting objects while the periphery would be specialized for detecting object motion.

In the mouse visual cortex, visual areas are biased in regard to coverage of the visual field. Some visual areas are biased toward the periphery, and some are biased toward the center of the visual field. It is hypothesized that this feature of the visual field is due to certain visual areas being biased to the part of the visual field with the most relevant information. For instance, optic flow might be best processed in the periphery of the visual field, so neurons in this area may be functionally specialized for detecting speed, whereas neurons in the center of gaze may be better suited for processing form (Saleem et al., 2020).

1.3.3 CENTER-PERIPHERY BIAS MAY BE THE BASIS FOR DIFFERENT FUNCTIONAL PROPERTIES BETWEEN AREAS

Functional differences between higher visual areas may be due in part to their center-periphery bias. Primate object-related areas such as LO and V4 have a center-periphery bias depending on what features they encode. Face-selective regions tend to be biased, meaning over-represented by neurons that encode the center of gaze. Object-selective regions that represent peripheral objects, such as buildings, tend to be biased for the periphery (Hasson et al., 2002). This signifies that there may be different circuits that use information from the center and periphery of the retina, and that this may contribute to the functional properties found in different visual areas. Area MT may similarly encode information in the center and periphery differently. There are myeloarchitectonic differences between the projections from areas V1 and V2 based on whether they are coming from the center or periphery. The heavily myelinated area of MT gets projections from peripheral V1 and V2 (Kastner et al., 1998). Furthermore, information from the central and peripheral part of the visual field seems to arrive to extrastriate areas via two different routes, since the onset latencies of neurons in some dorsal stream areas are shorter for stimuli in the peripheral part of the visual field (Stephen et al., 2002).

The fact that different circuits may process information from the center and periphery of the visual field has behavioral consequences, as reaching for objects that are in the center of gaze versus the periphery of gaze rely on two different streams: reaching in central vision involves the medial intraparietal sulcus, and the caudal part of the premotor cortex. Reaching for objects in the periphery requires the parieto-occipital junction and the rostral part of the PMd (Prado et al., 2005).

1.4. HOW I PLAN TO EXTEND ON PUBLISHED STUDIES

Chapter 2 of my thesis will address the following aims 1 and 2. Chapter 3 will address aim 3. Chapter 3 of my thesis is the study *Characterizing the effect of robustness of tuning metrics in mouse visual cortex*, published in eNeuro.

Aim 1. Determine how SF and TF is mapped across the mouse visual cortex: All of the current literature has focused on one retinotopic location in each visual area (often an undefined location that may differ between studies). I this thesis, I have asked whether there are differences in SF and TF frequency tuning across each visual area.

There is evidence that the SF changes across V1 in the mouse (Rhim et al., 2017), and that neurons in the binocular zone are functionally specialized (Salinas et al., 2017). Therefore, I expected to find tuning differences across V1. Whether there are SF and TF differences across higher visual areas is less clear. My null hypothesis was that SF and TF tuning properties are homogeneous across mouse V1 and each higher visual areas.

In primates, the functional specialization of neurons is thought to change abruptly at visual area borders (Popovkina et al., 2019; Rosa & Elston, 1998). It is assumed that this is also true in the mouse (Glickfeld et al., 2012). However, in mice, fundamental stimulus features are processed more broadly (Minderer, 2019), and some stimulus features are processed in a global manner and are not constrained to being processed in a particular area. I am testing the null hypothesis that functional properties, such as temporal and SFs, change abruptly across areal borders. An alternative hypothesis is that functional properties change continuously across visual area borders. Another alternative is that while there are abrupt changes across visual cortex, they do not occur at area borders. I sought to describe how SF and TF tuning are mapped across the mouse visual cortex.

The current evidence points to fundamental differences between how mice and primates processes visual information. More information about the mouse visual cortex will help solidify the important distinctions between the mouse and primate visual systems.

Aim 2. Determine whether calcium imaging provides an accurate measure of the temporal frequency tuning of somata in mouse visual cortex: Previous studies have employed 2P microscopy to measure somatic SF and TF tuning in mouse visual cortex. 2P microscopy offers cellular resolution, but with al field of view of ~400 um which is smaller than most visual areas in the mouse. Widefield imaging offers the ability to measure SF and TF from neurons across ~10 mm, enough to image all visual cortical areas simultaneously. Simultaneous measurements not only accelerate data collection, but facilitate comparisons across visual areas, that may be confounded by behavioral changes during serial imaging experiments.

The major disadvantage of widefield imaging is that it sacrifices cellular resolution in densely labeled mouse lines such as those I have employed in my thesis studies. Fluorescence can arise from neuronal somata, but also from dendrites and axons. At any location, fluorescence may arise from dendrites an axon from neurons in other locations. The tuning measured with widefield fluorescence might not accurately represent the SF and TF tuning of somata at that location. I sought to make a comparison of widefield and 2P imaging to validate widefield imaging as a method of measuring TF tuning in visual cortex.

Aim 3. Determine to what extent selection criteria can account for inconsistencies in the literature: There are five previous studies that have measured the temporal and spatial frequency tuning properties of mouse visual cortex (Tohmi et al., 2014; Roth et al., 2012; Marshel et al., 2011; Andermann et al., 2011; Glickfeld et al., 2013). There are inconsistencies and gaps in these studies. Experimental parameters vary across the existing 5 studies, for example, they use different anesthesia states, different indicators (some of which are less sensitive than GCaMP6; Tian, 2009; Chen et al., 2013), different stimulus presentations, and different methods of determining cellular responsiveness. Of these differences, the methods of determining cellular responsiveness are likely to have profound effect on results. In chapter 3 of my thesis, I examined the effects of different analysis approaches, particularly different selection criteria, and find that inclusion criteria have a large effect on the tuning metrics that are derived from a dataset.

2. MAPPING SPATIAL AND TEMPORAL FREQUENCY TUNING IN MOUSE VISUAL CORTEX WITH CALCIUM IMAGING

2. ABSTRACT

In this Chapter, I used a combination of widefield and 2-photon (2P) calcium imaging to investigate how spatial frequency (SF) and temporal frequency (TF) tuning properties are mapped in the mouse visual cortex. Receptive field tuning properties like SF and TF correlate with functional specialization of visual areas in primates and cats. I measured the TF tuning properties using drifting grating stimuli in three altitude locations in V1, and two altitude locations in higher visual area AM. I found clear evidence of functional specialization at different altitude locations in V1. Neurons in anterior V1 (lower visual field of view) have lower average TF and SF tuning than posterior V1 (upper visual field of view). I measured whether tuning gradients, gradual changes in tuning properties across a visual area or areas, in V1 and higher visual areas were consistent across cortical layers and in thalamic (dLGN) axons. In most visual areas, gradients had the same slope with respect to altitude. Interestingly, I found TF gradients that did not change abruptly across areal borders. While TF tuning differed across cortical layers, the relationship between TF and altitude was consistent across laminar populations and in dLGN axons. Therefore, gradients in V1 and some higher visual areas likely result from input from dLGN axons.

2.1 INTRODUCTION

A fundamental principle of the mammalian visual cortex is that neurons with similar functional properties are clustered together. This results in maps of receptive field properties, such as orientation selectivity, spatial frequency (SF) tuning, direction selectivity, and temporal frequency (TF) tuning (Hubel & Weisel, 1962; Swindale et al., 1987; Everson et al., 1981). These maps exist at different scales throughout the visual cortex and serve different functions.

In mice, recent evidence indicates that receptive field properties change across the visual field. Though mice do not have a fovea, neurons in the upper visual field are tuned to higher SFs (Rhim et al., 2017). Neurons in the upper visual field are also less sensitive to coherent motion (Sit & Goard, 2020) and this asymmetric coherent motion processing extends to higher visual areas. In addition, directional selectivity and orientation selectivity gradients exist in dLGN (Scholl et al., 2013; Piscopo et al., 2013). These tuning gradients could come from unequal expression of different retinal ganglion cell types with different tuning properties. Unlike in primates, several types of mouse retinal ganglion cells (RGCs) have asymmetric retinotopic distributions, clustering in different regions of visual space (Zhang et al., 2012). RGCs influence receptive field properties in cortex (Hillier et al., 2017). Asymmetric receptive field properties may result in parallel representations of visual stimuli depending on where they are presented in the visual field.

The structure of the mouse visual cortex is similar to that of primates. Most of the cortical visual input comes from the dLGN of the thalamus via the retinogeniculate pathway, with some direct input from LP via the retinocollicular pathway. The mouse primary visual area projects to several interconnected (Harris et al., 2019), but hierarchically organized higher visual areas, which have unique SF and TF tuning properties. Roughly twelve visual areas have been identified in the mouse, although there is variation mouse-to-mouse in how consistently each area can be identified (Zhuang et al., 2017). Mouse higher visual areas have unique SF and TF tuning properties (Tohmi et al., 2014; Roth et al., 2012; Marshel et al., 2011; Andermann et al., 2011; Glickfeld et al., 2013). However, the functions of the mouse higher visual areas and their homology to primate visual areas remain active areas of investigation.

Five previous studies have measured the SF and TF tuning properties in mouse visual cortex. These five studies have measured the SF and TF tuning of neurons in small 2P fields of view of each region, targeting the center of gaze, of up to seven visual areas. However, most studies have sampled three or less. All studies used 2P calcium imaging and measured responses to drifting gratings (Tohmi et al., 2014; Roth et al., 2012; Marshel et al., 2011; Andermann et al., 2011; Glickfeld et al., 2013).

Although mouse higher visual areas have distinct SF and TF tuning properties, it is unclear whether and how SF and TF tuning gradients change across the visual field, and how gradients of SF tuning in V1 relate to SF tuning gradients in higher visual areas.

Here I use widefield and 2P calcium imaging to map the SF and TF tuning properties of neurons in mouse visual cortex. Widefield fluorescence microscopy is used to monitor the fluorescence from spiking neurons in the brain. It records fluorescence from neurons that express fluorescent indicators with a low magnification camera. There are contributions from axons, dendrites, and somata to the widefield signal. Although widefield calcium imaging is a widely used technique, previous comparisons between widefield and 2P have not tested whether widefield is an accurate measurement of somatic TF tuning in a cortical region. To address this, I made a direct comparison of the tuning metrics measured with widefield and 2P in the same animals.

First, I conclude that widefield is a good approximation of the underlying pooled somatic signal and can accurately measure tuning properties. Then, I describe the presence of tuning gradients in TF and SF in visual cortex in layer 2/3.

The unparalleled genetic accessibility of mice allows for us to interrogate functional maps in laminar populations. Laminar populations are known to have different receptive field properties in the mouse, including orientation and direction selectivity (de Vries et al., 2020). I describe similar relationships between the altitude at TF tuning of neurons cortical layers, including Layer 4, Layer 5, and LGN axons.

2.2 METHODS

2.2.1 MICE

I used the following Cre-lines to image in bulk fluorescent widefield calcium activity in layer 2/3, layer 4, and layer 5/6, respectively: *Cux2-CreER*^{T2}*;CaMKII-tTa;Ai93* (N = 10), *Scnn1a-Tg3-Cre;CaMKIIa-tTa;Ai93* (N = 6), *Rorb-IRES2-Cre;CaMKIIa-tTa;Ai94* (N = 9), and *Rrb4-Cre_KL100;Ai94* (N = 8). Mice were aged 60-120 days and hemizygous for each transgenic gene. All transgenic Cre-lines express GCaMP6s of GCaMP6f in excitatory neurons. In order to image thalamic axons, I used transgenic line *Vipr2-IRES2-Cre;Ai162*(GCaMP6s).

2P imaging was performed in V1 or AM of either *Rorb-IRES2-Cre;CaMKIIa-tTa;Ai94* (N = 4) or *Emx1-Cre;Ai94* animals (N = 4). Two *Cux2-CreER*^{T2}*;Ai140* animals were used for validation of hemodynamic correction experiments.

A 5 mm cranial window was implanted over the left visual cortex. The preparation was similar to that described previously (Andermann et al., 2010; 2011; Goldey et al., 2014). To implant the window, a mouse was placed under isoflurane anesthesia, a head restraint bar was attached to the skull using C & B Metabond (Parkell) and a 5 mm craniotomy opened at center coordinates 3.1 mm lateral, 1.3 mm anterior to lambda. After surgery, the animals were allowed to recover for at least 7 days before retinotopic imaging with intrinsic signal during anesthesia (for detailed retinotopic protocol, see Juavinett et al., 2017). Subsequently, widefield calcium imaging and 2P imaging were performed. All experiments and procedures were approved by the Allen Institute Animal Care and Use Committee.

2.2.2 RETINOTOPIC MAPPING WIDEFIELD STIMULUS

To minimize animal distress, all imaging sessions were limited to 1 hour. To retinotopically map visual areas, full-field drifting checkerboard stimuli were displayed to awake, head-restrained, freely running mice. Retinotopic mapping stimuli were presented on a 43” LCD monitor positioned 13.5 cm from the right eye and covering the entire right visual field (ASUS PA248Q, frame rate 60 Hz, mean luminance: 50 cd/m^2). I used a drifting checkerboard stimulus as described in Zhuang et al. (2017). This method was chosen for its ability to gather retinotopic border information quickly (<1 hour). The drifting checkerboard stimulus is constantly displayed (leading to 30-fold reduction in acquisition time compared to other common methods) at a period that doesn’t match any biological periodicity, such as breathing or heart rate. Fourier analysis at the stimulus frequency eliminates the noise due to these periodic artifacts.

Briefly, retinotopic maps were generated by sweeping a bar across the monitor (Kalatsky and Stryker, 2003). The bar contained a flickering black-and-white checkerboard pattern, with spherical correction of the stimulus to stimulate in spherical visual coordinates using a planar monitor (Marshel et al., 2011; Garrett et al., 2014). Each square alternated between black and white at global. To generate a map, the bar was swept across the screen ten times in each of the four cardinal directions with a gap of 5 s between sweeps to ensure that stimulus-evoked activity had subsided.

2.2.3 DRIFTING GRATING WIDEFIELD STIMULUS

Drifting grating stimuli were displayed on a 24“ LCD monitor positioned 9 cm from the right eye, again covering the entirety of the visual field (ASUS PA248Q, frame rate 60 Hz, mean luminance 45.3 cd/m^2)**.** Stimuli were presented to awake, freely running mice. Sinusoidal drifting gratings of six different SFs covering five octaves (0.02, 0.04, 0.08, 0.16, and 0.32 cpd), six different temporal frequencies covering five octaves (0.5, 1, 2, 4, 8, and 15 Hz), and eight orientations (45 degree intervals starting from horizontal) were displayed. Conditions were chosen to cover the range of SFs and TFs that drive visually responsive cells in visual cortex - cells in mouse visual cortex are unresponsive past .32 cpd and 15 Hz (Neill and Stryker, 2008; Roth et al, 2010). Gratings were displayed for 4 s followed by a 2 s grey period to allow responses to return to baseline. All stimuli were spherically corrected.

2.2.4 2P STIMULUS

Stimuli were displayed on a 24” LCD monitor positioned 9 cm from the right eye (ASUS PA248Q, frame rate 60 Hz, mean luminance 45.3 cd/m^2). Drifting grating and locally sparse noise stimuli were both displayed in one session.

To map the receptive fields of ROIs in visual cortex, I used locally sparse noise. For locally sparse noise, bright and dark squares (8° × 8°) were displayed in a random sequence on a grid tiling the entire monitor. The size of receptive fields in mouse V1 range from 10-20 degrees, while receptive fields in higher visual areas range from 20-40 degrees. de Vries et al. (2020) compared stimuli of 4 and 8 degrees in V1 and higher visual areas and found cells to be more responsive to 8 degree stimuli, so I chose a square of 8 degrees for stimuli targeting both AM and V1. Locally sparse noise was used because it can map receptive fields more quickly sparse noise stimuli as more than one square in the grid can be displayed at once. At any given time, multiple squares could be displayed but the minimum distance between those squares was no less than 50 degrees, to ensure that cells weren’t incidentally excited by neighboring squares.

For the drifting grating stimuli, I sought to map only temporal frequency, so I only presented one SF. Each square lasted 100 ms and in total was displayed 40 times. Drifting gratings of six TFs (0.5, 1, 2, 4, 8, and 15 Hz), one SF (0.04 cpd), and four orientations were presented. Four repeats of each stimulus combination were presented. Gratings were displayed for 2 s followed by a 2 s grey period. All stimuli were spherically corrected.

2.2.5 WIDEFIELD MICROSCOPY RETINOTOPIC MAPPING

Retinotopic maps were gathered with either fluorescence or intrinsic signal imaging. Widefield fluorescence images were acquired with a 1:1 optical relay using two x1 PlanAPO dissecting microscope lenses (Leica, 10450028). For fluorescence imaging, illumination was from a blue LED (M470, Thorlabs), via a bandpass filter (469/35, Semrock) and fluorescence was detected by a CCD camera (Orca R2, Hamamatsu) via a 497 nm dichroic and 525/39 bandpass filter (Semrock). Illumination and image acquisition were controlled with software written by Jack Waters using the Hamamatsu Video Capture Library for Labview, v.2.0.2.

2.2.6 WIDEFIELD MICROSCOPY DRIFTING GRATINGS

The absorption of light by hemoglobin can substantially decrease fluorescence by absorbing light during excitation or emission of fluorescent indicator proteins in the brain. This decrease is typically slower than and follows the initial increase in fluorescence due to GCaMP6 (Zhuang et al., 2017). However, correcting for this decrease is necessary for stimuli are presented for an extended period of time (longer than ~500 ms), such as the drifting checkerboard stimulus. Absorption can be well-approximated using a single-wavelength backscatter measurement at an isosbestic wavelength (which is equally absorbed by deoxyhemoglobin and oxyhemoglobin, which have different excitation and emission spectra), which occurs at ~577 nm. To correct for the absorption of light by hemoglobin, I made simultaneous backscatter and fluorescence measurements of mouse visual cortex.

Images were produced by a tandem-lens microscope of custom optomechanical design (**Supplementary Figure 1**, see Valley et al., 2020). Epifluorescence illumination used a 470 nm LED (Thorlabs M470L3) filtered (Semrock FF01-474/27-50) through the objective lens. Backscatter illumination in yellow used a 577 nm LED (Thorlabs M565L3) and a bandpass filter

(Semrock F01-578/21). Yellow illumination was focused onto a 1-to-7 fan-out fiber bundle (Thorlabs BF72HS01), and the termination of each of the seven fibers was uniformly spaced circumferentially around a custom light shield surrounding the imaging objective with each fiber terminating at 45 degrees incident to the brain surface. Backscatter measurements were made to capture just the decrease in fluorescence due to the absorbtion of light by hemoglobin. Both the backscatter and fluorescence were passed through a high-pass filter (Edmund Optics Y-50, 500nm) to a Hamamatsu Flash4.0 v3 sCMOS camera. Datasets were collected at a resolution of 1024 x 1024 with a 1 x objective at a field of view of ~15 mm.

The fluorescence and backscatter LEDs were strobed and the camera triggered the fluorescence and backscatter exposures at 50 Hz. The two channels were deinterleaved in post-processing, so the final sample rate for each channel was 25 Hz.

2.2.7 2-PHOTON IMAGING

After surgery and habituation, 2P imaging was performed on a Sutter MOM. Before 2P imaging, retinotopic maps were generated. A vasculature map was taken, so that fields of view at different altitude locations in different visual areas could be found based on local vasculature using LED illumination. Imaging was done in a single plane at a depth of 300 um below pia. 2P was performed in the left hemisphere.

Up to three fields of view (up to three in V1 and two in AM) were imaged in one session at different altitudes.

A 16x/0.8 NA water immersion objective (Nikon 16XLWD-PF) was rotated to 24 degrees from horizontal to image the prep. Emitted light was first split by a 735 nm long pass dichroic mirror (FF735-DiO1, Semrock), filtered through a 470-588 nm bandpass emission filter (FF01-514/44-25, Semrock), and detected with a GAsP Photomultiplier tube (Hamamatsu). Image acquisition was controlled using Vidrio ScanImage software (Pologruto et al., 2003, Vidrio LLC). To maintain constant immersion of the objective, I used gel immersion (Genteal Gel, Alcon).

2P excitation was generated by laser illumination from a Ti:sapphire laser (Coherent Chameleon Ultra II) tuned to 920 nm. A single z-plane (720×720 µm (1x) or 380x 380 µm (2x) 512 × 512 pixels resolution) was imaged at a frame rate of about 30 Hz with an 8 KHz resonant-linear mirror galvanometer pair (Cambridge Technology, CRS 8K). To maintain constant imaging depth, automatic z-drift correction functions were implemented for experiments using the MOM motors. Briefly, a correction z-stack (± 50 µm from targeted depth, 2 µm step depth) was recorded before each imaging session and, during the session, the current imaging plane was continuously compared to each plane in the correction z-stack. If a drift in depth was detected, the stage was automatically adjusted to compensate for the drift, thus maintaining constant imaging depth.

2.2.8 WIDEFIELD ANALYSIS

Analysis of widefield movies was performed with Python 2.7. The procedure detailed above generates a single widefield movie containing the fluorescence and backscatter channels. The first step is to deinterleave this movie, resulting in one movie containing the fluorescence information and one containing the hemodynamics information. The recorded widefield movies were averaged every 5 frames and downsampled in x and y dimensions each 2-fold.

To eliminate the hemodynamic component, the absorption of blood hemoglobin, which has different absorption spectra in its deoxygenated and oxygenated states, needs to be approximated. Valley et al. has shown that using backscatter measurements are effective at eliminating the hemodynamic component. In GFP mice fitted with a 13 mm cranial window described in Valley et al, using two-wavelength backscatter (with two wavelengths that have different absorption coefficients for oxygenated and deoxygenated hemoglobin) approach versus a single isosbestic wavelength backscatter measurement was only marginally more effective in *Cux2-CreER*^{T2}*;Ai140* mice, which express GFP in cells in layer 2/3. In GFP mice, the hemodynamic component is thought to contribute to the majority of the variance found in the raw fluorescence traces (no stimulation was presented during these measurements). Therefore, eliminating the hemodynamic component should eliminate the variance in a fluorescence trace. In *Cux2-CreER*^{T2}*;Ai140* mice, using a double-wavelength approach decreased the variance from 0.12 to 0.09 percent variance remaining. However, this study used a preparation that covered the entire cortex, so in order to confirm that the majority of the variance could be eliminated in the preparation I used, I compared the single and double-wavelength approaches in the 5mm window.

To run the double-wavelength linear regression approach detailed in Valley et al, I collected two movies. I collected fluorescence data using 480 nm at 100 Hz and used two channels of backscatter data (577 nm and 630 nm) using a rolling shutter collected at 25 Hz (for more details, see Valley et al., 2020). I then deinterleaved the backscatter movie, so that I had three channels: two backscatter and one fluorescence. The fluorescence channel and reflectance channels were converted into %d f/f. I then calculated the weights at each pixel that best fit fluorescence from a GFP-expressing animal. Then I subtracted the weighted 577-nm/630-nm channel data from the fluorescence data and calculated the remaining variance.

In two mice, the single-wavelength approach left 15% percent remaining variance while the double-wavelength left 12% percent remaining variance (**Supplementary Figure 2**). I suspect that elimination of 85% of the remaining variance from hemodynamics will be enough to eliminate the confound of hemodynamic contamination, as the amplitude of the hemodynamic sag is about 1% df/f, while the increase in fluorescence due to GCaMP is 3-10% df/f across the cranial window.

In all analyses which required altitude, azimuth, eccentricity, or areal border measurements in tandem with TF or SF tuning, retinotopic maps were superimposed onto temporal frequency maps using a rigid transform with the vasculature map as guidance.

2.2.9 2-PHOTON ANALYSIS

The recorded 2P movies for each imaging plane were first downsampled 5-fold, then were motion-corrected using a custom-written python package (https://github.com/zhuangjun1981/stia/tree/master/stia, Zhuang et al., 2017). ROIs were segmented using Suite2p. The segmented ROIs were inspected manually to ensure that each corresponded to a soma. They were then filtered by overlap (for ROIs with more than 20% overlap, the smaller ones were excluded). ROIs were binary. For each retained ROI, a neuropil ROI was created as the region between two contours by dilating the ROI's outer border by 1 and 8 pixels excluding the pixels within the union of all ROIs. The calcium trace for each ROI was calculated by the mean of pixel-wise product between the ROI and each frame of the movie, and its neuropil trace was calculated in the same way using its neuropil ROI. Neuropil contamination, the presence of fluorescence from surrounding GCaMP-labeled processes in the somatic pixels, is a characteristic of densely labeled tissue. To remove the neuropil contamination, the neuropil contribution of each ROI's calcium trace was estimated by a linear model and optimized by gradient descendent regression with a smoothness regularization (Zhuang et al., 2017; de Vries et al., 2020). This resulted in the estimation of a neuropil contamination ratio *r,* which was generally low (a mean of 0.1 across all datasets). Increasing this value to a larger fixed value (0.7-0.8) did not significantly change the average SF or TF in a field of view.

2.2.10 DRIFTING GRATING ANALYSIS - WIDEFIELD

I calculated the TF tuning of pixels in the image using full-field drifting gratings as described above. For a given TF and SF combination (averaging over all orientations), the calcium traces within a temporal window around the stimulus onset were extracted and aligned by the drifting grating onsets. An event-triggered average trace was then calculated as the mean trace across all aligned traces. The mean value of the averaged trace in the window [-1, 0] seconds from the onset was calculated as the baseline and event-triggered df/f trace was calculated as (average trace - baseline) / baseline. The pixel-wise response to a drifting grating was defined as the mean of the event-triggered average from [0.25, 2 s].

Most pixels in the widefield image were most responsive to low TF values (0.5 Hz or 1 Hz). However, there were differences in the response to higher temporal frequencies (essentially how skewed the tuning curve is to low TFs). In order to measure how skewed temporal frequency tuning responses were across visual cortex, I used a measure of skew which I called center of mass, which was defined as the mean of the normalized tuning curve multiplied by the temporal frequency values:

$$\sum \ \frac{\mathrm{DF}}{\mathrm{F}}_{TF} \Big/ \frac{\mathrm{DF}}{\mathrm{F}}_{TFmax} * TF \qquad , TF = 0.5, 1, 2, 4, 8, 15$$

While the center of mass analysis is an effective measure of skew, it does have the effect that unresponsive pixels are given a center of mass that is in the center of the tuning curve. This can appear artificially high, especially when pixels are noisy and tuning curve is flat, resulting in intermediate center of mass values.

In order to remove unresponsive pixels from the widefield image, I used a signal to noise threshold. To define this threshold, I artificially degraded the signal in a 20 x 20 pixel square in the middle of V1 with low-amplitude white noise. I degraded the signal to noise by 25, 50, and 75 percent, and saw the TF slowly change (**Supplementary Figure 3**). The signal to noise at which the TF changed more than 20% was the signal to noise threshold used to discard unresponsive pixels.

2.2.11 RECEPTIVE FIELD ANALYSIS - 2-PHOTON

I calculated the ROIs' spatial receptive fields from their responses to the locally sparse noise stimulus. For a given square flash at a particular location with a particular sign, the calcium traces within a temporal window around the square onsets were extracted and aligned by the square onsets. An event-triggered average trace was then calculated as the mean trace across all aligned traces. The mean value of the averaged trace in the window [-0.5, 0] seconds from the onset was calculated as the baseline and event-triggered df/f trace was calculated as (average trace - baseline) / baseline. The response amplitude to this particular square was then calculated as the mean DF/F in the window [0, 0.5] second from the stimulus onset. By repeating this procedure for all squares presented in locally sparse noise stimuli, a 2d amplitude map was generated tiling the entire visual space covered by the monitor for each sign (“ON” from bright squares and “OFF” from dark squares). From the amplitude map, a z-score map was calculated by subtracting the mean and dividing the standard deviation of the entire map. The z-score map was then smoothed by a Gaussian filter with a sigma of 1 pixel and upsampled by a ratio of 10 with cubic interpolation. The resulting map was defined as the receptive field map with a resolution of 0.5 degrees. I defined a receptive field map with a peak value exceeding 1.6 as having a significant spatial RF. For each significant spatial RF, an RF mask was generated by thresholding either with a value of 1.6 (for maps with a peak less than 4) or with a value of 40% of its peak (for maps with a peak greater than 4, Zhuang et al., 2017). The RF area (plotted in Figure 1) was calculated as the area of the binary mask after thresholding. The RF center was calculated as the location of the center of mass from the weighted mask after thresholding.

2.2.12 DRIFTING GRATING ANALYSIS -2-PHOTON

I calculated the preferred temporal frequency tuning of each ROI with full-field drifting grating stimuli of six temporal frequencies (0.5, 1, 2, 4, 8, and 15 Hz) and four orientations at a SF of 0.04 cpd. For a given temporal frequency and orientation combination, the calcium traces within a temporal window around the stimulus onset were extracted and aligned by the drifting grating onsets. An event-triggered average trace was then calculated as the mean trace across all aligned traces. The mean value of the averaged trace in the window [-0.5, 0] seconds from the onset was calculated as the baseline and event-triggered df/f trace was calculated as (average trace - baseline) / baseline. The response amplitude to this particular square was then calculated as the mean df/f in the window [0, 2] seconds after stimulus onset. From the response amplitudes at each TF x orientation combination, I generated TF tuning curves by averaging across all orientations.

To compare with widefield, I pooled the somatic 2P data by summing the raw fluorescence of all the neurons in a single field of view. This generated a single fluorescence trace. From the event-triggered traces, I took the mean value in the window [0, 2] to generate a tuning curve. I then calculated the center of mass TF from the resulting tuning curve. To generate confidence intervals for this data, I bootstrapped. I sampled the number of ROIs with replacement one thousand times, summed the fluorescence from these values, and calculated the center of mass TF.

2.2.13 LINEAR MIXED MODEL

I used a linear mixed model to determine if temporal frequency tuning covaries with receptive field location. Using a linear mixed model, I tested whether the temporal frequency that tends to produce the greatest fluorescence change (the preferred TF) depends on the receptive field location. I chose a linear mixed model because it can capture fixed and random variables. The fixed effects in this case are what we're trying to predict the response strength from (temporal frequency and receptive field location). Random variables result from non-independence of the data, which is inherent in calcium imaging datasets. Response strength can vary from mouse-to-mouse and experiment-to-experiment, which is captured in linear mixed models (essentially with linear mixed models, I can reject the hypothesis that response strength varies only due to differences in experimental conditions). In calcium imaging, there is inherent variability of neurons (since response strength varies between neurons), different mice have different labeling strength, and experimental conditions may vary day-to-day resulting in different average levels of fluorescence between experiments.

I computed a likelihood ratio test to test the null hypothesis that the coefficients of interest (fixed effects) in the linear mixed model were equal to zero, indicating no interaction between TF and receptive field location. To do this, I computed an ANOVA between two nested models: one including the interaction coefficients and one without. This gave us a test statistic that follows a X^2 distribution, where k is the number of observations.

2.3 RESULTS

In this section, I mapped the TF tuning of neurons across V1 using two techniques: widefield calcium imaging and 2P calcium imaging. I found that the average preferred TF tuning of neurons in V1 decreases with decreasing receptive field altitude, and this phenomenon is captured in both widefield and 2P measurements. While widefield calcium imaging reported higher values of TF tuning for a given receptive field altitude, both methods measured a decrease in average TF tuning with decreasing receptive field altitude. The higher TF tuning measured with widefield calcium imaging is likely due to two factors: neuropil contamination (further described in the **DICUSSION**) and biases in the neural populations recorded using the two imaging techniques (further described in the **DISCUSSION** and **CHAPTER 3**). However, this comparison validates widefield as an accurate way to measure differences in TF tuning preferences across the visual field. I go on to map the SF and TF tuning across laminar populations in the mouse.

2.3.1 THERE ARE GRADIENTS OF TEMPORAL FREQUENCY TUNING IN MOUSE V1 AND HIGHER VISUAL AREA AM

I measured the temporal frequency (TF) tuning of neurons in the mouse visual cortex in three *Rorb-IRES2-Cre;CaMKIIa-tTa;Ai94* transgenic mice using 2P calcium imaging (**Figure 1A,** Allen Brain Atlas 2P tomography Transgenic Characterization experiment 238675). *Rorb-IRES2-Cre;CaMKIIa-tTa;Ai94* mice densely express GCaMP6f in layer 4 of the neocortex.

2P calcium imaging permits recording of neural activity with single cell resolution simultaneously from hundreds of neurons in a given field of view. 2P imaging with fluorescent calcium sensors provides accurate measurements of tuning curves compared to electrophysiological measurements (Nauhaus et al., 2011). However, the translation between neural spiking activity and calcium-related fluorescence is complex and could introduce errors. While GCaMP fluorescence scales with number of action potentials (Chen et al. 2013), calcium indicators have a limited dynamic range (Peron et al., 2015), and there are known low-pass filtering and nonlinearities that occur between the conversion of neural spiking to calcium fluorescence.

Calcium imaging with GCaMP6s, the fluorescent reporter used in this study, can be used to decode small trains of up to 3 action potentials delivered at 15 Hz with high fidelity (Huang et al., 2021). However, the problem of converting spikes to calcium fluorescence is not totally solved (Peron et al., 2015). The dynamic range of GCaMP in vivo is hard to predict. Resting baseline fluorescence and the dynamic range of the calcium indicator are likely heterogeneous across the neural population due to differences in calcium indicator expression cell to cell, making a quantitative model of spiking from fluorescence data complicated.

As I am using symmetrical stimuli that are modulated in time, another potential concern is that calcium indicators may not be able to capture firing rate modulations in response to stimuli. This would be of particular concern for purely linear cells, where the average spike rate does not change over the stimulus presentation interval. However, most cells in mouse visual cortical areas are nonlinear (Neill & Stryker, 2008; Siegel et al., 2021) and the spike rate of the neural population in visual areas overall increases in response to visual stimulation.

Ultimately, a recent rigorous comparison between 2P and electrophysiology measurements of TF and SF tuning made in the mouse visual cortex showed that while there are some differences (notably, electrophysiological measurements report a lower average TF tuning than 2P measurements in most visual areas), both reported similar findings of the relative magnitude of the average TF tuning between visual areas. Both 2P and electrophysiology found the same hierarchical relationship of TF tuning between mouse visual areas, where V1 has the lowest TF tuning on average and RL has the highest. 2P imaging is therefore likely to be adequate to be able to describe differences in the TF tuning between neural populations, as I do here (Siegel et al., 2020). While electrophysiological measurements also have biases to large, responsive cells, correspondence between these two modalities is evidence that 2P imaging is accurately reporting the TF tuning of neuronal populations in visual cortex.

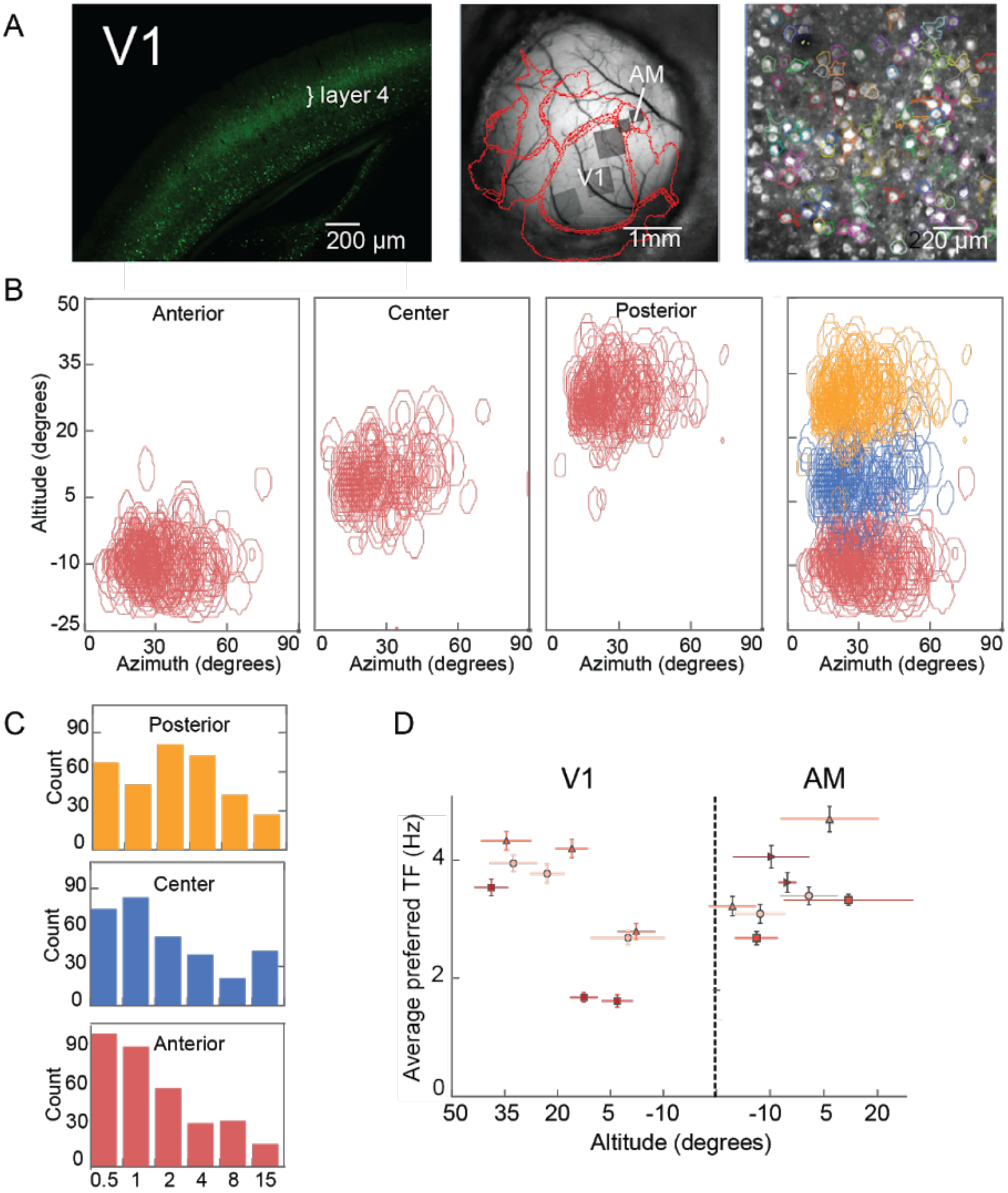

Figure 1) A) Left panel - coronal section of 2P tomography fluorescence image of GCaMP6s-positive cells in neocortex. Middle panel- widefield map of 5 mm cranial window preparation with retinotopic borders (see **METHODS**) in red and 2P fields of view in V1 and AM in grey. V1 and AM are labeled. Right panel - mean projection of 2P imaging plane with ROIs segmented before inclusion criteria were applied. **B)** Outer contours of sparse noise-derived, significant (see **METHODS**) receptive fields of neurons in three fields of view. Right panel shows three fields of view overlaid in different colors. **C)** Histograms of preferred TF tuning in three fields of view of

one example animal**. D)** Average preferred TF tuning for each field of view (y-axis) plotted against the median sparse noise derived receptive field altitude value. Each point represents median altitude of receptive field centers of a given field of view (horizontal error bars show interquartile range of this distribution) versus the mean preferred TF tuning and standard deviation at that field of view in V1 and AM.

My goal was to describe how the distribution of preferred TF tuning of neurons changed across receptive field altitude in V1. I compared the distribution of the preferred TF tuning of neurons in three separate 2P fields of view in V1 (**Figure 1A**). To do this, I first retinotopically mapped the cortical visual areas using widefield calcium imaging (our retinotopic mapping approach is described in the **METHODS**). I then targeted three regions of V1 at three different receptive field altitude locations in the widefield retinotopic map for my 2P experiments (**Figure 1A, center**). I recorded in layer 4 at a depth of 300 um below pia. Mice were awake and behaving.

I mapped the receptive field locations of neurons in each 2P field of view with sparse noise, as described in the **METHODS**. Neurons in different 2P fields of view have different receptive field altitude locations, but similar azimuth locations. The outer contours of z-score thresholded sparse noise-derived receptive fields of neurons in the three 2P fields of view in V1 are plotted in retinotopic space in **Figure 1B**. Neurons had significantly different receptive field altitude distributions based on the field of view (one way ANOVA, $p << 0.01$). I then performed a post-hoc t-test on cells in anterior and posterior fields of view and found significantly different receptive field altitude distributions in all three animals ($p << 0.01$ in all cases).

Next, using a stimulus set of six TFs ranging from 0.5 Hz – 15 Hz and four orientations**,** I calculated the preferred TF of each neuron in each 2P field of view (defined as the TF that elicits the strongest stimulus-triggered average response for each neuron; see **METHODS**). I then compared the distribution of preferred TF value in each 2P field of view.

I found that neurons in 2P fields of view associated with an average RF location in the upper visual field have higher preferred TF than neurons in 2P fields of view with an average RF location in the lower visual field of view. The distribution of the preferred TF tuning of neurons in the anterior 2P field of view (corresponding to the upper visual field) is skewed to lower values than neurons in the center or posterior 2P fields of view (**Figure 1C**). The average preferred TF tuning of neurons in the posterior field of view in V1 (corresponding to the upper part of visual space) is skewed to high TF values. Neurons in the center 2P field of view of V1, which correspond to the center of visual space close to the horizon, respond best to intermediate TF values, such that they have an intermediate TF tuning compared to cells in other 2P fields of view. Preferred TF and altitude were correlated with a Spearman’s correlation of r = 0.81, indicating substantial correlation.

The preferred TF tuning of neurons in V1 is skewed to low TF values (**Figure 1C**). This is consistent with previous measurements of TF tuning in mouse visual cortex made with 2P (Andermann et al., 2011; Roth et al., 2010; Marshel et al., 2011; De Vries et al., 2020) and extracellular probes (Neill & Stryker, 2008; Siegel et al., 2021) in other studies.

To visualize the relationship between average preferred TF tuning and receptive field altitude, I plotted the median population receptive field altitude versus the mean TF tuning for neurons in each 2P field of view (**Figure 1D**). This revealed a clear relationship between the average preferred TF and receptive field altitude in V1, where average preferred TF decreases with decreasing receptive field altitude. In sum, there is a TF tuning gradient — a gradual change in receptive field properties — across receptive field altitude.

To test whether there was a statistical effect of receptive field location on the preferred TF, I generated a linear mixed model (see **METHODS**). A log-likelihood ratio test indicated that the preferred TF of neurons depends on their receptive field altitude ($p << 0.01$). A post-hoc Mann Whitney-U test indicated that the preferred TF distributions in the posterior and anterior 2P fields of view are significantly different in all three mice ($p << 0.01$ for all three).

Using the same procedure, I then measured and compared the preferred TF of neurons in two 2P fields of view in AM. Using sparse noise, I mapped the receptive fields of the neurons in both fields. The receptive field centers of the neurons in both fields have significantly different altitude values (t-test $p << 0.01$ for all). The neurons recorded in the posterior 2P field of view in AM, (corresponding to the lower part of the visual field) have a lower average preferred TF than neurons in anterior 2P field of view (corresponding to the upper part of the visual field). The average preferred TF was significantly different in the two 2P fields of view in three of four animals (Mann Whitney-U test $p = 0.01$, $p = 0.03$, $p << 0.01$, $p = 0.1$). The average preferred TF of neurons in different 2P fields of view is higher in AM than V1 and ranges from 2-6 Hz. To test whether the receptive field location had a significant effect on the average preferred TF, I used a linear mixed model as described in the **METHODS.** A log-likelihood test resulted in a X^2 test statistic with value of $p = 0.045$, indicating significant interaction between TF and receptive field location.

There is a field sign map reversal at the border of AM and V1, which is why the x-axis has a field sign reversal in **Figure 1D** (Zhuang et al., 2017). The gradients of TF in both AM and V1 have the same slope in relation to altitude. In both AM and V1, for each 2P field of view, the median altitude value of the population of receptive field centers is slightly different. However, the average preferred TF of neurons with receptive fields having low altitude values (lower visual field) is lower than those with receptive fields with high altitude values (upper visual field) (**Figure 1D**).

Receptive field centers in each AM 2P field of view spanned a narrower band of altitudes than in V1 (-20 to 14 degrees). This result is consistent with previous studies that have mapped visual cortex (Zhuang et al., 2017). At this band of altitudes, the TF tuning of AM is significantly higher than that of V1 (Mann Whitney-U test, $p << 0.01$).

2.3.2 GRADIENTS IN AM AND V1 CAN BE MEASURED USING WIDEFIELD CALCIUM IMAGING

Next, I investigated whether there were tuning gradients across other visual areas and layers. Completing this with 2P would be both time and data-intensive, so I chose to complete these experiments using widefield imaging.

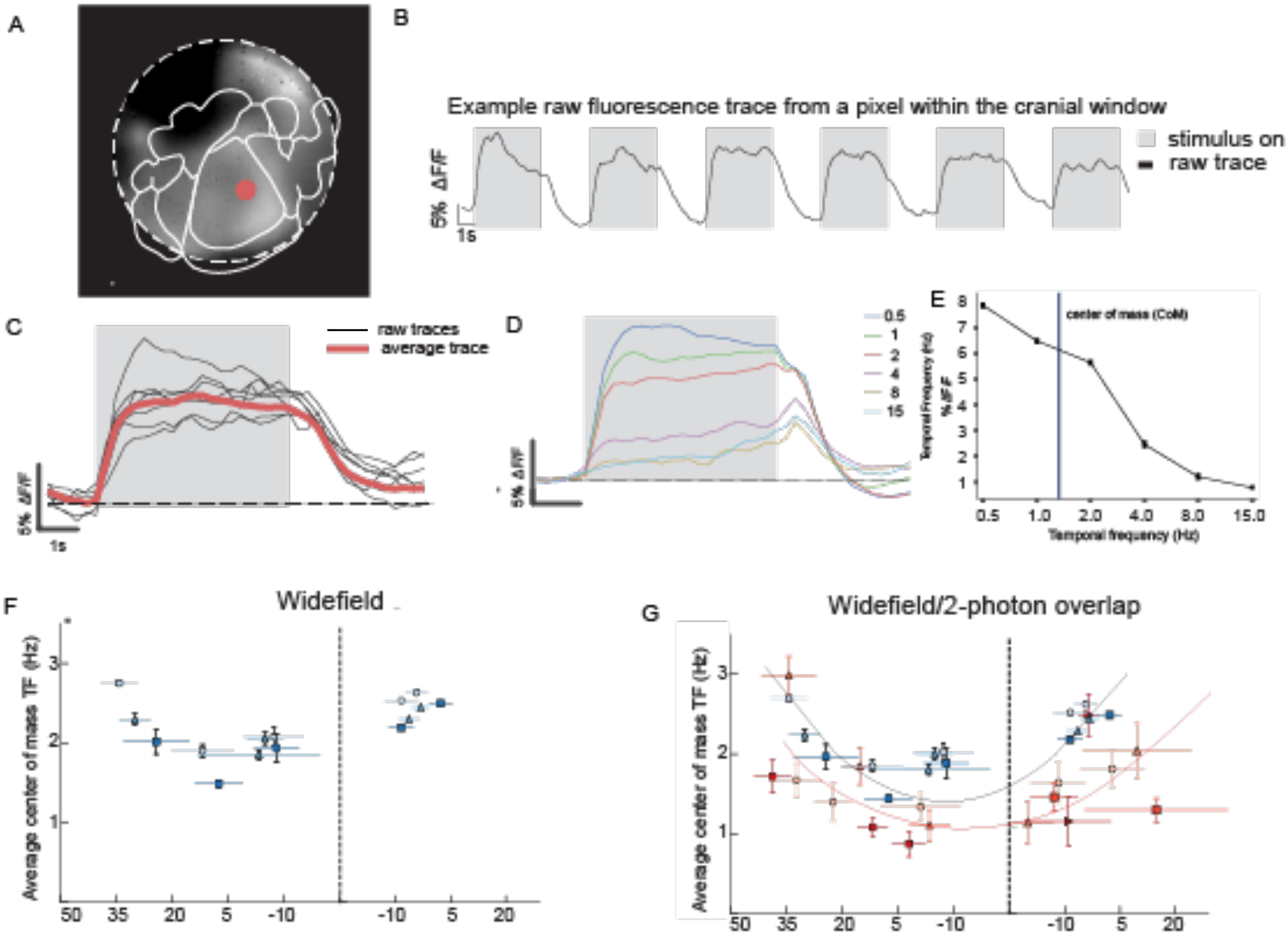

Figure 2) A) df/f image of 5 mm cranial window preparation 1 s after stimulus response. Defocused 1.5 turns. Retinotopic borders are overlaid in white**. B)** Example fluorescence trace from pixel in the middle of V1**. C)** Stimulus-triggered df/f responses (black) and averagestimulus triggered response of example pixel in response to 2 Hz TF stimulus (red). **D)** Stimulus-triggered average responses of example pixel to all TFs in stimulus dataset. **E)** Tuning curve derived from average fluorescence [0, 2]s after stimulus onset. Center of mass of tuning curve is shown as black vertical line. **F)** Pixels on widefield maps that correspond to 2P fields of view. Median altitude value derived from widefield retinotopic maps plotted on the x-axis. Median center of mass TF from widefield analysis for each pixel is plotted in the y-axis. Error bars show Inter-quartile range of TF of pixels in field of view. **G)** Data in Figure 2F overlain with data in 1G. Quadratic fits to altitude vs TF data in widefield (blue) and 2P (red).

Widefield calcium imaging uses a low magnification objective and high-speed camera to image bulk calcium activity across large areas (up to 15 mm diameter) of the brain simultaneously. This method, along with the cranial window preparation described in the **METHODS**, allows simultaneous measurement of stimulus-evoked fluorescence changes in all mouse cortical visual areas (**Figure 2A**). Widefield calcium imaging also affords similar temporal resolution as 2P calcium imaging (~25 Hz, with hemodynamic correction as described in the **METHODS**).

I used widefield calcium imaging in the same three *Rorb-IRES2-Cre;CaMKIIa-tTa;Ai94* mice, the same mice that were used for 2P imaging, and one more *Emx1-IRES-Cre;Ai94* in AM to measure TF tuning in visual areas. I displayed drifting gratings of 6 different SF values, 6 different TF values, and 8 directions and measured the bulk neuronal fluorescence changes in response to stimulus presentation (**Figure 2B**). For a given TF, the calcium traces within a temporal window around the stimulus onset were extracted and aligned by the drifting grating onset. An event-triggered average trace was then calculated as the mean trace across all aligned traces. The mean value of the averaged trace in the window [-0.5, 0] seconds from the onset was calculated as the baseline, and event-triggered df/f trace was calculated as (average trace - baseline) / baseline (**Figure 2C**). I then extracted SF and TF tuning curves for each pixel in the cranial window by taking the average df/f 2 s after stimulus onset (**Figure 2D-2E**). Like in 2P, most pixels had the strongest change in fluorescence in response to low frequency stimuli (0.5 Hz or 1 Hz) (**Figure 2E**). However, there were differences across visual areas in how strongly pixels across the image responded to high TFs.

The receptive field location of each pixel in visual areas was mapped with the widefield retinotopic mapping protocol described in the **METHODS.** Widefield retinotopic maps were generated in a separate experiment and aligned using surface vasculature maps.

I calculated the center of mass of the tuning curve for each pixel within the widefield field of view (see **METHODS**), which is a measure of how skewed the tuning curve measured at each pixel is. At pixels with high, positive receptive field altitude values (upper visual field), the center of mass TF tuning was highest (~3 Hz) (**Figure 2F**). As with our 2P TF measurements, The TF tuning decreased with decreasing receptive field altitude, with the lowest TF tuning reported at 0 degrees in receptive field altitude (visual horizon). Then, there was a reversal of the TF tuning gradient, and TF tuning increased in pixels with low receptive field altitude values (lower visual field) to 2.1 Hz.

The center of mass TF tuning values measured with widefield were higher than the TF tuning values measured with 2P. Using widefield calcium imaging, the TF tuning reported in V1 was between 1 Hz and 3 Hz. The TF tuning reported in AM was between 2 and 3 Hz. The range of tuning reported in AM using widefield was narrower than the range reported in 2P (**Figure 2F**).

It's not currently understood whether the bulk changes in fluorescence measured with widefield are an accurate representation of somatic fluorescence measured with 2P imaging. The relationship between 2P and widefield tuning measurements has not been compared directly, and the fluorescence changes and tuning reported from the two modalities might be different, since widefield captures the calcium dynamics from both soma and neuropil while 2P imaging captures the change in fluorescence from soma.

To make an accurate comparison of widefield and 2P, we recorded 2P and widefield TF mapping experiments in the same animals. I compared the widefield measurements reported in the pixels in the cortical window that corresponded to the locations of 2P recordings. Retinotopic location measurements for each pixel were derived from the widefield retinotopic mapping protocol described in the **METHODS**.

Widefield captures the fluorescence from neurons, dendrites, and axons from a region of cortex, so to compare 2P and widefield, I performed a widefield-style analysis on the 2P data. After segmentation, I pooled the fluorescence of all segmented ROIs in a given 2P field of view, to create a widefield-like “megapixel” made up of the somatic 2P fluorescence data. Then, I calculated the df/f and center of mass of the tuning curve derived from the pooled fluorescence. Widefield appears to be a good approximation of the pooled somatic 2P signal.

The pooled somatic 2P signal also revealed a gradient of TF in the altitude dimension. Again, neurons with receptive fields in the upper visual field had high TF tuning, while neurons with receptive fields in the lower visual field had low TF tuning (**Figure 2G**). Overall, the center of mass TF of the pooled somatic signal is lower than the TF reported from the widefield TF measurements (**Figure 2G**).

To make a quantitative comparison of the relationship between altitude and TF, I compared the center of mass TF of the pooled somatic signal at the anterior and posterior 2P fields of view for all three mice. The pooled somatic analysis again showed significantly different TF in the anterior and posterior fields of view in all three animals in V1 (t test, $p= <<0.01$, $p=0.02$, $p << 0.01$). In addition, I found that the pooled somatic signal had a range of TFs of ~0.75 Hz to 3 Hz and most reported TF values of the pooled somatic data fell below the widefield TF measurements (**Figure 2G**).

Both the widefield measurements and pooled somatic 2P analysis supported the conclusion that there are TF gradients in AM and V1. In both V1 and AM, neurons with receptive fields with low altitude values (lower visual field of view) had lower TF tuning. Neurons with receptive fields with high altitude values (upper visual field of view) had higher TF tuning. In AM, the range of TF values reported ranged from 1 Hz-2.5 Hz, similar to the pooled somatic data in V1 (**Figure 2G**). There was a larger spread of altitude values in the 2P data than in the widefield data. In all four animals in AM, I observed significantly different TF tuning in the anterior and posterior fields of view in all three animals (t test, $p= << 0.01$ for all) with the pooled somatic analysis.

I did not sum the fluorescence across the entire 2P field of view because doing so in many cases resulted in an overall decrease in fluorescence over the stimulus analysis window. This is likely because there are often blood vessels in each field of view, and blood hemoglobin can absorb fluorescence (Valley et al., 2020). Segmentation and neuropil subtraction eliminated this effect.

The center of mass TF tuning of the pooled somatic signal is lower than the average preferred TF tuning measured with 2P. This is due to two reasons. The first is that the center of mass analysis I used, while an effective measure of skew (**Supplementary Figure 4**), results in lower average values of center of mass than preferred average TF for equivalent distributions (assuming all neurons have the same peak df/f at their preferred TF tuning). The second is that cells that respond best to low TFs respond more strongly than cells that respond best to high TFs (Mann Whitney U test, cells with preferred TF tuning 0.5 and 1Hz vs. cells with preferred TF tuning of 8 and 15 Hz, V1: p = 0.03 AM: p= 0.021). The pooled somatic data uses raw fluorescence to create a single tuning curve. Instead of weighting every cell equally, more responsive cells will contribute more to the overall tuning curve. If more responsive cells are biased to a particular TF, in this case low TFs, it will lead to lower reported TFs in the pooled calculation.

In comparison to the average preferred TF tuning values, the TF values in the pooled somatic data are lower by an average of 1.1 Hz. At comparable fields of view, there is also a larger difference in the average TF tuning between V1 and AM, per altitude band, when the average preferred TF tuning is compared between the two areas.

Where does the reversal of the TF gradient occur in relation to the border of V1 and AM? To describe this and compare the widefield and 2P data, I fit a quadratic equation using a least squares optimization function to the center of mass TF tuning plotted against the mean receptive field altitude of neurons in each 2P field of view in AM and V1. I also fit a quadratic to the widefield center of mass TF plotted against the mean altitude for each field of view. Generally, there is good general agreement between the two quadratic curves. I assumed that the reversal occurred at the lowest point of the quadratic curve. For the pooled 2P data, the reversal occurs at -15 degrees. For the widefield data, the reversal occurs at -8 degrees. The V1-AM border occurs at -25 degrees in visual angle. Both reversals appear to occur in V1. In the 2P data, the average standard deviation of the receptive field altitude distribution of a neuronal population in a 2P field of view is roughly 9.3 degrees, while the average standard deviation of the receptive field altitude distribution of pixels in the comparable widefield field of views is 15 degrees. This means that there is a difference of 8 degrees. The slope of the TF gradient in the pooled somatic data is lower than in the widefield data (linear term in the quadratic equations: 1.15 vs 2.23). Both the 2P data and the widefield data support the notion that the TF gradient does not reverse at the V1-AM border.

2.3.3 DISCREPANCIES BETWEEN 2P AND WIDEFIELD LIKELY NOT DUE TO SCATTERING EFFECTS

Scattering by brain tissue commonly deflects photons en route to the camera chip, affecting lateral resolution. Scattering can significantly affect the trajectory of neurons from a point source in widefield imaging, such that sources of fluorescence can scatter up to 1 mm from their sources of origin. Widefield fluorescence at the brain surface is a weighted sum of photons from fluorophores distributed through 1-2 mm cubed of underlying cortical tissue (Waters, 2020). This might be a source of error and an explanation for the discrepancies between the widefield and

2P results. To test this, I used the Monte Carlo random-walk model from Waters (2020) to model the spread of fluorescence in V1 and AM.

I modeled cortical fluorescence through the depth of 700 um of cortical tissue, the depth of neocortex in the visual cortex. I assumed that fluorescence would be homogeneous throughout the cortical volume in both V1 and AM.

I tested to what extent fluorescence in V1 could alter tuning gradients in AM. To do this, I modeled responses to six different TFs in a cortical volume of a depth of 700 um and a width of 1 mm that would generate TF gradients in V1 and AM of opposite slope. I then varied the strength of the fluorescence in AM. The fluorescence in V1 was set at a consistent value, the average of the fluorescence at the center pixel (center of gaze). The fluorescence in AM was varied as a ratio of the fluorescence in V1.

I found that, even at very low fluorescence values in AM, the gradient in AM remained unaltered. At the mean ratio of fluorescence measured between V1:AM (0.51) using widefield in *Rorb-IRES2-Cre;CaMKIIa;Ai94* mice, there was no change in the gradient in AM (**Supplementary Figure 1**, right).

2.3.4 DISCREPANCIES BETWEEN 2P AND WIDEFIELD LIKELY NOT DUE TO DIFFERENCES IN TUNING BETWEEN LAYERS IN SINGLE CRE-LINE

Widefield offers no optical sectioning and captures fluorescence from other layers as well. While in the transgenic animals used in this study fluorescence is restricted to laminar populations, it is possible that neuronal projections in other layers and in other depths have different TF tunings. To test this, I measured the TF tuning of neurons and boutons at three different depths at the anterior portion of V1 (50 um from pia, 125 microns from pia and 300 microns from pia) in *Rorb-*

IRES2-Cre;CaMKIIa-tTa;Ai94 animals. I found no significant difference in the TF tuning at these different depths (**Supplementary Figure 5**).

2.3.5 THERE ARE GRADIENTS OF TEMPORAL AND SPATIAL FREQUENCIES IN V1 AND MOST HIGHER VISUAL AREAS

With widefield, I mapped TF and SF gradients across several visual areas and layers. To do this, I first visualized how consistent gradients were from mouse to mouse. Using the methods described in the **METHODS**, I measured the center of mass TF tuning and SF tuning for each pixel within the 5 mm cranial window in layer 2/3, layer 4, layer 5, and LGN axons.

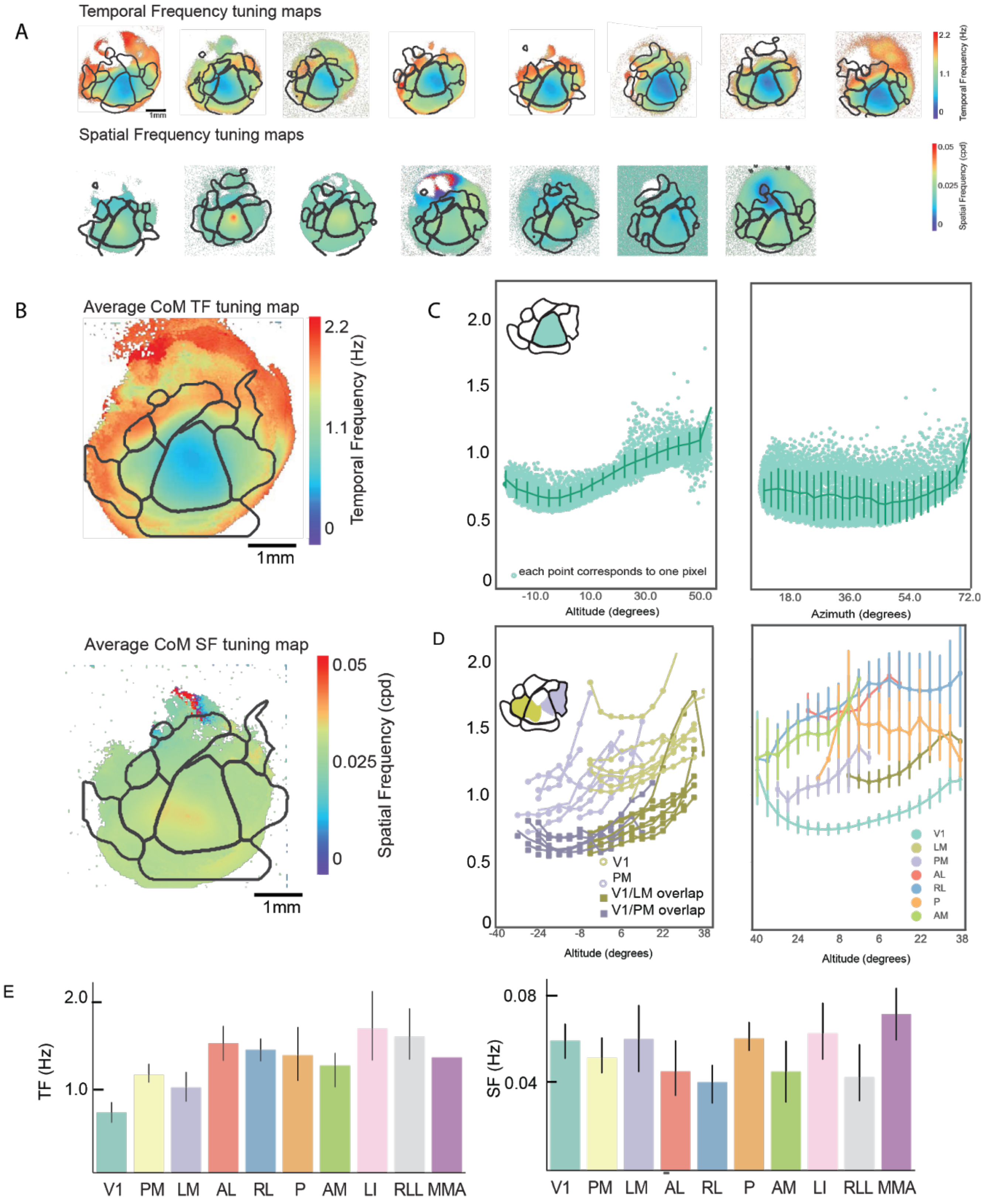
A
Temporal Frequency tuning maps
1mm
2.2
1.1
0
Temporal Frequency (Hz)
Spatial Frequency tuning maps
0.05
0.025
0
Spatial Frequency (cpd)
B
Average CoM TF tuning map
2.2
1.1
0
Temporal Frequency (Hz)
1mm
Average CoM SF tuning map
0.05
0.025
0
Spatial Frequency (cpd)
1mm
C
2.0
1.5
1.0
0.5
0
each point corresponds to one pixel
-10.0
10.0
30.0
50.0
Altitude (degrees)
18.0
36.0
54.0
72.0
Azimuth (degrees)
D
2.0
1.5
1.0
0.5
0
V1
PM
V1/LM overlap
V1/PM overlap
-40
-24
-8
6
22
38
Altitude (degrees)
V1
LM
PM
AL
RL
P
AM
40
24
8
6
22
38
Altitude (degrees)
E
TF (Hz)
2.0
1.0
V1
PM
LM
AL
RL
P
AM
LI
RLL
MMA
SF (Hz)
0.08
0.04
V1
PM
LM
AL
RL
P
AM
LI
RLL
MMA

Figure 3) A) center of mass TF and SF maps of 8 and 7 *Cux2-CreER^{T2};CaMKIIa;Ai93/4* animals, respectively. Black lines represent retinotopic borders. **B)** Top - average center of mass TF map Bottom: average center of mass SF tuning map. **C)** Right - altitude and center of mass TF of each pixel in V1. Dark green line shows median TF tuning for each 5 degree altitude bin. Right - same as left but in azimuth. **D)** Left - median TF tuning at each 5 degree altitude bins in V1, PM, and for all mice shown in A. Error bars show standard error. Right - Mean of curves shown in the left panel for all visual areas. Error bars show standard error**. E)** Mean and standard deviation of the center of mass TF tuning (left) per visual area for each and SF tuning (right).

Data in **Figure 3** were gathered from 8 *Cux2-CreER^{T2};Ai93/4* animals, which densely express either GCaMP6f or GCaMP6s, respectively, in layer 2/3 of the neocortex. Results in **Figure 3** represent SF and TF tuning in excitatory neurons in layer 2/3 of mouse visual cortex. Previous results have shown data from *Rorb-IRES2-Cre;CaMKIIa-tTa;Ai94* animals.

Mapping TF tuning in layer 2 /3 across ten different mice revealed that SF and TF tuning measured with widefield is largely consistent across mice (**Figure 3A**). Unresponsive pixels are blanked out in white, as described in the methods, giving each map a circular shape. In all 10 mice, gradients of SF and TF tuning exist in most higher visual areas as well as in V1. TF tuning is lowest in the center of V1 and increases smoothly outward from a point in the anterior part of V1 (lower part of the visual field).

There are gradients within visual areas in both SF tuning and TF tuning in the mouse visual cortex. The differences in SF tuning in different parts of V1 are subtle (average difference of 0.05 cpd across V1, a change of only 20%). In TF, these differences are more pronounced, around 1 Hz (a change of 50%). The average TF and SF center of mass maps also show the SF and TF tuning gradients found in each individual animal (**Figure 3B**).

In V1, there are TF gradients in both altitude and azimuth, but gradients are stronger in the altitude dimension. To illustrate this, I plotted the TF tuning of each pixel within V1 vs altitude

(**Figure 3C - left**). This plot shows the altitude TF tuning gradient across V1, which is 0.5 Hz at its lowest point (around 0 degrees in altitude) and 1.4 Hz at high altitudes values. The gradient in azimuth is weaker than the gradient in altitude (**Figure 3C -right**)

There are tuning gradients in most other visual areas. To describe the slope of gradients in the visual field and visualize how they relate to the gradient found in V1 across all animals, I generated the median TF value at each altitude for each visual area as described previously and took the mean of these curves.

In some visual areas, the slope of the gradient between TF and altitude is the same as in V1. In other areas, either the slope is flat, or can be reversed at altitude values as is the case with AM and P (**Figure 3D - left**).

2.3.6 AVERAGE TEMPORAL FREQUENCY TUNING MEASUREMENTS IN VISUAL AREAS ARE CONSISTENT WITH LITERATURE

I took the average center of mass TF tuning and SF tuning of all pixels in each visual area. This gave us an average TF value in each visual area. My results were consistent with trends in the literature (**Figure 3E**). For example, most studies that have measured TF tuning in areas AL and RL found that neurons in both areas have higher average preferred TF and lower preferred SF tuning than neurons in V1. I found that areas AL and RL have a three-fold higher center of mass TF tuning (1.5 Hz) than area V1 (0.61 Hz). Multiple studies have also found that areas LM and PM have lower TF tuning and higher SF tuning than areas AL and RL. I also found that areas LM and PM have lower TF tuning than areas AL and RL.

In **CHAPTER 3**, I further describe how experimental design choices can impact TF tuning, which could help account for the discrepancies between my study and the literature. In this chapter, I find that widefield center of mass TF values are lower than the average preferred TF tuning values measured with 2P.

The largest 2P study that has measured SF and TF tuning in V1 is the Allen Brain Observatory dataset (de Vries et al, 2020). This dataset was very similar to my study; it was collected using 2P imaging in the same Cre-lines, using the same GCaMP6 indicators, and was performed in awake behaving mice. This dataset is also expansive: it contains data from over 80,000 cells.

de Vries et al. (2020) serves as the best comparison with validating my results. While my widefield analysis yielded lower TF values, the relative TF tuning between areas was similar in the Brain Observatory *Cux2-CreER*^{T2}*;CaMKIIa-tTa;Ai93/4* mice compared to my widefield study. While the brain observatory dataset found higher TF values in V1, it found similar values of TF in the higher visual areas. Also, the relative order of TF values between areas was consistent.

2.3.7 THERE ARE TEMPORAL FREQUENCY TUNING GRADIENTS IN OTHER CORTICAL LAYERS AND THALAMIC AXONS

Next, investigated whether gradients were present in other laminar populations. Although the canonical cortical circuit in mice is not as well-defined as in primates (reciprocal connections between layers are common between cortical layers and dLGN projections to all layers have been found), it appears that layer 2/3 gets most of its input from layer 4, which in turn gets input from LGN axons. Layer 2/3 gives input to higher visual areas and also to layers 5 and 6, which then synapse on to higher visual areas. To measure tuning gradients in other cortical layers, I used transgenic mice that express GCaMP6s or CCaMP6f in layer 4, layer 5, and LGN axons: 8 *Rorb-IRES2-Cre;CaMKIIa-tTa;Ai94* (layer 4) , 6 *Scnn1a-Tg3-Cre;Ai93* mice (layer 4),*Rbp4-Cre_KL100*, and 7 *Vipr2-IRES2-Cre;Ai162* (LGN).

Immunohistological experiments Cortical expression of GCaMP in *Vipr2-IRES2-Cre;Ai162* is negligible and 99% of thalamic Cre expression in *Vipr2-IRES2-Cre;Ai162* mice is in the LGN, while the rest is in other thalamic nuclei, including LP (**Supplementary Figure 7**; Zhuang et al., 2019). Cortical z-stacks in V1 and AM reveal no somatic labelling in this mouse line, but the presence of GCaMP labelled cortical processing in both cortical visual areas.

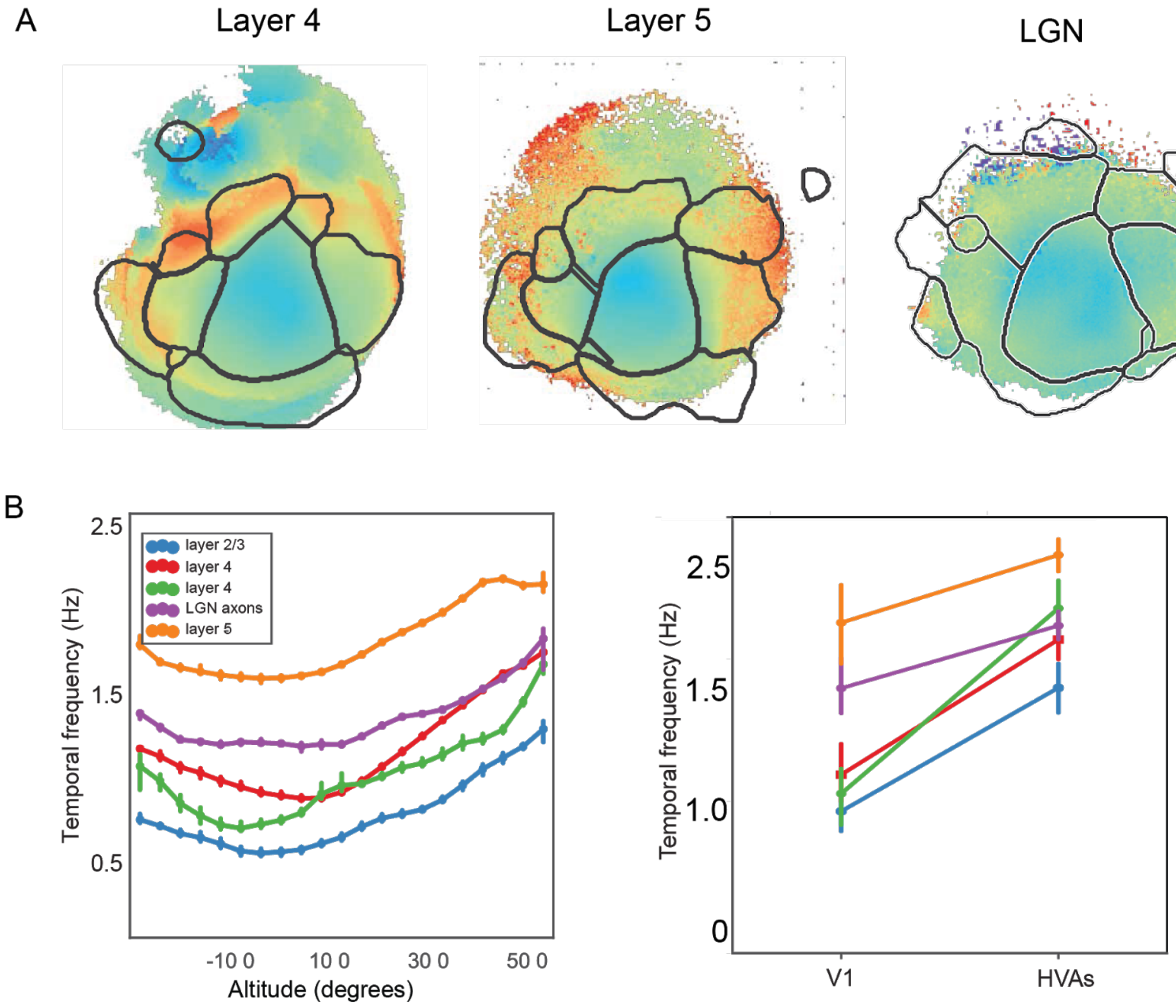

Figure 4) A) From left to right, center of mass TF tuning map in ten *Rorb-IRES2-CreERT2; CaMKIIa-tTa;Ai94,* seven *Rbp4-Cre_KL100;Ai93* mice, and 9 *Vipr2-IRES-Cre*;*Ai62* mice. **B)** Left - Average center of mass TF tuning at each 5 degree altitude bin in V1 in all Cre-lines. Right - Average center of mass TF tuning in pixels in V1 compared on average center of mass TF tuning in all higher visual areas.

The center of mass TF tuning maps in other cortical layers were very similar to the center of mass TF tuning maps in layer 2/3 (**Figure 4A**). Again, the lowest point in the center of mass TF tuning map was in V1 and the TF increased outward toward the edges of V1 and into higher visual areas.

In layer 4, 5, and in thalamic afferents, the slope of the TF tuning gradients in V1 and higher visual areas were the same as in layer 2/3. In **Figure 4B**, left panel, I plotted the median TF tuning in each 5 degree altitude bin in V1 for all layers. The slope of TF tuning versus altitude in V1 is preserved in all layers and in thalamic afferents. In all visual areas in all laminar populations, TF tuning was lowest in the anterior portion of V1 (lower visual field) and highest in posterior V1 (upper visual field). As there are gradients of TF tuning measured in *Vipr2-IRES-Cre*;*Ai162* mice, it is likely that TF information, and gradients, in both V1 and higher visual areas are inherited from dLGN axons, though it is also possible that LP axons contribute to the signal in HVAs..

Encouragingly, two Cre-lines that measured TF tuning in layer 4 (*Scnn1a-Tg3-Cre;CaMKIIa-tTa;Ai93* and *Rorb-IRES2-Cre;CaMKIIa-tTa;Ai94*) did not have significantly different average TF tuning. I compared the distribution of the center of mass TF tuning in pixels in V1 and higher visual areas (Mann Whitney U test, $p > 0.1$).

TF tuning was lowest in layer 2/3 maps, followed by layer 4, followed by layer 5. Thalamic axons had the highest TF tuning of all cortical layers. In mouse visual cortical areas, visual information is relayed primarily to layer 4 via the thalamus and out from layer 2/3 and layer 5. Our results indicate that in both V1 and HVAs, temporal frequency information is lost at each step in the mouse cortical circuit (**Figure 4B – left**).

TF tuning was highest in higher visual areas than V1 in all Cre-lines used, except in *Vipr2-IRES2-Cre;Ai162* (**Figure 4B – right**). Pixels located in higher visual areas in *Vipr2-IRES2-Cre;Ai162* passed our signal-to-noise criteria threshold, indicating that there were significant responses measured with widefield in higher visual areas. This data indicates that thalamic information may be responsible for establishing TF gradients in cortex.

2.4 DISCUSSION

In this section, I report three key findings: (1) the processing of SF and TF tuning is asymmetric across the visual field, (2) This asymmetry is preserved across layers, even though the average SF and TF tuning across layers changes in magnitude, (3) Although temporal frequency tuning is different between higher visual areas, it doesn't change abruptly across areal borders.

2.4.1 2P AND WIDEFIELD SIMILARITIES AND DIFFERENCES

Both widefield and 2P measurements of the temporal frequency tuning of visual cortical areas revealed TF tuning gradients in V1 and higher visual areas. However, the 2P pooled somatic signal reported lower TF tuning than the widefield signal at similar altitude locations. There are several potential reasons for the discrepancies between widefield and 2P: (1) neuropil contamination, (2) contamination from regions and layers from scattering, (3) different neuronal subpopulations selected for by 2P and widefield techniques.

It is possible that different neuronal subpopulations are selected for by widefield and 2P calcium imaging. Selecting different percentages of cells from a larger population based on how responsive and reliably activated they are to visual stimuli significantly changes the reported TF tuning. In **CHAPTER 3,** I quantify the effect of applying different inclusion criteria on a large population of cells on the reported TF tuning.

Most inclusion criteria in the literature select for distinct but overlapping neural subpopulations, indicating that they are using similar metrics to select for responsive neurons. As discussed further in **CHAPTER 3,** the inclusion criteria that I chose also used responsiveness (a response threshold) and reliability (a threshold on the number of responses that reached threshold; see **METHODS**), so I assumed that a similar sensitivity curve to that described in **CHAPTER 3 Figure 4** would hold, given that my experimental setup was similar in both sets of experiments. I assumed that in V1, the most responsive cells would have higher TF tuning than the whole neuronal population. My inclusion criteria selected for 55% of all segmented neurons, and according my analysis in **CHAPTER 3, Figure 4**, the TF tuning of neural subpopulations changes only 5% if 55% of cells are chosen compared to the entire population. I hypothesized that widefield calcium imaging would be equivalent to setting no response threshold and including all neurons in the analysis. If both assumptions are correct, the widefield and 2P results should have diverged little, and the widefield TF measurements, at least in V1, should have been lower than the 2P TF measurements on average.

However, it is also possible that widefield is a less sensitive technique than 2P imaging and selects for a more visually responsive population than 2P imaging. This may account for the higher TF tuning in my widefield results.

Regardless of whether widefield is biased to detect fluorescence in a different neural subpopulation than 2P imaging, it is possible to measure differences in tuning properties across visual areas with both techniques. In both widefield and 2P imaging, I saw differences of comparable magnitude in TF across altitude in V1, giving me confidence in the presence of gradients of TF in visual cortex and widefield's ability to detect them.

While we reported different absolute TF tuning values with 2P and widefield imaging, both modalities allowed us to measure the differences in TF tuning between neurons with receptive fields in the upper and lower fields of view.

Signals from dendrites from cells in V1 and feedforward and feedback connections from other cortical regions contribute to the widefield signal. It is possible that neuropil in visual areas has a higher temporal frequency tuning on average than the somatic signal, resulting in a higher overall TF tuning in the widefield signal. LGN axons and higher visual areas, which carry feedforward and feedback information to V1, respectively, both have higher TF tuning than layer 4 axons, it’s possible that processes in layer 4 are tuned to higher TF than the soma.

Unlike widefield, 2P provides optical sectioning — using widefield, a point on the cortical surface can capture fluorescence from a large 1-2 mm cubed brain region underneath the cortical surface centered on that point. This means that fluorescence from other layers, could be causing discrepancies between widefield and 2P. I used genetically-labeled lines that expressed GCaMP6 specifically in one cortical layer and tested the TF tuning in various depths in the anterior part of V1 and found no significant differences in the TF tuning between layers in a single Cre-line. It is possible that in other regions of V1 and in higher visual areas, there are laminar differences in TF in the population of cells and processes that are labeled in neocortex in a transgenic line. It’s possible that in higher visual areas or in other regions, laminar differences contribute to differences in the TF tuning between widefield and 2P measurements.

2.4.2 CONFIDENCE IN GRADIENTS IN OTHER AREAS OUTSIDE OF AM, V1

There are various biological and technical factors that might affect the accuracy of gradients in TF. First, since widefield does not provide optical sectioning and captures fluorescence from a large cortical volume, scattering and fluorescence sources from other layers is a concern.

Second, neuropil signal in widefield might alter the gradient making it deviate from the somatic tuning. Lastly, signal to noise varies across the field of view, since neurons in primary visual cortex respond better to periodic stimuli and there are differences in fluorescent labeling across Cre-lines.

I only verified the presence of TF tuning gradients in higher visual area AM, but used widefield tuning to measure TF tuning in all higher visual areas on the cortical surface that were responsive to drifting grating stimuli. How confident can I be in the TF tuning of higher visual areas?

GCaMP labeling varies across visual cortex in some Cre-lines, such as *Rorb-IRES2-Cre;CaMKIIa;Ai94* (Harris et al., 2019). In some lines, cellular labeling is less dense and per-cell GCaMP expression is lower in higher visual areas, which affects the signal to noise in higher visual areas. However, gradients and the overall TF and SF maps in Cre-lines that don't have a lower density of labeling in HVAs are similar to those in *Rorb-IRES2-Cre;CaMKIIa;Ai94*. It is unlikely that signal to noise differences could alter the gradient, since based on my modeling data, the ratio of fluorescence between V1 and a higher visual area would need to be very low for scattering from V1 to alter the gradient in AM.

Based on my modeling data, the inconsistencies between widefield and 2P appear not to be due to scattering effects, but a more biologically accurate model, such as one that incorporates the differences in fluorescence throughout the cortical column in V1 and higher visual areas, would allow for a more rigorous comparison.

Widefield captures the slope of the TF gradient in V1 and AM, meaning it can likely capture this relationship in other areas. However, the location of the TF reversal reported in V1 is less clear. From both my 2P and widefield data, it appears that the reversal occurs in anterior V1.

To compare where the reversal of the TF gradient occurs with relation to the AM/V1 border, I fit a quadratic equation using a least-squares optimization function. It revealed that the gradient measured in the 2P and widefield data reverses in V1. However, it is possible that the reversal still happens at the border between V1 and AM, and that although there is a gradient in both areas, the temporal frequency tuning in AM is higher than V1, making the reversal appear as if it is in V1, when in fact both areas contain gradients with the same sign slope (negative) in relation to altitude. This would mean that a quadratic equation is a poor choice for determining where the AM/V1 border is.

2.4.3 HOW DO HVAS GET THEIR TUNING?

How do higher visual areas get their higher TF tuning? Glickfeld et al. (2011) showed that projections in V1 are functionally specific and match the TF tuning of their downstream targets, but another study showed that when LP is lesioned, higher visual areas lose their higher TF tuning. The latter theorized that the high temporal frequency tuning found in higher visual areas is due to input from the lateral posterior nucleus of the thalamus (LP). However, my results showed that gradients in V1 and some higher visual areas are likely due purely to dLGN inputs. Previous tracer experiments have shown that dLGN provides input to V1 and LM, but there is no evidence of direct projections from dLGN to HVAs. I found that gradients in HVAs and V1 could be found in *Vipr2-Cre-neo;Ai162* mice, which express GCaMP6 in dLGN neurons. These mice do express a small amount (<1%) of GCaMP6 other thalamic nuclei, including LP, which could be driving responses in HVAs. Further study is needed to unambiguously provide evidence for the thalamic circuit establishing TF tuning higher visual areas.

2.4.4 GRADIENTS OF TUNING COULD BE DUE TO GRADIENTS OF DIFFERENT CELL AND RECEPTOR TYPES IN RETINA, THALAMUS, CORTEX

The mouse has over 30 retinal ganglion cell types, many of which are unevenly distributed across the retina. So-called predator-detecting W3 cells, which are thought to respond to object motion, are clustered in the ventral retina (upper visual field) (Zhang et a., 2012). One class of directionally selective-RGCs (dsRGCs) are more densely-expressed in the ventral retina (upper visual field), while alpha-like ON-RGCs are more densely-clustered and smaller dendritic diameters in the ventral-nasal part of the retina (Bleckert et al., 2014; El-Danaf et al., 2019).

A potential circuit that could explain my results involves ON-OFF dsRGCs that originate in the retina, synapse onto the dLGN shell and transmit information to layer 2/3 of V1. It is unclear whether this information is also passed onto layer 4. These cells are selective for high temporal frequency information and the posterior direction of motion (Rasmussen & Yonehara, 2018), and could result in the high TF tuning in the posterior visual field, if these cells are preferentially activated with full-field drifting gratings.

From the density and dendritic diameter of ON-RGCs, one might expect that the SF tuning of neurons in the upper nasal portion of the visual field in V1 and higher visual areas might have higher SF tuning. While I did see that the upper part of the visual field was more responsive to higher SFs, I didn’t see a nasal-to-temporal difference in SF tuning differences across V1 and the gradient of SF tuning was weak overall.

Other retinal ganglion cells with unequal distributions might be responsible for the differences in the TF tuning across visual cortex. The distribution of many retinal ganglion cells in the mouse retina has yet to be studied, especially with regard to which subcortical and cortical circuits they are involved in.

There is also an asymmetric distribution of photoreceptors in the mouse retina. The mouse retina is rod-dominated but UV-sensitive S-cones are clustered in the ventral retina, while green light sensitive M cones are clustered in the dorsal retina. In most laboratory conditions, the temporal sensitivity of S-cones is significantly lower M-cones. However, when UV stimuli are used, the temporal sensitivity of S-cones increases significantly. Using UV stimuli might reveal further functional specialization in the retina and cortex (Wang et al., 2011; Umino et al., 2008). It is unlikely that in the experimental conditions, S-cone mediated responses were responsible for the difference in temporal frequency tuning properties across visual cortex.

2.4.5 DIFFERENCES IN FUNCTIONAL SPECIFICITY ACROSS VISUAL FIELD

There are clear differences in functional properties across the mouse visual field. Neurons in the upper part of the visual field have higher TF tuning than the lower part of the visual field.

In mice, there are maps of functional properties within visual areas and across visual areas. Coherent motion, for example, is processed asymmetrically in visual space and across the visual cortex (Sit & Goard, 2020). It appears TF and SF may be similarly asymmetric. In addition, unlike in primates, TF tuning is processed in a global manner with no abrupt changes in tuning across areal borders. This has previously been found in mice, with other behaviorally-relevant stimulus features.

Why might the upper visual field be functionally specialized to detect fast moving, high SF stimuli? One hypothesis might be that the mouse thalamic visual circuit overall might be specialized for detecting fast moving, high SF stimuli in the upper visual field. This might benefit mice in predator detection.

2.5 SUPPLEMENTAL FIGURES

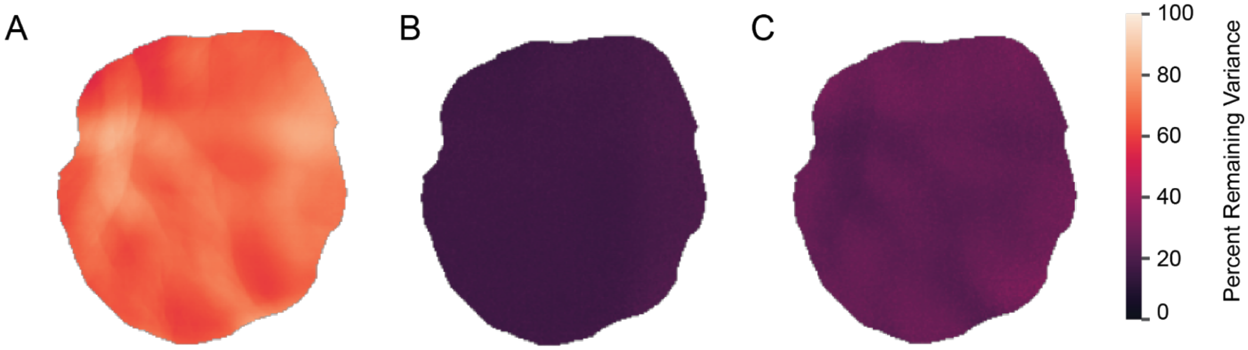

Supplementary Figure 1. A) Variance in one *Cux2-CreER^{T2};Ai140* animal. **B)** Percent remaining variance after two-wavelength hemodynamic correction **C)** Percent remaining variance after one-wavelength hemodynamic correction

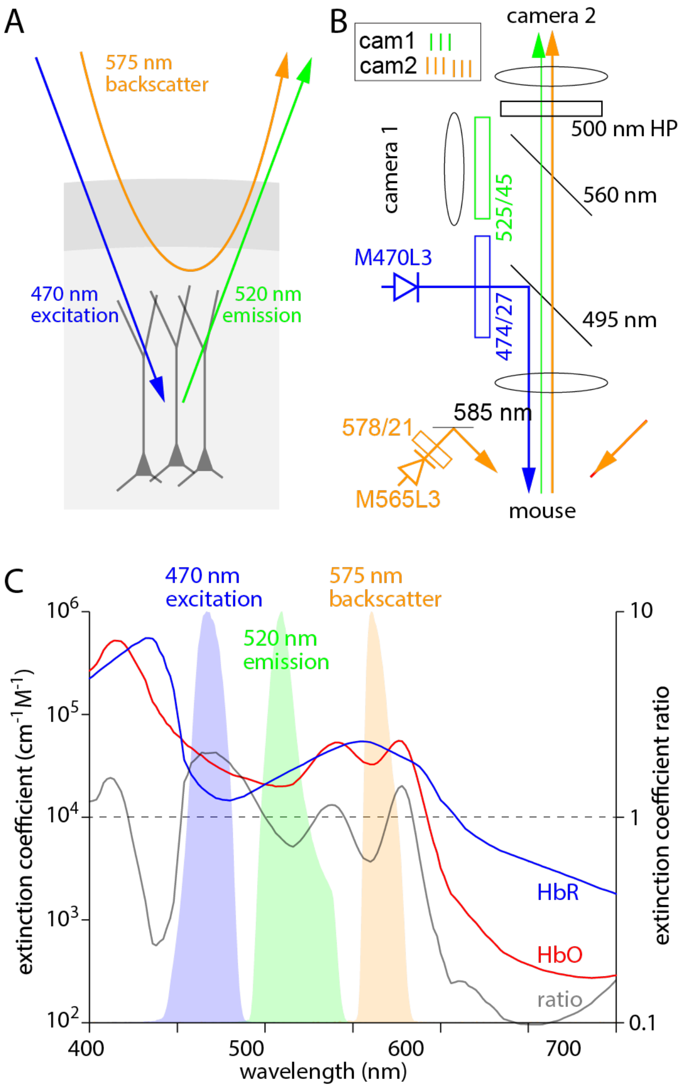

Supplementary Figure 2. (A) Schematic illustration of strategy to estimate absorption of GCaMP excitation and emission (centered at ~470 and ~520 nm, respectively) and of illumination at ~577 nmby hemoglobin. Blue illumination is susceptible to absorption when in transit from the LED to the neurons expressing GCaMP. Green fluorescence emission is susceptible to absorption while in transit from GCaMP molecules to the fluorescence camera. 577 nm illumination are susceptible to absorption during entry and during exit from the brain, before and after the scattering events that result in diffuse reflection. (B) Schematic illustration of simultaneous fluorescence and backscatter measurements, with relative locations and wavelength characteristics of LED sources, filters, lenses, dichroic mirrors and cameras (see figure S5 for a rendering of the microscope assembly). Camera frame interleaving sequence (inset, upper left) shows the continuous acquisition of fluorescence on camera 1, and strobing between detection of 577 nm backscatter and a blank frame on camera (C) Absorption spectra of oxy- and deoxyhemoglobin (HbO and HbR; left axis) in the visible spectrum, the HbO/HbR extinction coefficient ratio (right axis), and normalized spectra of wavebands used in my experiments.

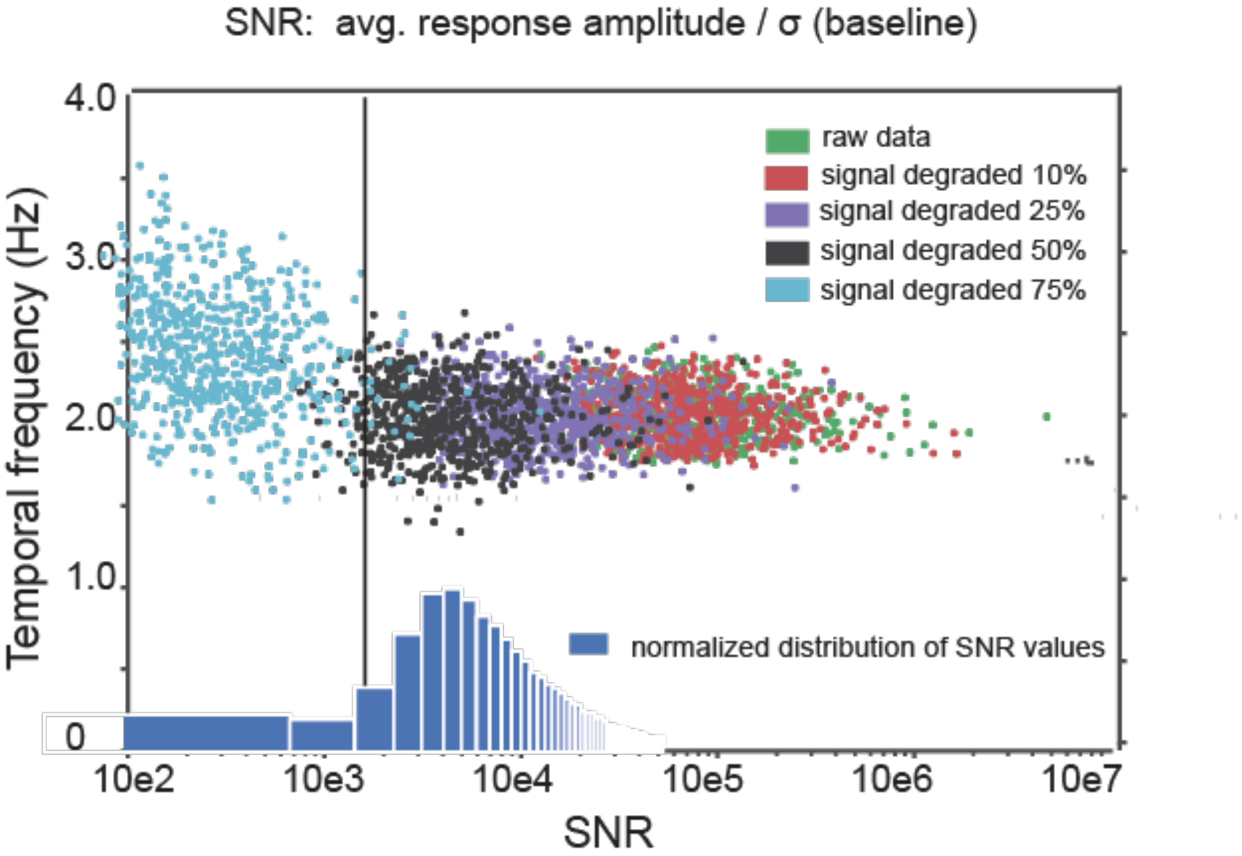

Supplementary Figure 3. Method by which I eliminated unresponsive pixels. In one example animal, a 20 x 20 pixel square in V1. Green pixels show signal to noise (mean event-triggered response divided by signal to noise of event triggered responses) and temporal frequency of raw data. Other colors show SNR and temporal frequency of the same data artificially degraded by white noise. Signal to noise was degraded 25, 50, and 75 percent of original value. Histogram on X axis is the count (normalized to 1) of pixels with certain signal to noise throughout the entire window.

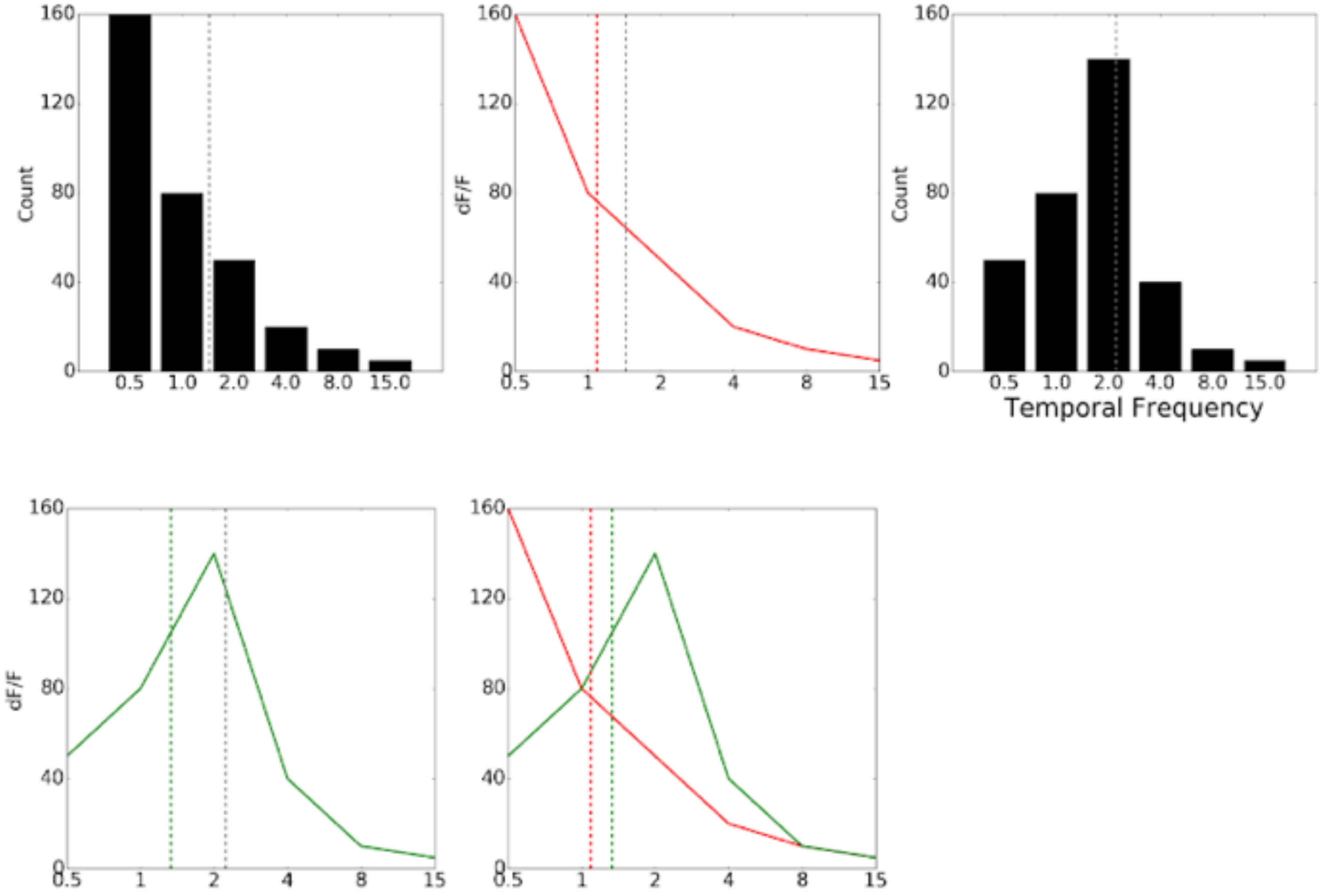

Supplementary Figure 4. Schematic of center of mass analysis versus underlying populations. (A) Schematic. Histogram of preferred TF tuning of population of neurons skewed to low TFs. Grey dashed line is mean preferred TF of population. (B) Resulting population tuning curve if all responses from neurons in population are equal (also assumes neuron is only tuned for one TF). Red dashed line is center of mass TF, grey dashed line is mean preferred TF from population in (A) (C) histogram of preferred TF tuning of a population. Grey dashed line is the mean TF of population. (D) Resulting population tuning curve (green solid line) if all responses from neurons in population are equal, green dashed line is center of mass TF, grey dashed line is mean preferred TF from population in (C). (E) Comparison of center of mass values from two distributions.

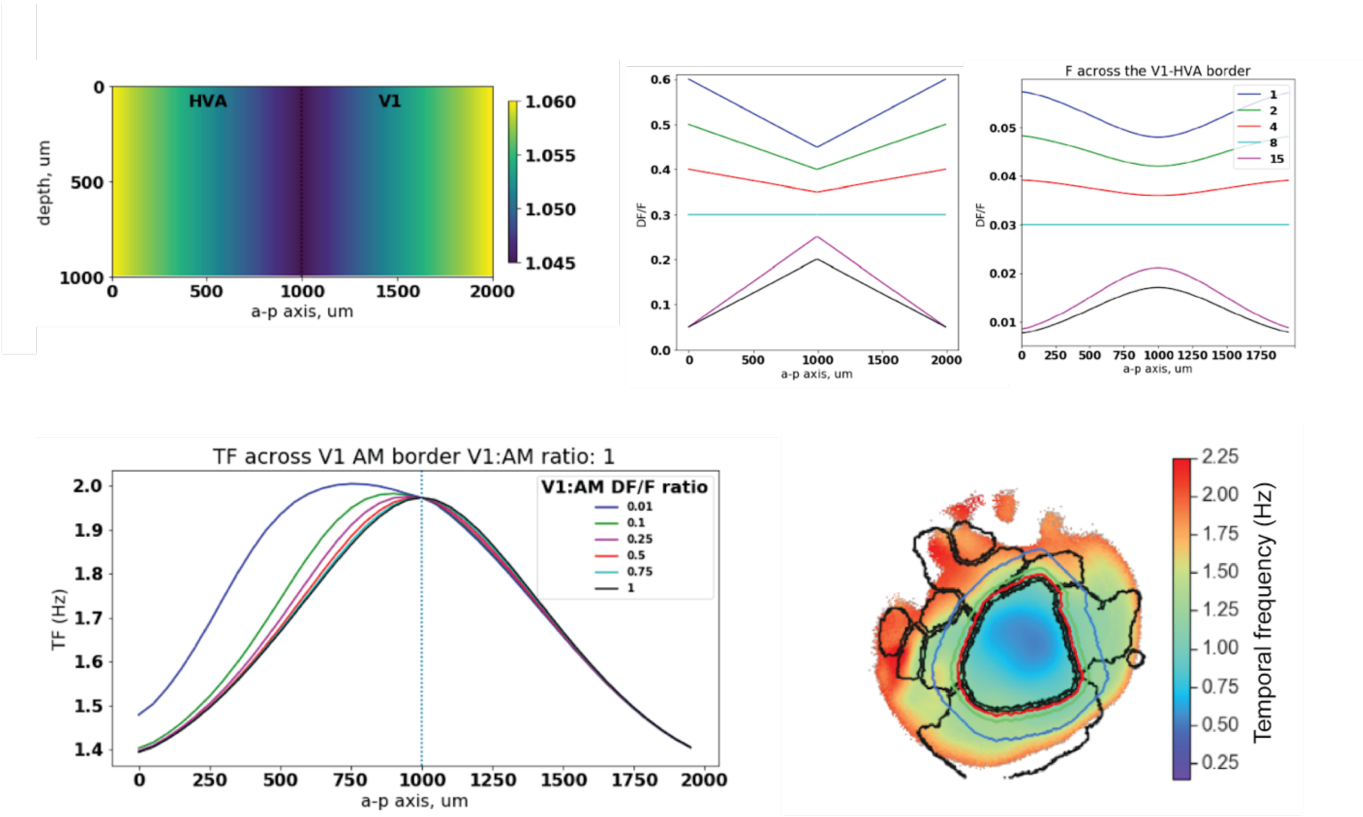

s

Supplementary Figure 5. Model of TF throughout cortical depth of 700 um of cortical tissue in mouse visual cortex after monte-carlo widefield model has been run. A) Model of fluorescence in V1 and AM in response to 0.5 Hz stimulation, assuming equivalent gradient in V1 and AM and gradient reversal at V1 AM border. B) Fluorescence at cortical surface AM and V1 in response to stimulation at various TFs, assuming gradients of the same but opposite slopes with distance from the center of V1 before model is run (left) and after model is run (right). The TF tuning if AM and V1 assuming responses in (B) after model is run, assuming different fluorescence ratios between AM and V1. D) the location of the gradient reversal in relation to the V1 AM border. Outline of where modeled reversal would be if the signal in AM was 0.5 (red) 0.1 (green) and 0.01 (blue) the fluorescence amplitude of the signal of V1. Underlying map is a center of mass temporal frequency tuning map.

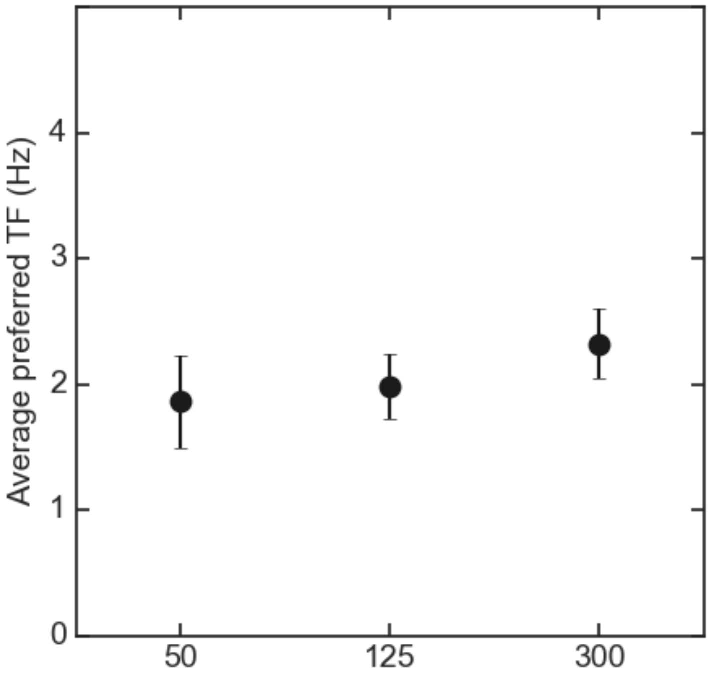

Supplementary Figure 6. Average preferred TF tuning measured at three cortical depths: 50 um, 125 um, and 300 um below pia in *Rorb-IRES2-Cre;CaMKIIa-tTa;Ai94* mice. Only processes and boutons were found at shallow cortical depths.

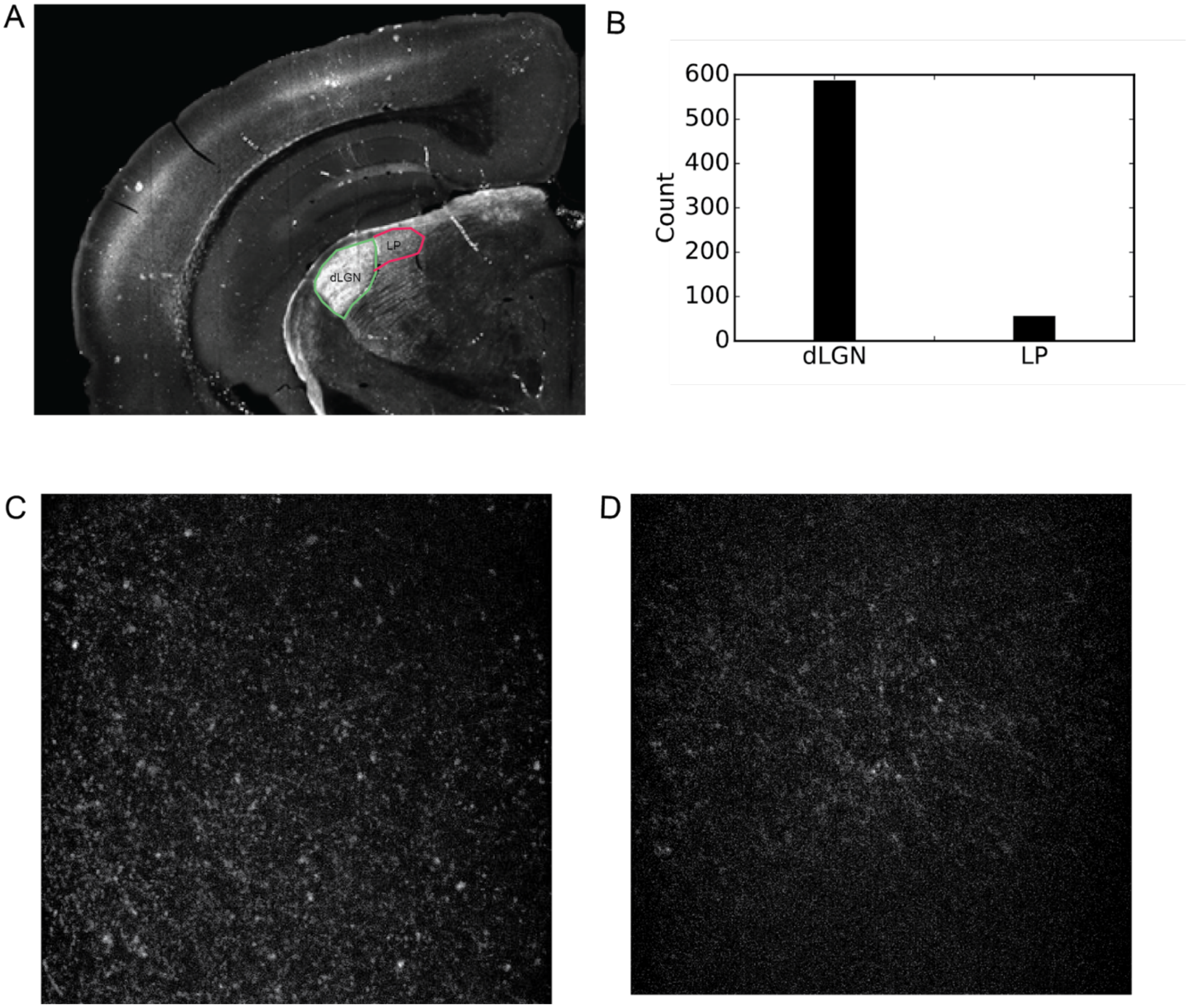

Supplementary Figure 7. A) Fluorescence 2P tomography image of GCaMP fluorescence in *Vipr2-Cre-neo;Ai162* mice. **B)** Number of GCaMP-labelled cells in dLGN vs LP **C)** Average intensity z-stack of 2P fluorescence images of anterior V1 showing labelled axons through 50-500 microns below pia. **D)** Average intensity z-stack 2P fluorescence images of anterior V1 showing labelled axons through 50-500 microns below pia

3. CHARACTERIZING THE EFFECT OF INCLUSION CRITERIA ON BASIC TUNING PROPERTIES IN MOUSE VISUAL CORTEX

3. ABSTRACT

Neurophysiology studies require the use of inclusion criteria to identify neurons responsive to the experimental stimuli. Five recent studies used calcium imaging to measure the preferred tuning properties of layer 2/3 pyramidal neurons in mouse visual areas. These five studies used different experimental designs that employed different inclusion criteria and report different, sometimes conflicting results. Experimental design choices and inclusion criteria both affect the subpopulation of neurons that are selected for. Here, I examined how different inclusion criteria can impact reported tuning properties, modifying inclusion criteria to select different sub-populations from the same dataset of almost 17,000 layer 2/3 neurons from the Allen Brain Observatory. The choice of inclusion criteria greatly affected the mean tuning properties of the resulting sub-populations; indeed, the differences in mean tuning due to inclusion criteria were often of comparable magnitude to the differences between studies. In particular, the mean preferred temporal frequencies of visual areas changed markedly with inclusion criteria, such that the rank ordering of visual areas based on their temporal frequency preferences changed with the percentage of neurons included. These results demonstrate that the current understanding of the functional organization of the mouse visual cortex obtained from previous experiments critically depends on the inclusion criteria used.

3.1 INTRODUCTION

3.1.1 SUMMARY

In this thesis, I am interested in how receptive field properties (spatial frequency [SF] and temporal frequency [TF]) are mapped in visual space. In **CHAPTER 2**, I used 2-photon (2P) calcium imaging to measure SF and TF tuning in visual areas. However, 2P calcium imaging studies can produce a wide range of different results — previous 2P calcium imaging studies in mouse visual cortex report widely different mean values of SF, TF, orientation selectivity, and directional selectivity tuning of visual areas. These values vary up to four-fold between studies. The differences between studies are likely due to differences in the experimental design and/or data analysis.

Experimental design and analysis choices can inadvertently change the population of neurons that are included in the experimental analysis, which can then alter the apparent tuning of the neural population that is being studied. Experimental design choices, such as the calcium indicator used or the anesthesia state of an animal, can change the apparent signal to noise of the stimulus response, altering either the response strength, the reliability of the response, both, or how well the response can be detected. How different experimental design choices alter response strength and reliability, and how this could affect tuning, is discussed in detail in section 3.1.4.

In the field, we currently don't have an understanding selecting different neural populations based on their signal to noise correlates with different tuning metrics. In this study, I encompass the strength and reliability in a single metric called robustness, which is defined in detail in section 3.1.3 of this chapter. To measure tuning properties in the visual cortex, I need a quantitative understanding of how tuning metrics change with robustness.

It is impractical to study how all different experimental design choices alter tuning, but it is possible to select for different subpopulations of neurons out of a larger population based on their robustness. This is what I've done in the following study.

In the following sections, I elaborate how experimental design choices and the choice of inclusion criteria can alter the apparent robustness of neurons in visual cortex and how this might have impacted the reported tuning in previous studies.

This chapter of my thesis is about this study, *Characterizing the effect of robustness of tuning metrics in mouse visual cortex*, published in eNeuro. In the discussion, I will consider the implications of the choice of inclusion criteria used in the rest of my thesis on the characterization of TF tuning (Mesa et al., 2021).

3.1.2 WHY 2P?

The main alternative used to measure tuning fundamental tuning metrics in mouse neurophysiology is electrophysiology. There are several advantages of 2P imaging. First, 2P has been used previously in several studies that have measured fundamental tuning properties. This allows for direct historical comparisons.

High-throughput electrophysiological recordings in cortex designed in recent years allow for high numbers of cells (> two thousand) to be recorded from multiple depths in a single session. In comparison to high-throughput methods such as neuropixels probes, 2P yields more cells. While a single neuropixels probe can record more cells than previous recording methods, the failure rate of units in a probe makes it so that the yield is less than 2P. 2P also affords greater spatial coverage of the cortex, while neuropixels probes require multiple probes in one animal to image multiple locations. The other is that, with 2P, one has the ability to image chronically, which again allows us to image in multiple locations in one animal without using multiple probes. When using high-yield probes, like neuropixels, experiments are typically acute (Siegel et al., 2021).

3.1.3 DISCREPANCIES BETWEEN STUDIES IN THE ABSOLUTE VALUE AND RANK ORDER OF TUNING METRICS IN VISUAL AREAS

There have been five recent studies that have employed 2P calcium imaging to measure SF and TF, as well as orientation selectivity and directional selectivity, in the visual cortex (Andermann et al. 2011; Marshel et al., 2011; Roth, Helmchen, and Kampa 2012; Tohmi et al. 2014; Sun et al. 2016). The results from these studies vary widely Some results were consistent across studies, e.g. the mean preferred TF of neurons in area AL was greater than those in V1 (**Figure 1A**), but there were also differences between studies, e.g. some studies found that the mean preferred TF of neurons in PM was greater than those in V1 while others found the opposite. Further, the magnitudes of average TF tuning, orientation selectivity index (OSI), and direction selectivity index (DSI) in individual visual areas as well as the rank order of these properties between visual areas differed across studies. All five studies imaged in layer 2/3 of mouse visual neocortex and responses were evoked using a drifting grating stimulus.

What accounts for the differences between previous studies? Studies used different experimental design choices, such as stimulus parameters, anesthesia state, and calcium indicators any of which could alter apparent robustness. Studies must also apply inclusion criteria to select responsive neurons and eliminate noisy ones. All of the studies and a summary of their different experimental designs are listed in **Table 1.**

Paper	**Anesthesia**	**Indicator**	**Stimulus**	**Responsiveness Criteria**	**Percentage of Responsive Cells**	**# Cells Allen Brain Observatory**
Study 1 **Sun *et al.* (2016)**	None	GCaMP6s	12 s full-field square grating TF: 0.5 Hz, 1 Hz SF 0.05 cpd 8-16 directions	• Mean ΔF /F > 10%	49% (n = 1279/2609)	19.2% (n = 1883/9818)
Study 2 **Roth *et al.* (2012)**	Urethane	OGB-1	5 s full-field sine wave grating TF: 0.5, 1, 2, 4 Hz SF: 0.01, 0.02, 0.04,0.08, 0.16 cpd 8 directions	• In 50% of trials, mean ΔF/F > baseline + 3σ • Mean response > 5%	44% (n = 399/973)	6.12% (n = 601/9818)
Study 3 **Andermann *et al.* (2011)**	None	GCaMP3	40 degree sine wave grating patches TF:0.5, 1, 2, 4, 8, 15, 24 Hz SF: 0.02, 0.04, 0.08, 0.16, 0.32 cpd Direction: upward	• T-test comparing grating response with blank sweep with Bonferroni correction ($p<0.05/n$)	8% (n = 28/340)	29.6% (n = 2909/9818)

Study 4 **Marshel *et al.* (2011)**	Isofluorane	OGB-1	4 s full-field sine wave gratings SF: 0.01, 0.02, 0.04, 0.08, 0.16 cpd TF: 0.5, 1, 2, 4, 8 Hz 8 directions	• Mean ΔF/F > 6% • reliability >1 *	42% (n = 586/1395)	6.18% (n = 607/9818)
Study 5 **Tohmi *et al.* (2014)**	Urethane	Fura-2	5 s ramping square and sine wave gratings SF 0.05 and 0.1 cpd 8 directions	• Max ΔF/F > 5%	41.2 % (n = 142/347)	96.2% (n = 9449/9818)

Table 1. Summary of the experimental conditions and inclusion criteria used in published studies. Last column shows the number of neurons selected from the Allen Brain Observatory.

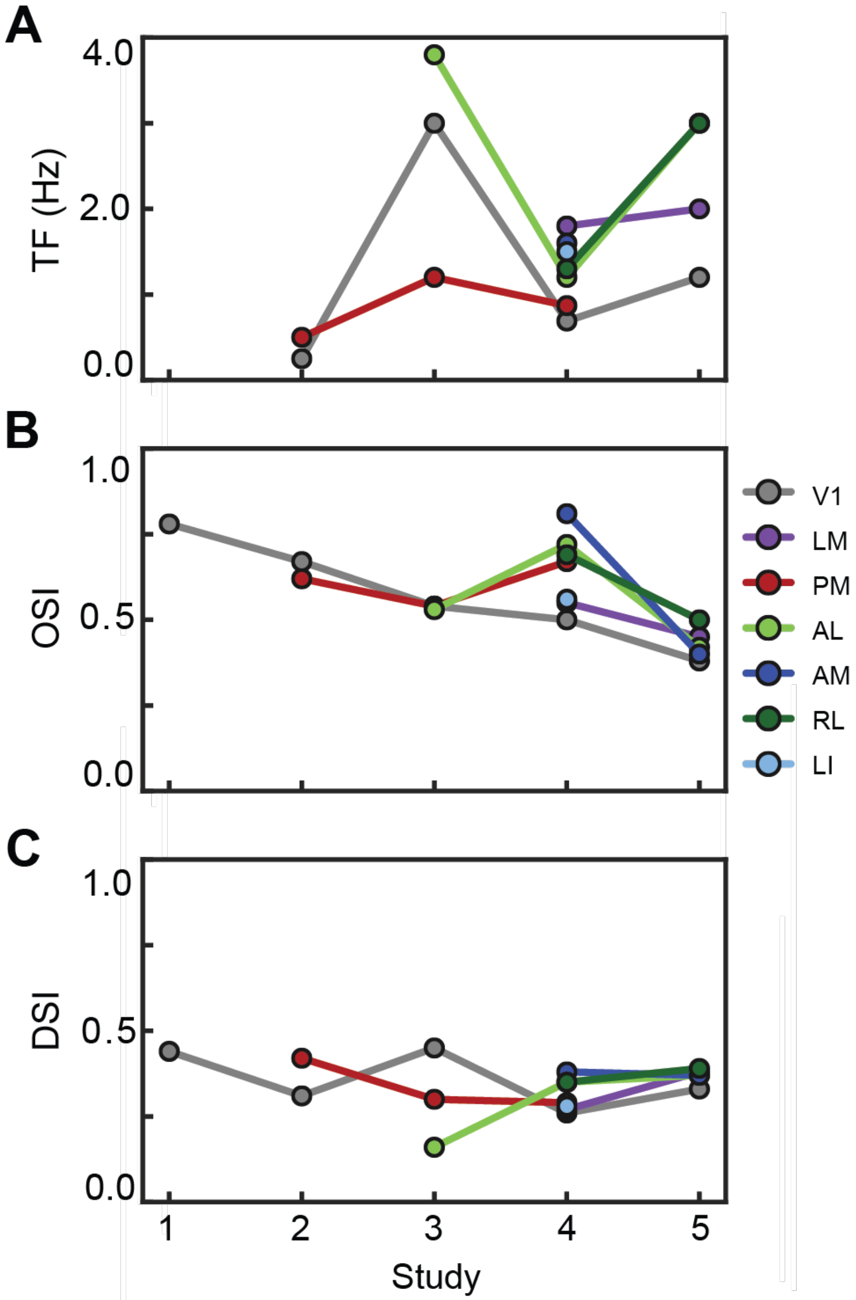

Figure 1. Tuning characteristics in published studies. **A)** Mean preferred temporal frequency (TF) tuning of seven visual areas reported in five published studies. **B - C)** Same as in A, but reporting the orientation selectivity index (gOSI) and the direction selectivity index (DSI).

3.1.4 EXPERIMENTAL PARAMETERS ALTER THE POPULATION OF NEURONS INCLUDED IN THE ANALYSIS

There is inherent variability to how strongly and reliably neurons respond to stimuli in the visual cortex. There are some neurons that respond strongly and consistently to visual stimulation and others that are still tuned but respond weakly or inconsistently to visual stimulation. Naturally, some neurons exhibit large-amplitude changes in fluorescence on every trial in response to a preferred stimulus and fulfill both amplitude and reproducibility criteria (**Figure 2A-C**). Many neurons display reproducible, small-amplitude changes (**Figure 2D-F**) or large-amplitude changes in fluorescence on only some trials (**Figure 2G-I**). Although not often used as the basis for inclusion criteria, other features of the fluorescence traces, such as periodicity in the fluorescence in response to a periodic stimulus such as a drifting grating (**Figure 2I**) and tuning to stimulus characteristics such as orientation and temporal frequency (**Figure 2C, H, I**), may also be suggestive of stimulus-evoked activity (Glickfeld et al., 2013; Neill & Stryker, 2008).

To measure how strongly and consistently neurons respond to visual stimuli, I used a metric of robustness to measure reliability and responsiveness. I defined robustness as the standard deviation of the response to the preferred stimulus divided by the mean peak df/f to the preferred stimulus, also referred to as the coefficient of variance or CV. I measure whether only including the most robustly responsive neurons in the analysis may lead to a biased measurement of tuning metrics. Some crucial experimental design choices that could potentially alter apparent robustness of neurons are anesthesia state, the choice of stimulus parameters, and the calcium indicator. These can alter the strength of the stimulus response or how well weakly responsive neurons can be detected. The effect each of these factors might have on tuning is discussed in detail below.

In the following three sections, I describe how the choice of stimulus parameters, anesthesia, and calcium indicator can influence reported tuning metrics.

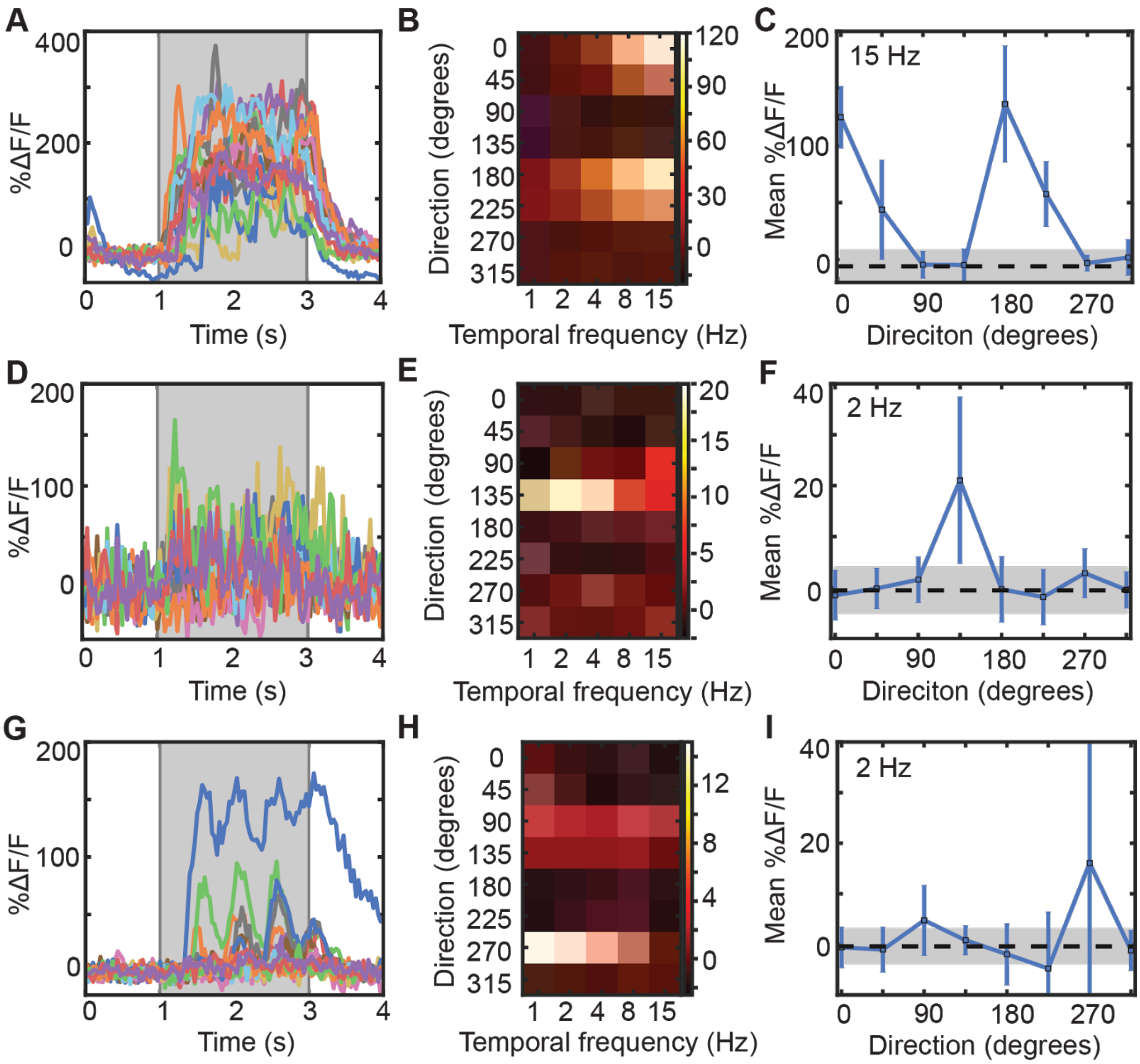

Figure 2. Examples of cells that pass inclusion criteria exclusively. **A)** All ΔF/F responses to the preferred stimulus condition (TF & direction) of a cell that passes all published inclusion criteria. **B)** Heatmap of mean %ΔF/F responses to each stimulus condition (TF x direction). **C)** Mean %ΔF/F responses to stimuli of different grating directions in the same example cell. **D-F)** Same as in A, but with a cell that passes most criteria, but not Study 2. **G-I)** Same as in A, but with a cell that only passes Study 1 criteria.

3.1.4.1 STIMULUS PARAMETERS MAY CAUSE DIFFERENCES IN TUNING METRICS

Suboptimal stimulus parameters may cause weakly responsive neurons to appear unresponsive. Additionally, interactions between stimulus features can also alter the apparent tuning of neurons. For example, the orientation selectivity of neurons in V1 is dependent on the SF of the stimulus, such that non-optimal SFs decrease not just the response amplitude, but also the orientation selectivity of the neurons. Tohmi et al. and Sun et al. used only one SF, but reported the lowest and highest OSI values, respectively, suggesting that there are other factors that contribute to differences in orientation tuning between these studies.

Tohmi et al. also used a ramping stimulus, which could alter the apparent TF tuning through stimulus adaptation, causing the temporal frequency tuning of cells to appear lower than it is. A ramping stimulus could have a similar effect as the contrast gain adaptation to ramping contrast stimulus seen in monkeys, which shifts the apparent contrast response curve (Ohzawa et al., 1985).

Differences in the stimulus parameters between studies could also alter stimulus responses in neurons. Some studies, again Sun et al. and Tohmi et al., used square wave gratings. This type of stimulus contains fourier components of various high frequencies, which could alter response properties of V1 neurons or recruit different neurons (Pollen and Ronner, 1982). However, Tohmi et al. did not see a large difference in the orientation tuning of cells in their study when square waves were used, making this an unlikely explanation for the differences between studies overall.

3.1.4.2 ANESTHESIA STATE CAN ALTER THE APPARENT RESPONSIVENESS OF NEURONS BY CHANGING FIRING RATE

Anesthetics can affect firing rates and tuning metrics. Urethane lowers both the spontaneous and evoked firing rate of neurons, but does not appear to impact OSI (Neill and Stryker, 2008). In contrast, atropine affects OSI but not spontaneous firing rates, evoked firing rates, or DSI. (Durand et al., 2016). Isofluorane anesthesia suppresses firing and decreases DSI, but not OSI (Goltstein et al., 2015). Different anesthetics have different effects. For example, anesthesia such as urethane may decrease evoked firing rates, make weakly responsive neurons silent or undetectable, biasing analyses to more robust neurons. Anesthetics such as atropine and isoflurane do not appear to change firing rates, but still influence the DSI and OSI.

3.1.4.3 CALCIUM INDICATORS CAN ALTER THE SIGNAL TO NOISE RATIO AND POPULATION OF NEURONS CONSIDERED RESPONSIVE

Calcium indicators have different sensitivities and signal to noise properties (Hendel et al. 2008; Chen et al. 2013) and are likely to play a large role in the discrepancies between studies. More sensitive indicators can detect firing events and as such indicators with low sensitivity may discard weakly responsive cells. This is also true of indicators with low signal to noise ratio, which may be unable to detect responses.

Different calcium indicators are known to sample different subsets of the total neuronal population due to their different sensitivities and signal to noise properties. For example, although the signal to noise of transgenically-expressed GCaMP3 is higher, OGB-1 is more sensitive and thus samples more weakly responsive neurons, leading more neurons to be labeled as responsive. The OSI and DSI of the neurons sampled by these two indicators is different (Zariwala et al., 2012). Similarly, like GCaMP3, Fura-2 has a higher signal to noise but is less sensitive at detecting smaller events than GCaMP3 (Miyazaki and Ross, 2015). Both

Roth and Marshel used OGB-1, but reported different values of DSI, leading me to the conclusion that this was not the primary difference for the discrepancies in DSI between studies. However, these two studies did report lower values of TF tuning than other studies, and had more restrictive inclusion criteria, indicating that differences in TF tuning between studies may be due to the use of OGB-1 in these studies.

3.1.5 INCLUSION CRITERIA SELECT NEURONS ON ROBUSTNESS

After maximizing the number of neurons included in the analysis with the previous experimental design choices, one must then establish criteria for how robust a neuron must be to be included in the analysis in order to exclude unresponsive cells or cells whose responses are purely noise. Inclusion criteria must be different study-to-study, depending on the experimental design. For example, inclusion criteria must be appropriate for the indicator used. Many criteria use simple thresholds on peak %df/f which cannot be applied uniformly across different calcium indicators, as they have different sensitivities. Therefore, it is important to pick an appropriate inclusion criterion and understand how sensitive tuning metrics are to changing thresholds for neural responsiveness and reliability.

It is unclear how inclusion criteria affect tuning metrics. Each of the five studies listed above in section 3.1.3 used different inclusion criteria. It is unclear whether these different criteria select for different subpopulations of neurons, and whether these subpopulations have different tuning. Here, I explore the effects of inclusion criteria on results from a single large dataset, eliminating the effects of different experimental conditions. I used recordings from the Allen Brain Observatory, a database of physiological activity in the visual cortex measured with 2P calcium imaging from adult GCaMP6f transgenic mice (de Vries et al., 2020). I found that tuning properties varied with inclusion criteria, in some cases changing the rank order of tuning properties across mouse cortical visual areas.

3.2 METHODS

3.2.1 STIMULUS AND DATASET

I used calcium imaging recordings from the Allen Brain Observatory, a publicly available dataset that surveys physiological activity in the mouse visual cortex (de Vries et al., 2020). I specifically used the responses to the drifting grating stimulus in this dataset. This stimulus consisted of a 2 s grating followed by a 1 s mean luminance grey period. Six temporal frequencies (1, 2, 4, 8, 15 Hz), eight different directions, and one SF (0.04 cpd) were used. Each grating condition was presented 15 times.

Data analysis was performed in Python using the AllenSDK. The evoked response was defined as the mean dF/F during the 2 s grating presentation. Responses to all 15 stimulus presentations were averaged together to calculate the mean evoked response.

I restricted all analyses to cells in layer 2/3 (175-250 um below pia) of transgenic lines *Cux2-CreER*^{T2}*;Camk2a-tTa;Ai93* and *Slc17a7-IRES2-Cre;Camk2a-tTa;Ai93*, which express GCaMP6f in excitatory neuron populations in layer 2/3 and throughout neocortex, respectively. A total of N = 16,923 neurons from 66 mice (42 male, 24 female) were used for these analyses.

3.2.2 METRICS

The preferred direction and temporal frequency condition were defined as the grating condition that evoked the largest mean response. In order to compute the average TF tuning of a population of neurons, these TF values were first converted to an octave scale (base 2), averaged, then converted back to a linear scale and reported.

Directional selectivity was computed for each neuron as:

$$DSI = \frac{R_{pref} - R_{null}}{R_{pref} + R_{null}}$$

where R_pref is the mean response at to the preferred direction and R_null is the mean response to the opposite direction.

Orientation tuning was computed for each neuron using the global orientation selectivity index (OSI), (Ringach et al., 1997) defined as:

$$OSI = \frac{\sum R_{\theta} e^{2i\theta}}{\sum R_{\theta}}$$

Where R_θ is the mean response at each orientation.

The coefficient of variance (CV) was used to determine robustness. CV was calculated for each neuron as the ratio of standard deviation of the 15 responses to the preferred condition (mean df/f over the 2 s stimulus presentation) to the mean evoked response (see above). A low CV would indicate high robustness.

Metrics were either computed using all available trials, or with cross validation. When using cross validation, half of the trials (chosen at random, without replacement) were used to identify the preferred direction and temporal frequency, and the other half of the trials were used to compute the metrics using those preferred conditions. This was iterated 50 times, and the resulting metrics were averaged together.

When examining the effects of the number of trials, for each number of trials (n), n trials were chosen at random (without replacement), and the cross-validation was done as described above.

3.2.3 INCLUSION CRITERIA

Published studies used the following inclusion criteria, which Iapplied to cells in the Allen Brain Observatory Dataset in the following manner:

Study 1: The mean evoked response (df/f) to the preferred stimulus condition is greater than 10%. (Sun et al. 2015)

Study 2: In 50% of trials, the response is (1) larger than 3x the standard deviation of the pre-stimulus baseline and (2) larger than 5% df/f. (Roth, Helmchen, and Kampa 2012)

Study 3: Paired t-test ($p > 0.05$) with Bonferroni correction comparing the mean evoked response during the blank sweeps with mean evoked responses to preferred stimulus condition. (Andermann et al. 2011)

Study 4: (1) The mean response (df/f) to any stimulus condition is is greater than 6%. And (2) reliability>1 where:

$$reliability = \frac{R_{pref} - R_{blank}}{\sigma_{pref} + \sigma_{blank}}$$

(Marshel, Garrett et al. 2011)

Study 5: The maximum fluorescence change (df/f) during the 2 s stimulus presentation block to any stimulus condition was greater that 4%. (Tohmi et al. 2014)

3.3 RESULTS

3.3.1 DIFFERENT INCLUSION CRITERIA SELECTED DIFFERENT, OFTEN OVERLAPPING POPULATIONS OF NEURONS

The five studies listed in **section 3.1.3** employed a range of inclusion criteria, selecting 8-49% of the neurons in their respective studies (**Table 1**). The inclusion criteria were based on one or both of the amplitude and the trial-to-trial variability of the evoked responses and I therefore calculated the mean and standard deviation of the response of each neuron to its peak stimulus condition (the direction and TF that evoked the largest mean response). I applied the five different inclusion criteria to the Allen Brain Observatory, a large 2P calcium imaging data set. Different inclusion criteria selected different, often overlapping populations of neurons (6-94% of 16,923 neurons, Table 1 Column 7), readily visualized by plotting the mean against the standard deviation of the response (**Figure 3A**). The results derived using these different criteria covered similar ranges to those in the published studies, consistent with the idea that effects of inclusion criteria could contribute to the disparate results across published studies (**Figure 3B**).

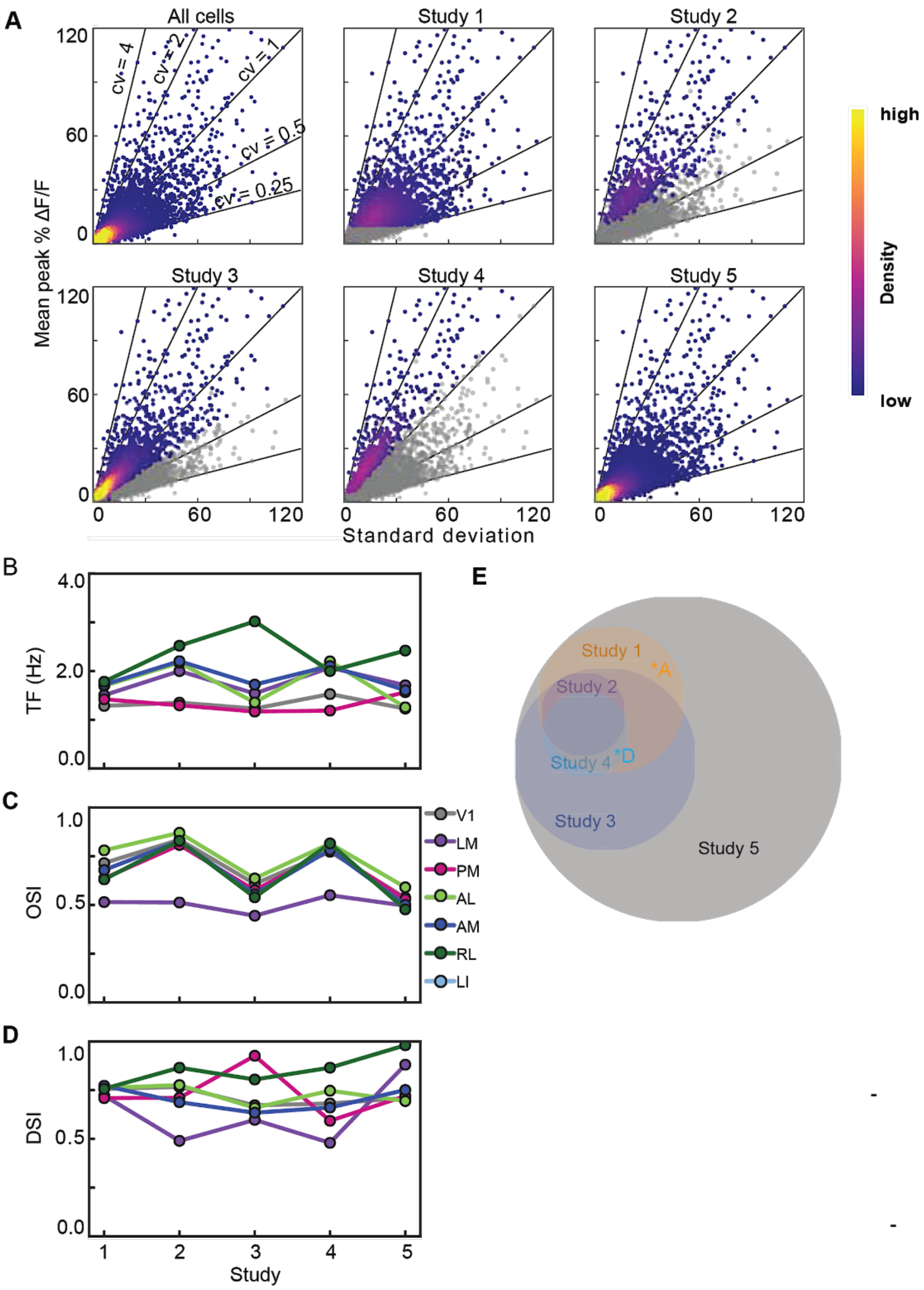
A
All cells
Study 1
Study 2
Study 3
Study 4
Study 5
cv = 4
cv = 2
cv = 1
cv = 0.5
cv = 0.25
120
60
0
Mean peak % ΔF/F
Standard deviation
high
Density
low
B
TF (Hz)
4.0
2.0
0.0
C
OSI
1.0
0.5
0.0
V1
LM
PM
AL
AM
RL
LI
D
DSI
1
2
3
4
5
Study
E
Study 1
*A
Study 2
Study 4
*D
Study 3
Study 5

Figure 3. Most studies select for neurons along similar axes of the data. **A)** Six density plots of the mean response at the preferred stimulus condition (% ΔF/F) against the standard deviation of the responses at the preferred stimulus condition where each point represents a single neuron. For each study, colored neurons are those selected for by inclusion criteria. Heatmap represents the density of neurons. **(B-D)** Tuning characteristics after inclusion criteria are applied to Allen Brain Observatory Dataset. **B)** shows mean TF tuning of six visual areas when different inclusion criteria are applied. **C-D)** show the mean OSI and DSI of six visual areas, respectively. **E)** Venn Diagram of neurons that were selected for by each inclusion criteria. Area of circles represents the number of neurons.

3.3.2 INCLUDING ONLY MOST ROBUST NEURONS IN MY ANALYSIS ALTERED TUNING PROPERTIES

Using coefficient of variation (CV = standard deviation/mean) as a measure of response robustness, I asked how increasing the number of neurons selected, from the most robust (lowest CV) to the least (highest CV), affects the computed tuning metrics. For some metrics, including more neurons affected tuning properties by almost as much as the differences between studies. For example, increasing included neurons changed the mean preferred TF for V1, PM, and AL as well as the rank order of these three areas, such that AL and PM display different mean TFs when only the top decile are included, but have the same mean TF when all neurons are included (**Figure 4A-D, M**). Within V1, the change in mean TF reflects the fact that the highest decile (10% with highest CV) shows a broader distribution of preferred TF than the lowest decile (**Figure 4B, C**). In contrast, the effect on OSI smaller and more consistent across areas, having a smaller effect on the value or the rank order across areas (**Figure 4E-H, M**). Finally, increasing the number of neurons included increased the mean DSI, and did so consistently and significantly across all visual areas (**Figure 4I-L, M**). The increase in DSI reflects the fact that many of the neurons in the lowest decile have a DSI of 1, whereas the neurons in the highest decile have a uniform distribution of DSIs (**Figure 4J,K**).

3.3.3 CV ALONE CANNOT ACCOUNT FOR ALL DIFFERENCES BETWEEN THE STUDIES

None of the inclusion criteria used in the published studies apply a threshold on the CV specifically, but some incorporate measurements of reliability that might have a similar effect. If criteria are selecting neurons based primarily on reliability, one might expect that selecting a population of neurons with matched mean CV would result in similar tuning properties and would replicate the differences observed between the studies. I selected populations of neurons that had the same mean CV as those chosen by each inclusion criteria, for each area separately, and compared the tuning properties for that population to the tuning properties for the neurons chosen by the criteria. For some metrics, there was a high correlation between these values, namely mean preferred TF and mean DSI (r=0.82 Pearsons correlation for both. **Figure 4N, P**). For preferred TF the values were close to unity, indicating that selecting neurons by their CV closely matched the differences between studies. For DSI, however, the range of DSI values was more limited. Thus, while there was a high correlation between the values for neurons selected by CV to those for neurons selected by the criteria, the shallow slope of this relationship made it less predictive. Further, for the mean OSI, the was no correlation between these values (r=0.09, **Figure 4O**). Thus, some of the differences between the published studies could result from the inclusion criteria effectively selecting neurons based on their reliability at different threshold. However, it is clear that the criteria did not select neurons exclusively based on the reliability, as captured by the CV, as CV alone cannot account for all of the differences between the studies.

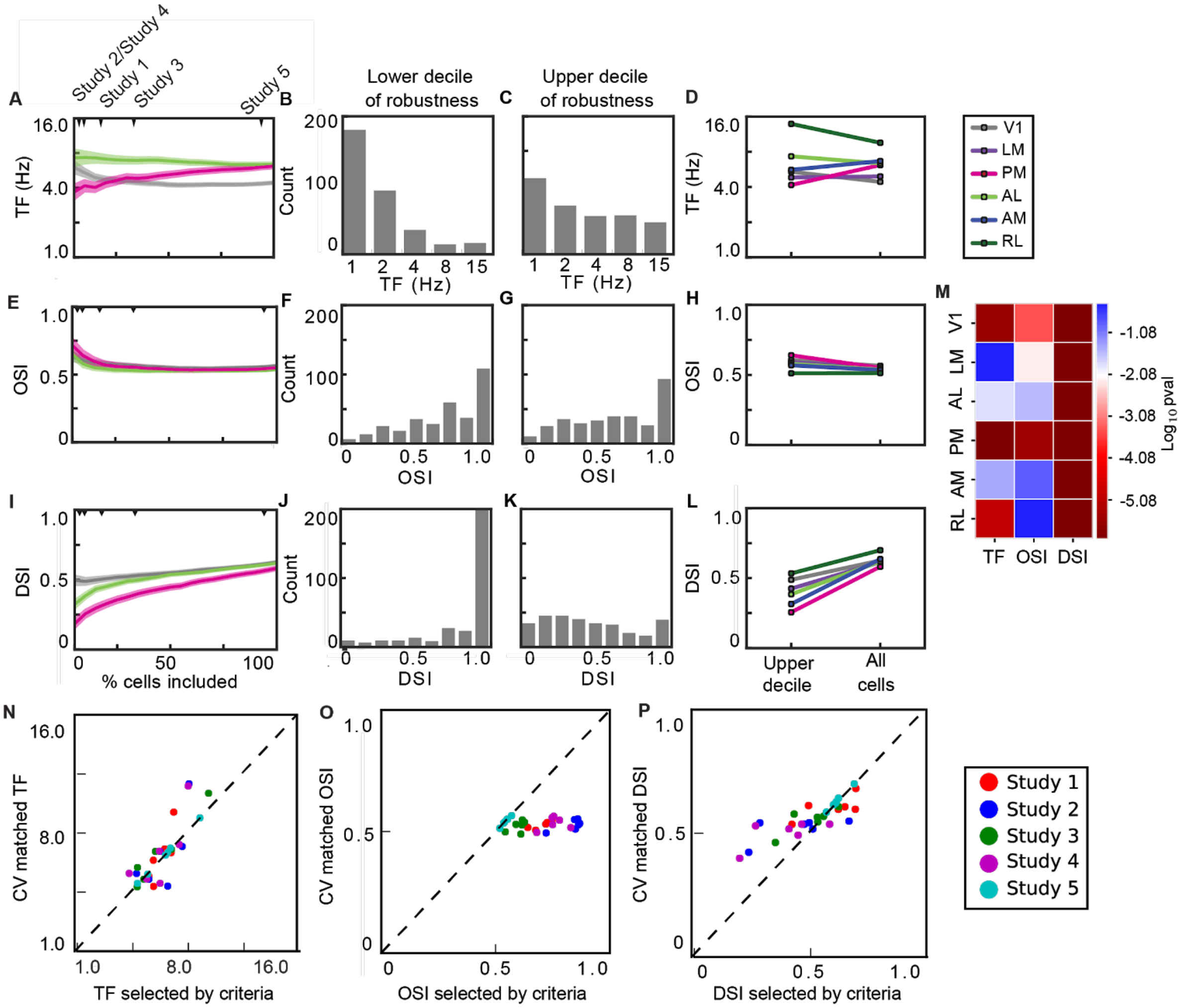

Figure 4. Tuning characteristics of neurons based on robustness. **A, E, I)** Mean TF, OSI, and DSI tuning of neurons in V1, AL, and PM based on what percentage of most robust cells (cells with low coefficient of variation) are included in the analysis. Shaded regions indicate SEM. The minimum percentage most robust cells displayed is 5%. **B)** Distribution of TF tuning of 10% least robust cells. **C)** Distribution of TF tuning of 10% most robust cells. **F, G, J, K)** Same as in **B**, **C** but with OSI and DSI. **D, H, L)** Mean TF, OSI, and DSI tuning of neurons in all visual areas in 10% most robust neurons versus the entire population of neurons. **M)** Heat map displaying p-values for Mann-Whitney U test comparing the 10% most robust neurons and the entire population of neurons. The colorscale is centered at p=0.05/6 to account for Bonferonni correction. **N)** Mean DSI calculated for neurons selected to match the mean CV for each the neurons selected by each criterion, for each area, compared to the mean DSI for the neurons selected by that criteria and area. **O-P)** same as in M but for OSI and TF.

3.3.4 TF and DSI ARE MORE SENSITIVE TO SELECTION BY ROBUSTNESS

Selection by CV displayed a greater effect on preferred TF and DSI than on OSI, likely because the measurements of preferred TF and DSI are more susceptible to noise. The neurons with the noisiest responses (greatest CV) commonly displayed DSI ~1 (**Figure 4J**), which is inevitable when the response to the null direction is 0. The response to the preferred direction need not be large and could even result from a single trial having just a small amplitude fluorescence change. As the preferred TF is the TF at which the neuron has its largest response, regardless of amplitude or reliability, the TF tuning is similarly sensitive to small numbers of noisy events. In contrast, OSI is calculated from the responses to all eight directions of drifting gratings and is thus less sensitive to a small amplitude response in one condition.

3.3.5 CROSS-VALIDATION AND INCREASING NUMBER OF TRIALS DECREASES VARIABILITY

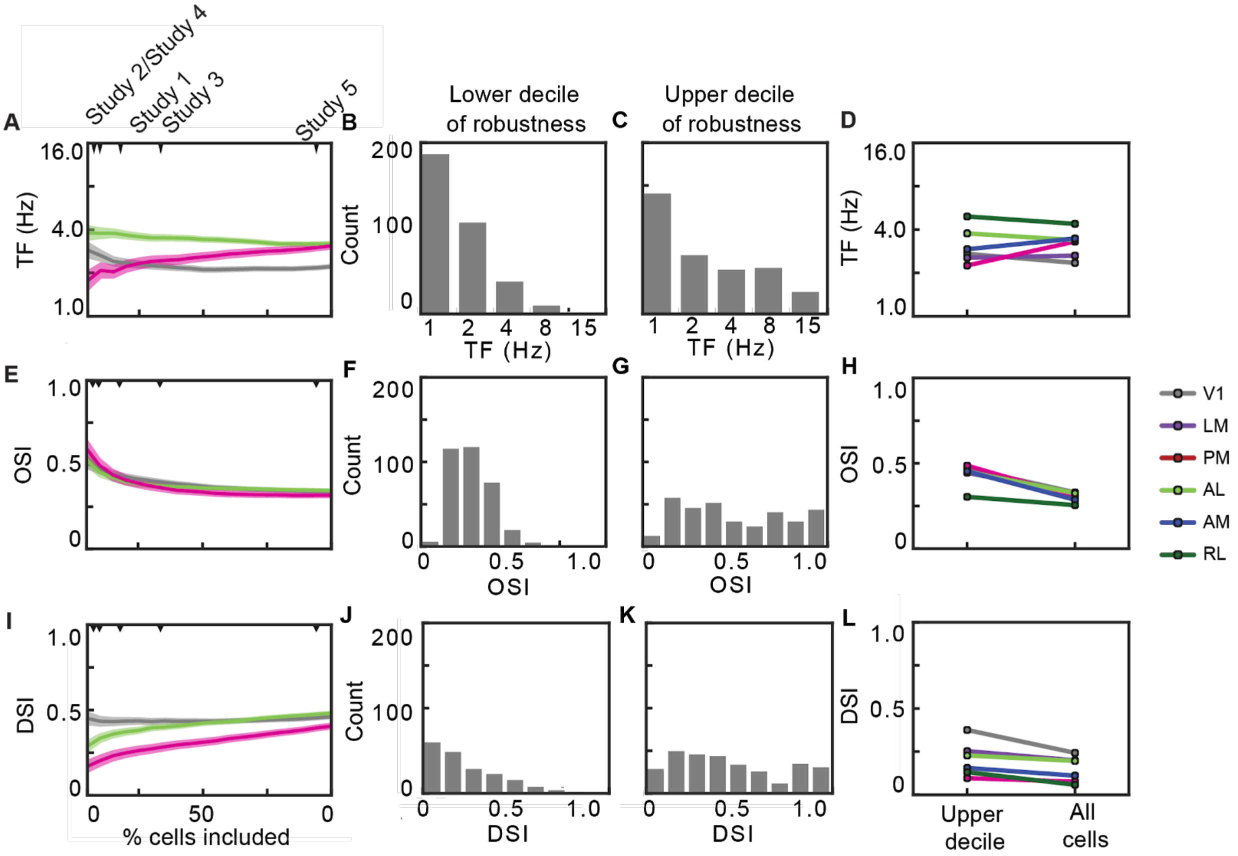

Figure 5. Tuning characteristics of neurons based on robustness with cross-validated metrics. **A, E**, **I**) Mean TF, OSI, and DSI tuning of neurons in V1, AL, and PM based on what percentage of neurons are included in the analysis, starting with the most robust neurons. Shaded regions indicate SEM. The minimum percentage most robust cells displayed is 5%. **B**) Distribution of TF tuning of 10% least robust neurons. **C**) Distribution of TF tuning of 10% most robust neurons. **F, G**, **J**, **K**) Same as in **B**, **C** but with OSI and DSI. **D**, **H**, **L**). Mean TF, OSI, and DSI tuning of neurons in all visual areas in 10% most robust neurons versus the entire population of neurons.

Might a calculation that is more robust to trial-to-trial variability reduce the sensitivity of measurements to inclusion criteria or CV? I.recalculated OSI, DSI and TF with cross-validation, using half of trials to identify the stimulus condition that evoked the largest mean responses (grating direction and temporal frequency) and then calculated OSI, DSI and TF for these preferred conditions from the other half of the trials. The overall effect of including more neurons based on their CV on the cross-validated metrics across different areas was similar to that on the non-cross-validated metrics (**Figure 5**). The notable difference is that the noisy neurons in the lowest decile of robustness no longer have high DSI or OSI values, but are shifted to much lower values (**Figure 5F, J**). This difference is also reflected in the fact that the overall curves are shifted to lower values (compare **Figure 5E, I** with **Figure 4E, I**). Thus, while more statistically robust metrics calculated through cross-validation likely better reflect the true values of the population, they do not reduce the impact of selection on those metrics.

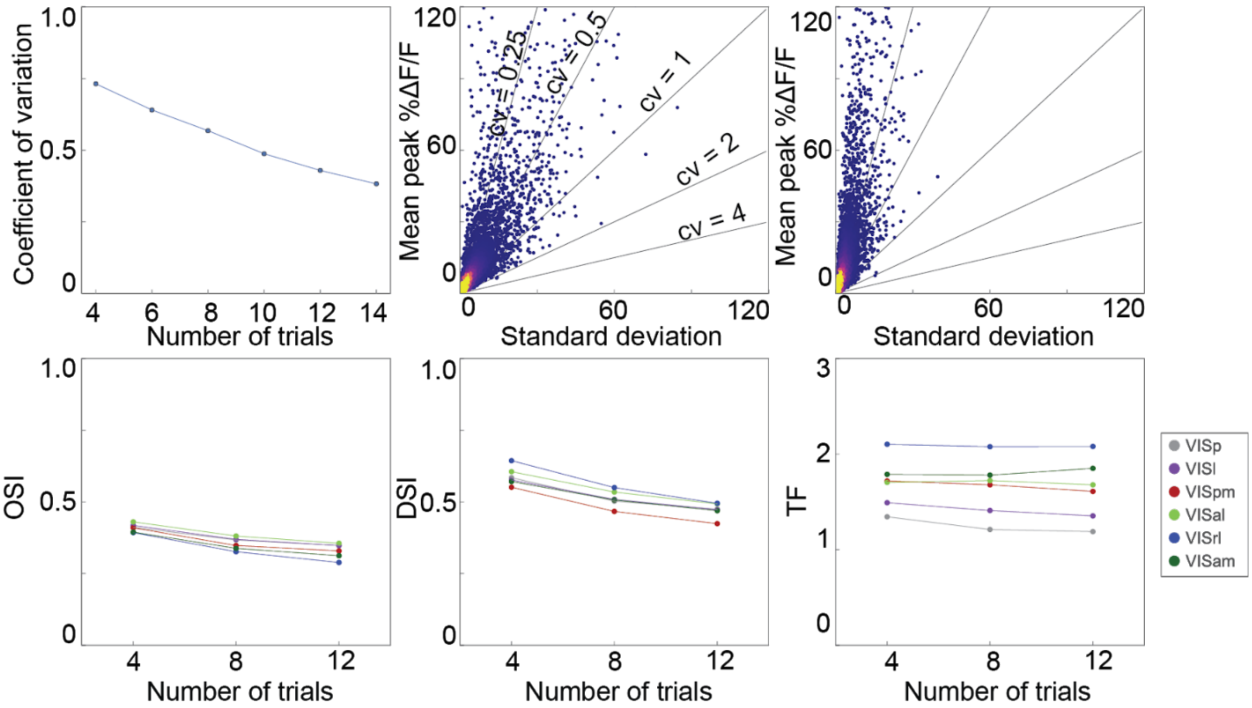

Figure 6. How trial number changes tuning metrics and CV. A) Mean CV calculated at the preferred condition using different numbers of trials and the cross-validation method. **B)** Mean peak response at the preferred condition versus standard deviation at the preferred condition using only four trials and the cross validation method. **C)** same as in B but using 14 trials. **D – F)** OSI, TF, and DSI calculated using the cross validation method as a function of the number of trials used in the analysis.

Different studies presented each visual stimulus multiple times, with numbers of repetitions ranging from 4 to 24 trials (**Table 1**). Might the number of repetitions account for some of the differences between studies? I computed OSI, DSI and preferred TF using subsets of 4-14 trials. As expected, the variability of the responses decreased as the number of trials increased, resulting in a lower mean CV across the entire population (**Figure 6A**). Visualizing the neurons by plotting response mean vs standard deviation for n=4 trials (**Figure 6B**) and n=14 trials (**Figure 6C**), it is clear that the bulk of the data is shifted to more robust responses. Increasing the number of trials had a small effect on the cross-validated metrics (**Figure 6D-F**), decreasing both the mean OSI and DSI across all areas (when including all neurons). The effect was consistent across all areas, however, thus the number of trials did not impact the rank order across areas. Thus, while more trials can reduce the variability of the response measurements, it is unlikely that these differences had a large effect on the differences observed between studies.

3.4 DISCUSSION

I applied different inclusion criteria to the Allen Brain Observatory 2P dataset to examine how these criteria impact the reported tuning properties across visual areas after experimental differences are eliminated. Mean TF, OSI and DSI changed differently with the robustness of the responses of the underlying neurons. The preferred TF was the most sensitive and OSI was the least sensitive.

3.4.1 THIS STUDY CAN HELP US QUANTIFY HOW STRINGENT MY INCLUSION CRITERIA ARE

It is impossible to pick a perfect inclusion criterion. However, these results allow us to put future results in context and ask what percentage of most robust neurons we’re selecting for, therefore giving us an idea of what percentage of the total population of cells we’re including, and how much my results may change were more restrictive.

For my experiments, I chose to use the following metric to determine responsiveness:

Response > 2* std(baseline) for 25% trials

61% of neurons were considered responsive after this criterion was applied. When applied to the brain observatory data, an average of 55% of cells were selected. I can therefore conclude that the inclusion criterion we're using for my analysis is permissive.

Looking at data from only V1, this indicates that the temporal frequency for my analyses will be similar to the TF total population of cells that are segmented (only 1% higher). Compared to the top 10% of cells, however, I expect this value to be 40% lower (4 Hz vs 5.6 Hz).

With this inclusion criterion, I expect that all other visual areas will have a higher average TF than V1.

3.4.2 CROSS-VALIDATION AND INCREASING NUMBER OF TRIALS CAN IMPROVE ACCURACY OF MEASURED RESPONSES

Cross-validating metrics and increasing the number of trials can each improve the accuracy of the measured responses. Cross-validation can mitigate the impact of particularly noisy responses, reducing the impact of small numbers of outlier trials. This is most evident in the effect of cross-validation on the DSI distribution for the neurons in the lowest decile of robustness (**Figure 5J**). It is possible that inclusion criteria based on the reliability of metrics across iterations of cross-validation might be more effective for identifying neurons with truly robust responses

3.4.3 INCLUSION CRITERIA CAN PLAY A ROLE IN DETERMINING TUNING PROPERTIES OF VISUAL AREAS

My results offer one possible explanation as to why published studies produce different results. Therefore, careful consideration of inclusion criteria in designing calcium imaging studies is extremely important. However, other elements of experimental design are likely also important, including the choice of calcium indicator, stimulus parameters, and methods of analysis.

My results illustrate how inclusion criteria can play a role in determining the tuning properties of visual areas. The choice of inclusion criteria is unlikely to account for all of the differences observed between the original studies, indicating that other experimental factors are important. Other factors likely include anesthesia state, the type of anesthesia used, the calcium indicator, image brightness, as well as visual stimulus parameters. Brain state can modulate neural responses in visual cortex, and anesthesia in particular can impact both the spontaneous and evoked responses. The type of anesthesia can also be a factor, with urethane impacting spontaneous and evoked firing rates but not OSI (Niell and Stryker, 2010) and atropine affecting OSI but not spontaneous firing rate, evoked firing rate, DSI, preferred TF, or preferred SF (Durand et al. 2016). Stimulus parameters, such as the size or contrast of the drifting gratings or the precise spatial and temporal frequencies, do also impact the evoked responses and could account for some of the differences observed between the original studies.

Functional specialization of the higher visual areas in mouse cortex has been interpreted as evidence of parallel streams (Andermann et al. 2011; Marshel, Garrett et al. 2011). For example, V1 is thought to transfer low TF, high SF information to PM, the putative gateway to the dorsomedial stream (Glickfeld et al. 2013; Polack and Contreras 2012; Lopez-Aranda et al. 2009). However, in some studies, neurons in V1 and PM have similar mean TF tuning (with PM's being 1.3- 2x that of V1) (Roth, Helmchen, and Kampa 2012; Marshel et al. 2011), while others show that mean TF tuning in PM neurons that is 1/3 that of V1 neurons (Andermann et al. 2011). My results indicate that in the most robust neurons, V1 has a higher TF tuning than PM, but in the least robust neurons, PM has a higher TF tuning than V1, potentially explaining the some of the difference between studies. Since TF is sensitive enough to inclusion criteria to change the relative order of TF tuning, it is difficult to interpret the relative TF tuning between visual areas currently. The most appropriate inclusion criteria would take into account how downstream targets filter or weight inputs and how robustness factors into that weighting. Since it is not known what this weighting is, I must be cautious in drawing conclusions about functional organization from these analyses.

4. CONCLUSIONS AND FUTURE DIRECTIONS

In this thesis, my goal was to characterize how basic tuning properties are mapped in visual cortex. In **CHAPTER 1**, I summarized how different functional properties are mapped in the retina, thalamus, and visual cortex. In **CHAPTER 2**, I used a combination of widefield calcium imaging and 2P calcium imaging to measure how spatial frequency (SF) and temporal frequency (TF) tuning properties are mapped in V1 and higher visual areas of mouse visual cortex. In **CHAPTER 3**, I leveraged a large standardized dataset to study how inclusion criteria can affect tuning properties, particularly temporal frequency, directional selectivity, and orientation selectivity. My analyses and conclusions in **CHAPTER 3** influence how I interpret results in **CHAPTER 2**, previous analyses measuring tuning properties in mouse visual areas, and future studies.

4.1.1 THE IMPORTANCE OF CHOOSING APPROPRIATE INCLUSION CRITERIA

In **CHAPTER 3,** I found that applying different inclusion criteria to a single population of cells changes the resulting TF tuning, orientation selectivity index (OSI), and directional selectivity index (DSI). Since previous studies use different inclusion criteria, my results offer one possible explanation why published studies comparing TF, OSI and DSI across mouse visual areas have produced different results for TF and more similar results for OSI and DSI. Mean TF tuning is more sensitive than OSI and DSI to the neurons selected. As a result, comparison across studies is difficult and there remains considerable uncertainty regarding the mean TF and the rank order of TF tuning across mouse visual areas.

My results illustrate how inclusion criteria can play a role in determining the tuning properties of visual areas. This may be true in other species besides mice, particularly as calcium imaging is becoming a more tractable technique in primates and other species. While experimental factors are important, the choice of inclusion criteria is critical for proper interpretation of results. My study provides evidence for the importance of a sensitivity analysis: a method to determine how sensitive a particular metric is to the robustness of the subpopulation of neurons that is included in the analysis from a larger population in a calcium imaging dataset. Quantifying how choosing only the most robust cells changes the apparent TF, OSI, and DSI tunings in different populations of neurons is critical for interpreting results. Similar sensitivity analyses are important in other studies that measure tuning metrics, especially TF, OSI, and DSI.

What population of neurons is encoding relevant information about the visual stimulus? In any given cellular population, there is considerable variability in how strongly and consistently neurons respond to their preferred visual stimulus. However, some weakly responsive neurons are still clearly tuned (see **CHAPTER 3, Figure 2**). My study highlights that the most robust neurons in a dataset and the least robust neurons in a dataset have different TF, OSI, and DSI tunings. Which neurons are encoding relevant information about stimulus features? A related question is: are only the most responsive and reliable neurons determining the output of a given area? To answer this question, one might look at the axonal tuning of the outputs of a visual area and the tuning of the target area and ask how they compare to the tuning of the population from the original visual area, particularly the tuning of the most and least robust cells of the population. Further study is necessary to understand how strongly and weakly responsive neurons in a population contribute differently to cortical computations.

4.1.2 ASYMMETRICAL PROCESSING OF STIMULUS FEATURES

In the mouse, there is growing evidence that stimulus features are processed asymmetrically across the visual field. I show that both spatial frequency (SF) and TF are processed asymmetrically across the visual field. Most appreciably, there is a marked difference in the TF tuning in V1 based on altitude. In mice, previous studies and my results suggest that SF, temporal frequency, and coherent motion stimuli are processed differently based on retinotopic location. Indeed, recent studies measuring coherent motion processing (Sit & Goard, 2020) also support this conclusion. While Sit & Goard postulated an “lower field advantage” due to the stronger coherent motion tuning in the lower visual field, I propose an “upper visual advantage”, due to the higher TF and SF tuning of cells in the upper visual field.

One might expect that visual regions that process coherent motion might have specialized TF tuning. Indeed, there are some similarities between the TF tuning maps in my study and the coherent motion maps in Sit and Goard (2020). Sit and Goard (2020) found that neurons with receptive fields in the lower part of the visual field had stronger responses to coherent motion than those with receptive fields in the upper part of the visual field. Within the context of my results, this would suggest that in V1, neurons in the upper part of the visual field have higher TF tuning but weaker responses to coherent motion. This suggests that the high TF tuning of the lower part of V1 might be used for a different computation. Neurons that are specialized to detect coherent motion might be better-suited to detecting self-motion signals. Areas PM and AM both have strong responses to coherent motion and are biased to upper temporal portions of the visual field and receive feedback projections from motor areas (**Figure 1**).

It is possible that the coherent motion tuning is actually a feedback effect rather than a feedforward one, as V1 integrates spatial context signals. Based on my widefield thalamic results, the differences in SF and TF tuning across the visual field are likely inherited from thalamic inputs therefore feedforward in nature. Further research is necessary to determine whether parallel processing of TF tuning and coherent motion as well as other properties is present in other species and other sensory cortices, including in humans and non-human primates, and whether this upper field advantage exists in other species.

4.1.3 PARALLEL STREAMS AND HIERARCHY IN MICE

What sorts of parallels can be drawn between mice and primates? There is substantial evidence that the mouse visual cortex is organized hierarchically and that higher visual areas are functionally specialized (Harris et al., 2019; Siegel et al., 2021). A growing body of evidence shows that different visual areas have different roles in visual perception in mice. The current literature suggests that visual areas that project to limbic cortices appear to be involved in object identification, while visual areas that project to motor and motor-associated cortices appear to be involved in the detection of global motion signals.

However, it is unclear that any specific areas in the mouse can be matched to higher visual areas in primates. Thus far, researchers have failed to find the characteristic receptive field properties reminiscent of the types of hierarchical computations that are hallmarks of primate vision. This section places my findings in the context of previous findings about the parallel and hierarchical structure in primate and mouse visual systems.

In primates, the two visual streams hypothesis suggests processing of visual information into two distinct routes in the brain: a dorsal stream for the control of actions and a ventral stream for the identification of objects (Kravitz et al. 2011, 2013; Milner & Goodale 2008, Nassi & Callaway 2009, Ungerleider & Mishkin 1982). Decades of primate research have come to challenge this dichotomy, and suggest that the two may be interconnected (the dorsal stream is, for example, also involved in spatial attention and novel object recognition). Still, ventral stream areas have distinctive receptive field properties and encode feature, shape, and objects. These features are distinct from the receptive field properties of dorsal stream areas: neurons in these areas encode direction, pattern motion, and coherent motion tuning.

In the mouse, there is some evidence for parallel processing of visual information based on connectivity analyses. Downstream targets of HVAs are divided into two separate submodules: one module that has been analogized to the ventral stream, which includes temporal association areas and the entorhinal cortex, and another that has been analogized to the dorsal stream, which provides output to retrosplenial, anterior cingulate, and secondary motor cortices (Wang et al., 2012; Oh et al., 2014).

In addition, the unique receptive field properties of higher visual areas relative to V1 provide evidence for parallel and hierarchical processing of mouse visual areas. A prerequisite for functional specialization of higher visual areas in both the dorsal and ventral streams is an increase in receptive field size: neurons integrate information over a larger field of view, underpinning their ability to generalize and complex features and objects, speed, and complex motion. In the mouse, receptive field sizes increase in higher visual areas (Van den Bergh, 2010; Wang & Burkhalter, 2007).

The larger receptive field properties and the unique SF and TF tuning of mouse higher visual areas are certainly evidence for functional specialization of higher visual areas (see **CHAPTER 1**). Connectivity analysis and electrophysiology have confirmed the presence of a hierarchy that begins with V1, then LM, RL, AL, P, and finally PM and AM at the top. However, previous studies, particularly those using simple grating stimuli have failed to find evidence for the hierarchical transformations that are hallmarks of primate vision in mice.

For example, in mice, there is currently no evidence for the presence of shape or object-specific receptive fields like those found in ventral stream areas in the primate. Comparable experiments have not yet been performed in the mouse, but some have been performed in other rodents. In rats, while feature or object-selective receptive fields have not been found directly, neurons in the putative ventral stream could discriminate natural from scrambled movies (Vermaercke et al. 2014, Vinken et al. 2017). Putative ventral stream regions may play a role in object identification rather than object encoding, however. Although the higher-area neurons were worse at discriminating between abstract shapes than those in V1, their selectivity better matched the behavior of the rat (Vermaercke et al. 2015).

A classic example of a hierarchical transformation found in the primate visual system is the formation of pattern-motion selective receptive fields in MT. While pattern-selective receptive fields have been found in mice (Juavinett & Callaway, 2015), they are found in small proportions in various higher visual areas. Pattern motion is therefore not restricted to a visual area.

Based on my widefield results, I found that mouse visual cortical areas could not be separated into two different functionally distinct classes based on the TF and SF or speed tuning properties. As previous studies have noted (Andermann et al., 2011, Marshel et al., 2011), one might predict that object encoding areas preserve SF tuning along the cortical hierarchy, while areas involved in motion-detection stream-like computations prefer high TF stimuli. While there were clear differences in the SF and TF tuning properties between areas, and TF and SF tunings correlated (where areas with higher TF tended to have lower SF and vice versa), I found some clear deviations from the expected TF and SF tunings. First, all higher visual areas had high TF tuning. While putative object-related areas LM and LI had high SF tuning, LI also had high TF tuning. Area PM, a putative motion-related area, had high SF tuning.

It is possible that areas process SF and TF (Jin and Glickfeld, 2019) and other relevant stimulus features similarly, but downstream decoders process these stimulus features differently. Such is the case with orientation tuning, for example. This suggests that multiple visual areas could have similar tuning but process different properties overall.

It is unlikely visual information routes like the ventral and dorsal streams exist in mice. However, mice do exhibit a number of visual behaviors, including distinguishing signals from noise and prey-capture, so it is very possible that higher visual areas are functionally specialized to allow for mice to perform these behaviors. Little is known about the functional specializations that do occur in higher visual areas and further study is needed.

Biases in retinotopic representations can also be used to draw comparisons between species: The bias of PM and AM for temporal retinotopic coordinates matches that of dorsal stream areas MT, MST, and DM (Garrett et al. 2014, Huk et al. 2002, Maunsell & Van Essen 1987, Zhuang et al. 2017). Efforts to characterize hierarchical transformations as patterned motion (Juavinett & Callaway, 2015), shape selectivity (Vermaercke et al. 2014, Vinken et al. 2016), and color (Rhim et al. 2017) have revealed that specific mouse higher visual areas do not encode these features, although color is encoded asymmetrically across the visual field.

Biases in retinotopic representation may be important for determining what role areas play in visual computation during navigation, as is discussed in detail in the next section.

4.1.4 THE ROLE OF NAVIGATION IN MOUSE VISION

A piece that might be critical to understanding the role of higher visual areas in mouse vision is their role in navigation and spatial processing. The mouse visual system appears to be modulated strongly by locomotion, head movements, spatial signals, and distance travelled, suggesting that V1 is a place for integration of navigation and visual signals (Flossman & Rochefort, 2021). Other Spatial modulation seems to be a purely cortical phenomenon, since it isn’t present in thalamic circuits (Diamanti et al., 2021).

Indeed, another hypothesis that has been presented recently is that there are different streams of visual processing for the purpose of navigation in the mouse, based on the retinotopic biases of visual areas. This hypothesis states that higher visual areas that are biased to the center of the visual field are specialized to process landmarks, while those biased for the periphery are specialized to process self-motion related signals (**Figure 1**). This would place areas LM, LI, AL, and RL along the central streams and PM, P, and AM along the peripheral streams. Within the context of this hypothesis, I might expect two outcomes from my results: one, that the upper temporal portion of V1 might be specialized to process high SF, low TF stimuli and that two, that visual areas are biased for the periphery of the visual field have higher TF tuning than those biased for the center.

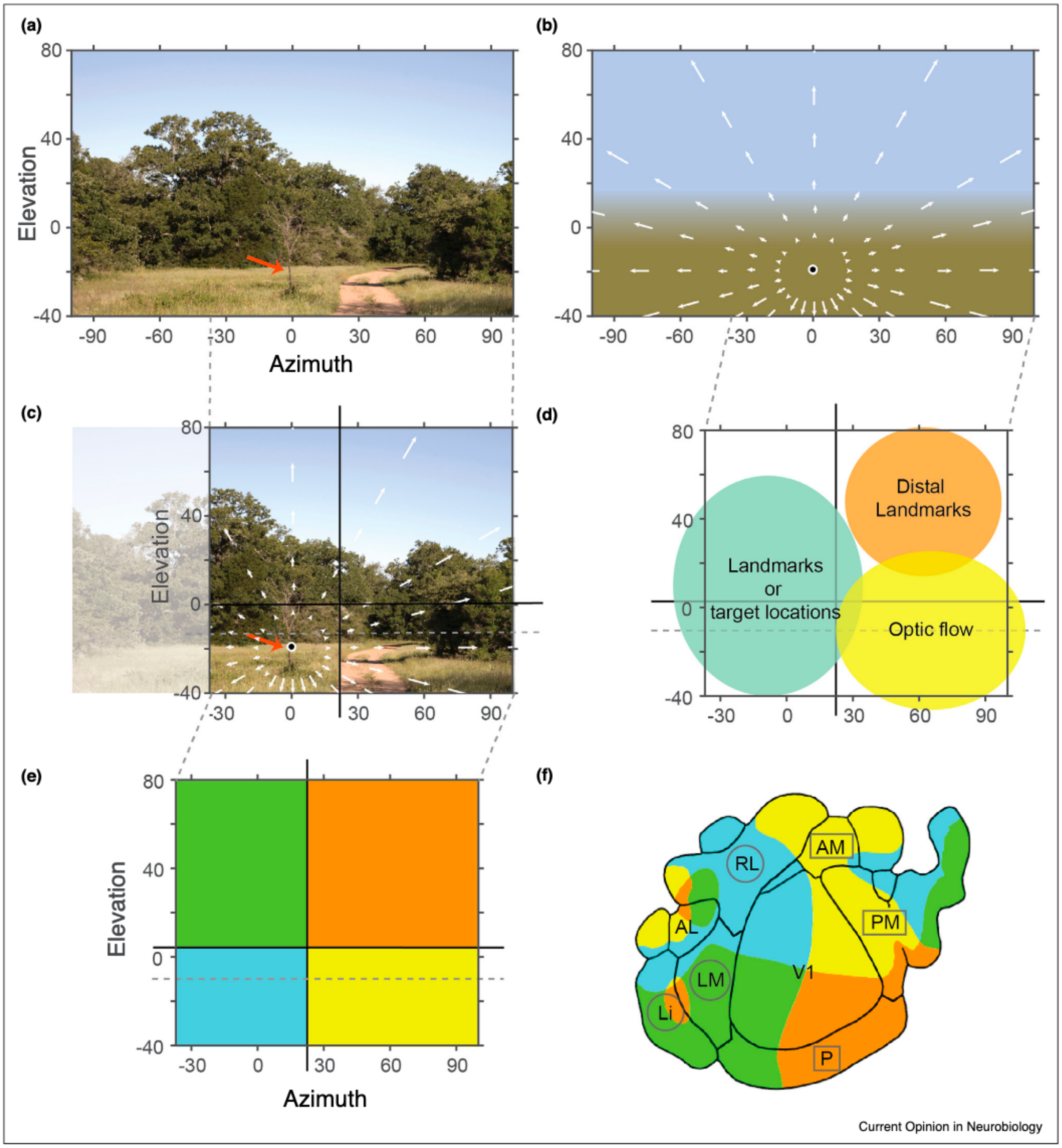

Figure 1. From Saleem et al., 2020. **A**) Example natural scene. The red arrow points to a potential target/landmark location **B**) Schematic of the optic flow pattern expected for forward translation towards a central target/landmark **C**) The overlay of the optic flow vectors on the sample natural image. **D)** Hypothesized distribution of the visual information at different positions in the visual field (while the chosen natural scene in **A**,**C**) has no features in the region highlighted 'Distal Landmarks', one can expect distant features in landscapes, such as hills, in this region) **E**,**F**). Visual field representation across higher visual areas. Modified from Zhuang et al., 2019. Areas hypothesised to be on a central pathway are circled, while those on the peripheral pathway are in a rectangular box.

My results support the first outcome with respect to TF. While the difference between the nasal and temporal TF tuning of V1 in altitude was not as pronounced, I still saw higher TF tuning in the upper and temporal portions of the visual field. In addition, it seems that all visual areas contain gradients of TF, which supports the idea that some portions of visual areas might be specialized for encoding optic flow or self-motion.

The second outcome was not readily supported by my TF analysis but there are some indications that the functional properties of higher visual areas might, for some areas, be related to their visual field bias. While I also found gradients of SF and TF tuning in higher visual areas similar to those in V1, indicating that certain parts of higher visual areas might indeed be tuned to process optic flow or other computations that require underlying neuronal populations to have high TF tuning properties, only some areas correlate with putative central stream and peripheral stream areas. While putative central stream areas LI and LM do indeed have higher SF tuning than most other visual areas, which is consistent with this hypothesis, the central steam also includes RL and AL, which have the high TF and low SF tuning. However, area RL might be specialized to process binocular signals, particularly optical disparity, and seems to be driven weakly by drifting grating stimuli. AM and PM both have similar and relatively high TF and SF tuning properties, which does not readily support this hypothesis.

It is possible that feature-detection in higher visual areas is performed primarily by V1 and areas LM and LI, which have the highest SF tuning of most higher visual areas. There has been previous preliminary evidence that the upper nasal portion of the visual field is a fovea-like region (Bleckert et al., 2014; Paik & Ringach, 2011), supporting my results that the upper portion of the visual field has high SF tuning. This might indicate that feature, landmark, or target locations may instead be processed by the upper nasal visual field, while RL and AL, and the lower visual field have other functions.

However, it is possible that gratings are not the ideal stimuli for interrogating whether these areas are specialized for detecting targets, and the functions of higher visual areas might best be interrogated in freely navigating mice rather than the head-restrained preparation I used. Another alternative is that all TF tuning bands are required for processing of self-motion signals, to make computations that distinguish between moving external stimuli and self-motion. In addition, different visual areas could be specifically tuned to distinguishing these slow- and fast-moving signals.

4.1.5 FINDING THE PUTATIVE CIRCUIT FOR FUNCTIONAL SPECIALIZATION ACROSS THE VISUAL FIELD IN RESPONSE TO DRIFTING GRATINGS

TF and SF are basic tuning properties. While they are informative to draw putative conclusions about the potential functions of cortical areas, drifting gratings are likely not sufficient to fully characterize the functions of mouse visual cortical neurons, the hierarchy of mouse visual cortex, or the extent of functional specialization of the visual field.

However, there are differences in the functional specialization across the visual field, and that different circuits containing different cell types may govern visual processing in different parts of the visual field.

Cells in different parts of the visual field may respond better to more naturalistic stimuli, which may alter SF and TF tuning maps. In the retina, spatiotemporal coding changes in response to more natural images — tuning bandwidth decreases when more spatiotemporal frequency bands are introduced into these stimuli (Ravello et al., 2018). Cells in RL are also driven more strongly due to naturalistic stimuli. Using more naturalistic stimuli may thus reveal even starker differences in the tuning properties across the visual field.

Full-field gratings have been shown to suppress responses, which might also change response properties unequally in visual areas across visual cortex, especially in areas that integrate over large areas of visual space such as PM (Murgas et al, 2020; Adesnik et al., 2012; Vaceilunate et al., 2012).

There is asymmetric expression of RGC populations (Bleckert et al., 2014; El-Danaf et al., 2019) and cone photoreceptors across the retina (Rhim et al., 2017), and future studies might focus on which RGC populations or neuronal populations might be involved in generating the functional specialization in cortex in response to drifting gratings.

5. BIBLIOGRAPHY

1. Abramson, B. P., & Chalupa, L. M. (1988). Multiple pathways from the superior colliculus to the extrageniculate visual thalamus of the cat. *Journal of Comparative Neurology*, *271*(3), 397-418.
2. Adams, D. L., & Horton, J. C. (2003). A precise retinotopic map of primate striate cortex generated from the representation of angioscotomas. *Journal of Neuroscience*, *23*(9), 3771-3789.
3. Adelson, E. H., & Bergen, J. R. (1985). Spatiotemporal energy models for the perception of motion. *Josa a*, *2*(2), 284-299.
4. Adesnik, H., Bruns, W., Taniguchi, H., Huang, Z. J., & Scanziani, M. (2012) .*Nature*, *490*(7419), 226-231.
5. Ahmadlou, M., Zweifel, L. S., & Heimel, J. A. (2018). Functional modulation of primary visual cortex by the superior colliculus in the mouse. *Nature communications*, *9*(1), 1-13.
6. Albright, T. D. (1984). Direction and orientation selectivity of neurons in visual area MT of the macaque. *Journal of neurophysiology*, *52*(6), 1106-1130.
7. Andermann, M. L., Kerlin, A. M., Roumis, D. K., Glickfeld, L. L. & Reid, C. R. (2011). Functional Specialization of Mouse Higher Visual Cortical Areas. *Neuron* 72, 1025–1039
8. Bard, P. (1938). Studies on the Cortical Representation of Somatic Sensibility: Harvey Lecture, February 17, 1938. *Bulletin of the New York Academy of Medicine*, *14*(10), 585.
9. Beltran, W. A., Cideciyan, A. V., Guziewicz, K. E., Iwabe, S., Swider, M., Scott, E. M., ... & Aguirre, G. D. (2014) Canine retina has a primate fovea-like bouquet of cone photoreceptors which is affected by inherited macular degenerations. *PloS one*, *9*(3), e90390.
10. Bleckert, A., Schwartz, G. W., Turner, M. H., Rieke, F., & Wong, R. O. (2014). Visual space is represented by nonmatching topographies of distinct mouse retinal ganglion cell types. *Current Biology*, *24*(3), 310-315.
11. Bhaumik, B., & Shah, N. P. (2014). Development and matching of binocular orientation preference in mouse V1. *Frontiers in systems neuroscience*, *8*, 128.
12. Bonhoeffer, T., & Grinvald, A. (1991). Iso-orientation domains in cat visual cortex are arranged in pinwheel-like patterns. *Nature*, *353*(6343), 429-431.
13. Born, R. T., & Tootell, R. B. (1991). Single-unit and 2-deoxyglucose studies of side inhibition in macaque striate cortex. *Proceedings of the National Academy of Sciences*, *88*(16), 7071-7075.
14. Born, R. T., & Bradley, D. C. (2005). Structure and function of visual area MT. *Annu. Rev. Neurosci.*, *28*, 157-189.
15. Braddick, O. J., O'Brien, J. M., Wattam-Bell, J., Atkinson, J., Hartley, T., & Turner, R. (2001). Brain areas sensitive to coherent visual motion. *Perception*, *30*(1), 61-72.
16. Braida, D., Donzelli, A., Martucci, R., Ponzoni, L., Pauletti, A., Langus, A., & Sala, M. (2013). Mice discriminate between stationary and moving 2D shapes: application to the object recognition task to increase attention. *Behavioural brain research*, *242*, 95-101.
17. Burgess, C. R., Ramesh, R. N., Sugden, A. U., Levandowski, K. M., Minnig, M. A., Fenselau, H., ... & Andermann, M. L. (2016). Hunger-dependent enhancement of food cue responses in mouse postrhinal cortex and lateral amygdala. *Neuron*, *91*(5), 1154-1169.
18. Canário, N., Jorge, L., Silva, M. L., Soares, M. A., & Castelo-Branco, M. (2016). Distinct preference for spatial frequency content in ventral stream regions underlying the recognition of scenes, faces, bodies and other objects. *Neuropsychologia*, *87*, 110-119.
19. Caviness Jr, V. S. (1975). Architectonic map of neocortex of the normal mouse. *Journal of Comparative Neurology*, *164*(2), 247-263.

20. Chaplin, T. A., Yu, H. & Rosa, M. G. P. (2013). Representation of the visual field in the primary visual area of the marmoset monkey: Magnification factors, point-image size, and proportionality to retinal ganglion cell density. *J Comp Neurol* 521, 1001–1019.
21. Chen, G., Lu, H. D. & Roe, A. W. (2008). A Map for Horizontal Disparity in Monkey V2. *Neuron* 58, 442–450.
22. Chen, T.-W. *et al.* (2013). Ultrasensitive fluorescent proteins for imaging neuronal activity. *Nature*, *499*, 295.
23. Czuba, T. B., Rokers, B., Huk, A. C. & Cormack, L. K. (2010). Speed and Eccentricity Tuning Reveal a Central Role for the Velocity-Based Cue to 3D Visual Motion. *Journal of Neurophysiology* **104**, 2886–2899.
24. Dacey, D. M. (2004). Origins of perception: retinal ganglion cell diversity and the creation of parallel visual pathways. *The cognitive neurosciences*, *3*, 281-301.
25. Dacey, D. M., Peterson, B. B., Robinson, F. R., & Gamlin, P. D. (2003). Fireworks in the primate retina: in vitro photodynamics reveals diverse LGN-projecting ganglion cell types. *Neuron*, *37*(1), 15-27.
26. Dacey, D. M., & Petersen, M. R. (1992). Dendritic field size and morphology of midget and parasol ganglion cells of the human retina. *Proceedings of the National Academy of sciences*, *89*(20), 9666-9670.
27. Daniel, P. M., & Whitteridge, D. (1961). The representation of the visual field on the cerebral cortex in monkeys. *The Journal of Physiology, 159,* 203–221.
28. de Vries, S. E., Lecoq, J. A., Buice, M. A., Groblewski, P. A., Ocker, G. K., Oliver, M., ... & Koch, C. (2020). A large-scale standardized physiological survey reveals functional organization of the mouse visual cortex. *Nature neuroscience*, *23*(1), 138-151.
29. Desimone, R. & Gross, C. G. (1979). Visual areas in the temporal cortex of the macaque. *Brain Res, 178*, 363–380
30. Diamanti, E. M., Reddy, C. B., Schröder, S., Muzzu, T., Harris, K. D., Saleem, A. B., & Carandini, M. (2021). Spatial modulation of visual responses arises in cortex with active navigation. *Elife*, *10*, e63705.
31. Douglas, R. M., Neve, A., Quittenbaum, J. P., Alam, N. M., & Prusky, G. T. (2006). Perception of visual motion coherence by rats and mice. *Vision research*, *46*(18), 2842-2847.
32. Durand, S., Iyer, R., Mizuseki, K., de Vries, S., Mihalas, S., & Reid, R. C. (2016). A comparison of visual response properties in the lateral geniculate nucleus and primary visual cortex of awake and anesthetized mice. *Journal of Neuroscience*, *36*(48), 12144-12156.
33. Drager, U. C., & Hubel, D. H. (1975). Responses to visual stimulation and relationship between visual, auditory, and somatosensory inputs in mouse superior colliculus. *Journal of Neurophysiology*, *38*(3), 690-713.
34. Eiber, C. D., Rahman, A. S., Pietersen, A. N., Zeater, N., Dreher, B., Solomon, S. G., & Martin, P. R. (2018). Receptive field properties of koniocellular on/off neurons in the lateral geniculate nucleus of marmoset monkeys. *Journal of Neuroscience*, *38*(48), 10384-10398.
35. El-Danaf, R. N., & Huberman, A. D. (2019). Sub-topographic maps for regionally enhanced analysis of visual space in the mouse retina. *Journal of Comparative Neurology*, *527*(1), 259-269.
36. Essen, D. C. V. (1997). A tension-based theory of morphogenesis and compact wiring in the central nervous system. *Nature, 385*, 313–318.
37. Everson, R. M., Prashanth, A. K., Gabbay, M., Knight, B. W., Sirovich, L., & Kaplan, E. (1998). Representation of spatial frequency and orientation in the visual cortex. *Proceedings of the National Academy of Sciences*, *95*(14), 8334-8338.

38. Felleman, D. J., Burkhalter, A., & Van Essen, D. C. (1997). Cortical connections of areas V3 and VP of macaque monkey extrastriate visual cortex. *Journal of Comparative Neurology*, *379*(1), 21-47.
39. Felleman, D. J., & Van Essen, D. C. (1991). Distributed hierarchical processing in the primate cerebral cortex. *Cerebral cortex (New York, NY: 1991)*, *1*(1), 1-47.
40. Ferrera, V. P., Rudolph, K. K., & Maunsell, J. H. (1994). Responses of neurons in the parietal and temporal visual pathways during a motion task. *Journal of Neuroscience*, *14*(10), 6171-6186.
41. Flossmann, T., & Rochefort, N. L. (2021). Spatial navigation signals in rodent visual cortex. *Current Opinion in Neurobiology*, *67*, 163-173.
42. Foster, K. H., Gaska, J. P., Nagler, M., & Pollen, D. A. (1985). Spatial and temporal frequency selectivity of neurones in visual cortical areas V1 and V2 of the macaque monkey. *The Journal of physiology*, *365*(1), 331-363.
43. Garg, A. K., Li, P., Rashid, M. S., & Callaway, E. M. (2019). Color and orientation are jointly coded and spatially organized in primate primary visual cortex. *Science*, *364*(6447), 1275-1279.
44. Garrett, M. E., Nauhaus, I., Marshel, J. H. & Callaway, E. M. (2014).Topography and Areal Organization of Mouse Visual Cortex. *The Journal of Neuroscience, 34*, 12587–12600
45. Girman, S. V., Sauvé, Y., & Lund, R. D. (1999). Receptive field properties of single neurons in rat primary visual cortex. *Journal of neurophysiology*, *82*(1), 301-311.
46. Glickfeld, L. L., Andermann, M. L., Bonin, V. & Reid, C. R. (2013).Cortico-cortical projections in mouse visual cortex are functionally target specific. *Nature Neuroscience 16*, nn.3300
47. Glickfeld, L. L., Histed, M. H., & Maunsell, J. H. (2013). Mouse primary visual cortex is used to detect both orientation and contrast changes. *Journal of Neuroscience*, *33*(50), 19416-19422.
48. Glickfeld, L. L., Reid, C. R. & Andermann, M. L. (2014).A mouse model of higher visual cortical function. *Current Opinion in Neurobiology*, *24*, 28–33
49. Goldey, G. J., Roumis, D. K., Glickfeld, L. L., Kerlin, A. M., Reid, R. C., Bonin, V., ... & Andermann, M. L. (2014). Removable cranial windows for long-term imaging in awake mice. *Nature protocols*, *9*(11), 2515.
50. Goodale, M. A. (2014). How (and why) the visual control of action differs from visual perception. *Proceedings of the Royal Society B: Biological Sciences, 281*, 20140337
51. Goodale, M. A., & Humphrey, G. K. (1998). The objects of action and perception. *Cognition*, *67*(1-2), 181-207.
52. Goodale, M. A. & Milner, A. D. (1992). Separate visual pathways for perception and action. *Trends in Neurosciences, 15*, 20–25
53. Goltstein, P. M., Montijn, J. S., & Pennartz, C. M. (2015). Effects of isoflurane anesthesia on ensemble patterns of Ca 2+ activity in mouse v1: reduced direction selectivity independent of increased correlations in cellular activity. *PloS one*, *10*(2), e0118277.
54. Grubb, M. S. & Thompson, I. D. (2003). Quantitative Characterization of Visual Response Properties in the Mouse Dorsal Lateral Geniculate Nucleus. *Journal of Neurophysiology, 90*, 3594–3607
55. Habot-Wilner, Z., Noronha, G., & Wykoff, C. C. (2019). Suprachoroidally injected pharmacological agents for the treatment of chorio-retinal diseases: a targeted approach. *Acta ophthalmologica*, *97*(5), 460-472.
56. Harris, J. A., Mihalas, S., Hirokawa, K. E., Whitesell, J. D., Choi, H., Bernard, A., ... & Zeng, H. (2019). Hierarchical organization of cortical and thalamic connectivity. *Nature*, *575*(7781), 195-202.

57. Hawken, M. J., Parker, A., & Lund, J. S. (1988). Laminar organization and contrast sensitivity of direction-selective cells in the striate cortex of the Old World monkey. *Journal of Neuroscience*, *8*(10), 3541-3548.
58. Hendel, T., Mank, M., Schnell, B., Griesbeck, O., Borst, A., & Reiff, D. F. (2008). Fluorescence changes of genetic calcium indicators and OGB-1 correlated with neural activity and calcium in vivo and in vitro. *Journal of Neuroscience*, *28*(29), 7399-7411.
59. Henschen, S. (1890): Klinische und anatomische Beiträge zur Pathologie des Gehirns. Stockholm (Vol 1). Almquist and Wiksell.
60. Horton, J. C. (1984). Cytochrome oxidase patches: a new cytoarchitectonic feature of monkey visual cortex. *Philosophical Transactions of the Royal Society of London. B, Biological Sciences*, *304*(1119), 199-253.
61. Horton, J. C., & Hocking, D. R. (1996). An adult-like pattern of ocular dominance columns in striate cortex of newborn monkeys prior to visual experience. *Journal of Neuroscience*, *16*(5), 1791-1807.
62. Howarth, M., Walmsley, L., & Brown, T. M. (2014). Binocular integration in the mouse lateral geniculate nuclei. *Current Biology*, *24*(11), 1241-1247.
63. Hoy, J. L., Yavorska, I., Wehr, M. & Niell, C. M. (2016). Vision Drives Accurate Approach Behavior during Prey Capture in Laboratory Mice. *Curr Biol, 26*, 3046–3052
64. Huang, L., Ledochowitsch, P., Knoblich, U., Lecoq, J., Murphy, G. J., Reid, R. C., ... & Li, L. (2021). Relationship between simultaneously recorded spiking activity and fluorescence signal in GCaMP6 transgenic mice. *Elife*, *10*, e51675.
65. Hübener, M., Shoham, D., Grinvald, A., & Bonhoeffer, T. (1997). Spatial relationships among three columnar systems in cat area 17. *Journal of Neuroscience*, *17*(23), 9270-9284.
66. Huk, A. C., Dougherty, R. F., & Heeger, D. J. (2002). Retinotopy and functional subdivision of human areas MT and MST. *Journal of Neuroscience*, *22*(16), 7195-7205.
67. Huk, A. C., & Heeger, D. J. (2002). Pattern-motion responses in human visual cortex. *Nature neuroscience*, *5*(1), 72-75.
68. Juavinett, A. L., & Callaway, E. M. (2015). Pattern and component motion responses in mouse visual cortical areas. *Current Biology*, *25*(13), 1759-1764.
69. Juavinett, A. L., Kim, E. J., Collins, H. C., & Callaway, E. M. (2020). A systematic topographical relationship between mouse lateral posterior thalamic neurons and their visual cortical projection targets. *Journal of Comparative Neurology*, *528*(1), 99-111.
70. Jin, M., & Glickfeld, L. L. (2019). Contribution of sensory encoding to measured bias. *Journal of Neuroscience*, *39*(26), 5115-5127.
71. Kastner, S., De Weerd, P., Desimone, R., & Ungerleider, L. G. (1998). Mechanisms of directed attention in the human extrastriate cortex as revealed by functional MRI. *science*, *282*(5386), 108-111.
72. Kim, M. H., Znamenskiy, P., Iacaruso, M. F., & Mrsic-Flogel, T. D. (2018). Segregated subnetworks of intracortical projection neurons in primary visual cortex. *Neuron*, *100*(6), 1313-1321.
73. Kondo, S., Yoshida, T., & Ohki, K. (2016). Mixed functional microarchitectures for orientation selectivity in the mouse primary visual cortex. *Nature communications*, *7*(1), 1-16.
74. Kravitz, D. J., Saleem, K. S., Baker, C. I., & Mishkin, M. (2011). A new neural framework for visuospatial processing. *Nature Reviews Neuroscience*, *12*(4), 217-230.
75. Kravitz, D. J., Saleem, K. S., Baker, C. I., Ungerleider, L. G., & Mishkin, M. (2013). The ventral visual pathway: an expanded neural framework for the processing of object quality. *Trends in cognitive sciences*, *17*(1), 26-49.
76. Krebs, W., & Krebs, I. P. (1989). Quantitative morphology of the central fovea in the primate retina. *American Journal of Anatomy*, *184*(3), 225-236.

77. Krieger, B., Qiao, M., Rousso, D. L., Sanes, J. R., & Meister, M. (2017). Fmy alpha ganglion cell types in mouse retina: Function, structure, and molecular signatures. *PloS one*, *12*(7), e0180091.
78. Kristensen, S., Garcea, F. E., Mahon, B. Z., & Almeida, J. (2016). Temporal frequency tuning reveals interactions between the dorsal and ventral visual streams. *Journal of cognitive neuroscience*, *28*(9), 1295-1302.
79. Kumano, H., & Uka, T. (2013). Responses to random dot motion reveal prevalence of pattern-motion selectivity in area MT. *Journal of Neuroscience*, *33*(38), 15161-15170.
80. La Chioma, A., Bonhoeffer, T., & Hübener, M. (2020). Disparity sensitivity and binocular integration in mouse visual cortex areas. *Journal of Neuroscience*, *40*(46), 8883-8899.
81. Levy, I., Hasson, U., Avidan, G., Hendler, T. & Malach, R. (2001). Center–periphery organization of human object areas. *Nat Neurosci* 4, 533–539.
82. López-Aranda, M. F., López-Téllez, J. F., Navarro-Lobato, I., Masmudi-Martín, M., Gutiérrez, A., & Khan, Z. U. (2009). Role of layer 6 of V2 visual cortex in object-recognition memory. *Science*, *325*(5936), 87-89.
83. Lu, Y., Yin, J., Chen, Z., Gong, H., Liu, Y., Qian, L., ... & Wang, W. (2018). Revealing detail along the visual hierarchy: neural clustering preserves acuity from V1 to V4. *Neuron*, *98*(2), 417-428.
84. Lui, L. L., Bourne, J. A., & Rosa, M. G. (2007). Spatial and temporal frequency selectivity of neurons in the middle temporal visual area of new world monkeys (Callithrix jacchus). *European Journal of Neuroscience*, *25*(6), 1780-1792.
85. Lyon, D. C., Nassi, J. J. & Callaway, E. M. A Disynaptic Relay from Superior Colliculus to Dorsal Stream Visual Cortex in Macaque Monkey. *Neuron, 65*, 270–279 (2010).
86. Mahon, B. Z., Kumar, N., & Almeida, J. (2013). Spatial frequency tuning reveals interactions between the dorsal and ventral visual systems. *Journal of cognitive neuroscience*, *25*(6), 862-871.
87. Manookin, M. B., Patterson, S. S., & Linehan, C. M. (2018). Neural mechanisms mediating motion sensitivity in parasol ganglion cells of the primate retina. *Neuron*, *97*(6), 1327-1340.
88. Maunsell, J. H., Nealey, T. A., & DePriest, D. D. (1990). Magnocellular and parvocellular contributions to responses in the middle temporal visual area (MT) of the macaque monkey. *Journal of Neuroscience*, *10*(10), 3323-3334.
89. Marshel, J. H., Garrett, M. E., Nauhaus, I. & Callaway, E. M. (2011).Functional Specialization of Seven Mouse Visual Cortical Areas. *Neuron, 72,* 1040–54.
90. Matsui, T. & Ohki, K. (2013).Target dependence of orientation and direction selectivity of corticocortical projection neurons in the mouse V1. *Front Neural Circuit, 7*, 143
91. McAdams, C. J., & Maunsell, J. H. (1999). Effects of attention on orientation-tuning functions of single neurons in macaque cortical area V4. *Journal of Neuroscience*, *19*(1), 431-441.
92. Merigan, W. H., & Maunsell, J. H. (1990). Macaque vision after magnocellular lateral geniculate lesions. *Visual Neuroscience, 5*(4), 347-352.
93. Merigan, W. H., & Maunsell, J. H. (1993). How parallel are the primate visual pathways?. *Annual review of neuroscience*, *16*(1), 369-402.
94. Metin, C., Godement, P., & Imbert, M. (1988). The primary visual cortex in the mouse: receptive field properties and functional organization. *Experimental brain research*, *69*(3), 594-612.
95. Mesa, N., Waters, J., & de Vries, S. E. (2021). The effect of inclusion criteria on the functional properties reported in mouse visual cortex. *Eneuro*, *8*(1).
96. Minderer, M., Brown, K. D., & Harvey, C. D. (2019). The spatial structure of neural encoding in mouse posterior cortex during navigation. *Neuron*, *102*(1), 232-248.

97. Mishkin, M., & Ungerleider, L. G. (1982). Contribution of striate inputs to the visuospatial functions of parieto-preoccipital cortex in monkeys. *Behavioural brain research*, *6*(1), 57-77.
98. Miyazaki, K., & Ross, W. N. (2015). Simultaneous sodium and calcium imaging from dendrites and axons. *Eneuro*, *2*(5).
99. Mohammed, A. I., Gritton, H. J., Tseng, H. A., Bucklin, M. E., Yao, Z., & Han, X. (2016). An integrative approach for analyzing hundreds of neurons in task performing mice using wide-field calcium imaging. *Scientific reports*, *6*(1), 1-16.
100. Movshon, J. A., & Newsome, W. T. (1996). Visual response properties of striate cortical neurons projecting to area MT in macaque monkeys. *Journal of Neuroscience*, *16*(23), 7733-7741.
101. Munk H. (1881) Ueber die Functionen der Grosshirnrinde. Gesammelte Mittheilungenaus den lahren. Berlin: Hirschwald;
102. Murgas, K. A., Wilson, A. M., Michael, V., & Glickfeld, L. L. (2020). Unique spatial integration in mouse primary visual cortex and higher visual areas. *Journal of Neuroscience*, *40*(9), 1862-1873.
103. Nakamura, H., Gattass, R., Desimone, R., & Ungerleider, L. G. (1993). The modular organization of projections from areas V1 and V2 to areas V4 and TEO in macaques. *Journal of Neuroscience*, *13*(9), 3681-3691.
104. Nauhaus, I., Nielsen, K. J., Disney, A. A. & Callaway, E. M. (2013). Orthogonal micro-organization of orientation and spatial frequency in primate primary visual cortex. *Nature Neuroscience* **15**, 1683–1690
105. Nauhaus, I. & Nielsen, K. J. (2014). Building maps from maps in primary visual cortex. *Curr Opin Neurobiol* **24**, 1–6
106. Nassi, J. J., Lyon, D. C. & Callaway, E. M. (2006).The Parvocellular LGN Provides a Robust Disynaptic Input to the Visual Motion Area MT. *Neuron* **50**, 319–327
107. Nassi, J. J., & Callaway, E. M. (2009). Parallel processing strategies of the primate visual system. *Nature reviews neuroscience*, *10*(5), 360-372.
108. Niell, C. M., and M. P. Stryker. 2010. “Modulation of Visual Responses by Behavioral State in Mouse Visual Cortex.” *Neuron*, *65*(4): 472–79.
109. Neitz, J. & Neitz, M. (2016).Evolution of the circuitry for conscious color vision in primates. *Eye* **31**, 286–300.
110. Obermayer, K., & Blasdel, G. G. (1997). Singularities in primate orientation maps. *Neural Computation*, *9*(3), 555-575.
111. Ohki, K., Chung, S., Ch’ng, Y. H., Kara, P. & Reid, C. R. (2005). Functional imaging with cellular resolution reveals precise micro-architecture in visual cortex. *Nature, 433*, 597–603
112. Ohzawa, I. Z. U. M. I., Sclar, G., & Freeman, R. D. (1985). Contrast gain control in the cat's visual system. *Journal of neurophysiology*, *54*(3), 651-667.
113. Olavarria, J., & Montero, V. M. (1989). Organization of visual cortex in the mouse revealed by correlating callosal and striate-extrastriate connections. *Visual neuroscience*, *3*(1), 59-69.
114. Orban, G. A., Van Essen, D., & Vanduffel, W. (2004). Comparative mapping of higher visual areas in monkeys and humans. *Trends in cognitive sciences*, *8*(7), 315-324.
115. Paik, S. B., & Ringach, D. L. (2011). Retinal origin of orientation maps in visual cortex. *Nature neuroscience*, *14*(7), 919.
116. Payne, B. R., & Berman, N. (1983). Functional organization of neurons in cat striate cortex: variations in preferred orientation and orientation selectivity with receptive-field type, ocular dominance, and location in visual-field map. *Journal of Neurophysiology*, *49*(4), 1051-1072.

117. Paxinos, G., & Watson, C. (2006). *The mouse brain in stereotaxic coordinates: hard cover edition*. Elsevier.
118. Pettet, M. W., & Gilbert, C. D. (1992). Dynamic changes in receptive-field size in cat primary visual cortex. *Proceedings of the National Academy of Sciences*, *89*(17), 8366-8370.
119. Perrone, J. A. & Thiele, A. (2001). Speed skills: measuring the visual speed analyzing properties of primate MT neurons. *Nature Neuroscience, 4*, 526–532
120. Piñon, M. C., Gattass, R., & Sousa, A. P. (1998). Area V4 in Cebus monkey: extent and visuotopic organization. *Cerebral cortex (New York, NY: 1991)*, *8*(8), 685-701.
121. Piscopo, D. M., El-Danaf, R. N., Huberman, A. D. & Niell, C. M. (2013). Diverse Visual Features Encoded in Mouse Lateral Geniculate Nucleus. *Journal of Neuroscience 33(*11), 4642–4656.
122. Polack, P. O., & Contreras, D. (2012). Long-range parallel processing and local recurrent activity in the visual cortex of the mouse. *Journal of Neuroscience*, *32*(32), 11120-11131.
123. Pollen, D. A., & Ronner, S. F. (1982). Spatial computation performed by simple and complex cells in the visual cortex of the cat. *Vision research*, *22*(1), 101-118.
124. Prado, J., Clavagnier, S., Otzenberger, H., Scheiber, C., Kennedy, H., & Perenin, M. T. (2005). Two cortical systems for reaching in central and peripheral vision. *Neuron*, *48*(5), 849-858.
125. Priebe, N. J., Lisberger, S. G. & Movshon, A. J. (2006).Tuning for Spatiotemporal Frequency and Speed in Directionally Selective Neurons of Macaque Striate Cortex. *Journal of Neuroscience 26(*11), 2941–2950
126. Rasmussen, R., & Yonehara, K. (2020). Contributions of Retinal Direction Selectivity to Central Visual Processing. *Current Biology*, *30*(15), R897-R903
127. Ravello, C. R., Perrinet, L. U., Escobar, M. J., & Palacios, A. G. (2019). Speed-selectivity in retinal ganglion cells is sharpened by broad spatial frequency, naturalistic stimuli. *Scientific reports*, *9*(1), 1-16.
128. Rhim, I., Coello-Reyes, G., Ko, H.-K. & Nauhaus, I. (2017).Maps of cone opsin input to mouse V1 and higher visual areas. *Journal of neurophysiology* ,*117*, jn.00849.2016
129. Paik, S. B., & Ringach, D. L. (2011). Retinal origin of orientation maps in visual cortex. *Nature neuroscience*, *14*(7), 919.
130. Ringach, D. L., Mineault, P. J., Tring, E., Olivas, N. D., Garcia-Junco-Clemente, P., & Trachtenberg, J. T. (2016). Spatial clustering of tuning in mouse primary visual cortex. *Nature communications*, *7*(1), 1-9.
131. Robson, J. G. (1966). Spatial and temporal contrast-sensitivity functions of the visual system. *Josa*, *56*(8), 1141-1142.
132. Roland, P. E., Geyer, S., Amunts, K., Schormann, T., Schleicher, A., Malikovic, A., & Zilles, K. (1997). Cytoarchitectural maps of the human brain in standard anatomical space. *Human brain mapping*, *5*(4), 222-227.
133. Rosa, M. G., & Elston, G. N. (1998). Visuotopic organisation and neuronal response selectivity for direction of motion in visual areas of the caudal temporal lobe of the marmoset monkey (Callithrix jacchus): middle temporal area, middle temporal crescent, and surrounding cortex. *Journal of Comparative Neurology*, *393*(4), 505-527
134. Rosenholtz, R. (2016).Capabilities and Limitations of Peripheral Vision. *Annu Rev Vis Sc 2*, 437–457
135. Roth, M. M., Helmchen, F. & Kampa, B. M. (2012). Distinct Functional Properties of Primary and Posteromedial Visual Area of Mouse Neocortex. *Journal of Neuroscience 32*(28), 9716–9726
136. Rust, N. C., Mante, V., Simoncelli, E. P. & Movshon, J. A. (2006). How MT cells analyze the motion of visual patterns. *Nat Neurosci 9*, 1421–1431

137. Saad, Z. S., Ropella, K. M., Cox, R. W., & DeYoe, E. A. (2001). Analysis and use of FMRI response delays. *Human brain mapping*, *13*(2), 74-93.
138. Saleem, A. B. (2020). Two stream hypothesis of visual processing for navigation in mouse. *Curr Opin Neurobiol* 64, 70–78
139. Sincich, L. C., & Horton, J. C. (2005). The circuitry of V1 and V2: integration of color, form, and motion. *Annu. Rev. Neurosci.*, *28*, 303-326.
140. Salinas, K. J., Velez, D. X. F., Zeitoun, J. H., Kim, H., & Gandhi, S. P. (2017). Contralateral bias of high spatial frequency tuning and cardinal direction selectivity in mouse visual cortex. *Journal of Neuroscience*, *37*(42), 10125-10138.
141. Schiller, P. H. (2010). Parallel information processing channels created in the retina. *Proceedings of the National Academy of Sciences*, *107*(40), 17087-17094.
142. Schuett, S., Bonhoeffer, T., & Hübener, M. (2002). Mapping retinotopic structure in mouse visual cortex with optical imaging. *Journal of Neuroscience*, *22*(15), 6549-6559.
143. Scholl, B., Burge, J., & Priebe, N. J. (2013). Binocular integration and disparity selectivity in mouse primary visual cortex. *Journal of neurophysiology*, *109*(12), 3013-3024.
144. Sengpiel, F., Stawinski, P., & Bonhoeffer, T. (1999). Influence of experience on orientation maps in cat visual cortex. *Nature neuroscience*, *2*(8), 727-732.
145. Shapley, R., & Perry, V. H. (1986). Cat and monkey retinal ganglion cells and their visual functional roles. *Trends in Neurosciences*, *9*, 229-235.
146. Shapley, R., Kaplan, E., & Soodak, R. (1981). Spatial summation and contrast sensitivity of X and Y cells in the lateral geniculate nucleus of the macaque. *Nature*, *292*(5823), 543-545.
147. Simoncelli, E. P. & Heeger, D. J. (1998) A model of neuronal responses in visual area MT. *Vision Research 38*, 743–761
148. Siegle, J. H., Ledochowitsch, P., Jia, X., Millman, D., Ocker, G. K., Caldejon, S., ... & de Vries, S. E. (2020). Reconciling functional differences in populations of neurons recorded with two-photon imaging and electrophysiology. *bioRxiv*.
149. Siegle, J. H., Jia, X., Durand, S., Gale, S., Bennett, C., Graddis, N., ... & Koch, C. (2021). Survey of spiking in the mouse visual system reveals functional hierarchy. *Nature*, *592*(7852), 86-9
150. Sit, K. K., & Goard, M. J. (2020). Distributed and retinotopically asymmetric processing of coherent motion in mouse visual cortex. *Nature communications*, *11*(1), 1-14.
151. Skottun, B. C. *et al.* (1991) Classifying simple and complex cells on the basis of response modulation. *Vision Research 31*, 1078–1086
152. Skottun, B. C. & Skoyles, J. R. (2011)On Identifying Magnocellular and Parvocellular Responses on the Basis of Contrast-Response Functions. *Schizophrenia Bull* **37**, 23–26 (
153. Snowden, R. J. & Hess, R. F. (1992).Temporal frequency filters in the human peripheral visual field. *Vision research 32*, 61–72
154. Solomon, S. G., Tailby, C., Cheong, S. K., & Camp, A. J. (2010). Linear and nonlinear contributions to the visual sensitivity of neurons in primate lateral geniculate nucleus. *Journal of neurophysiology*, *104*(4), 1884-1898.
155. Stephen, J. M., Aine, C. J., Christner, R. F., Ranken, D., Huang, M., & Best, E. (2002). Central versus peripheral visual field stimulation results in timing differences in dorsal stream sources as measured with MEG. *Vision Research 42*, 3059-3074.
156. Stirman, J. N., Smith, I. T., Kudenov, M. W., & Smith, S. L. (2016). Wide field-of-view, multi-region, two-photon imaging of neuronal activity in the mammalian brain. *Nature biotechnology*, *34*(8), 857-862.
157. Stirman, J. N., Townsend, L. B., & Smith, S. L. (2016). A touchscreen based global motion perception task for mice. *Vision research 127*, 74-83.

158. Szmajda, B. A., GrÜnert, U., & Martin, P. R. (2005). Mosaic properties of midget and parasol ganglion cells in the marmoset retina. *Visual neuroscience*, *22*(4), 395.
159. Tan, Z., Sun, W., Chen, T.-W., Kim, D. & Ji, N. (2015). Neuronal Representation of Ultraviolet Visual Stimuli in Mouse Primary Visual Cortex. *Scientific Reports 5*, 12597 (
160. Tian, L., Hires, S. A., Mao, T., Huber, D., Chiappe, M. E., Chalasani, S. H., ... & Looger, L. L. (2009). Imaging neural activity in worms, flies and mice with improved GCaMP calcium indicators. *Nature methods*, *6*(12), 875-881.
161. Tootell, R. B., & Taylor, J. B. (1995). Anatomical evidence for MT and additional cortical visual areas in humans. *Cerebral Cortex*, *5*(1), 39-55.
162. Traschütz, A., Zinke, W. & Wegener, D. (2012). Speed change detection in foveal and peripheral vision. *Vision Research* 72, 1–13
163. Tsao, D. Y., Freiwald, W. A., Knutsen, T. A., Mandeville, J. B. & Tootell, R. B. H. (2003).Faces and objects in macaque cerebral cortex. *Nature Neuroscience* 6, 989–995
164. Vaiceliunaite, A., Erisken, S., Franzen, F., Katzner, S., & Busse, L. (2013). Spatial integration in mouse primary visual cortex. *Journal of neurophysiology*, *110*(4), 964-972.
165. Valley, M. T., Moore, M. G., Zhuang, J., Mesa, N., Castelli, D., Sullivan, D., ... & Waters, J. (2020). Separation of hemodynamic signals from GCaMP fluorescence measured with wide-field imaging. *Journal of neurophysiology*, *123*(1), 356-366.
166. Van Essen, C. G., Schulson, E. M., & Donaghay, R. H. (1970). Electron Channelling Patterns from Small (10 μ m) Selected Areas in the Scanning Electron Microscope. *Nature*, *225*(5235), 847-848.
167. Van Essen, D. C. (1979). Visual areas of the mammalian cerebral cortex. *Annual review of neuroscience*, *2*(1), 227-261.
168. Van den Bergh, G., Zhang, B., Arckens, L., & Chino, Y. M. (2010). Receptive-field properties of V1 and V2 neurons in mice and macaque monkeys. *Journal of Comparative Neurology*, *518*(11), 2051-2070.
169. Vermaercke, B., Gerich, F. J., Ytebrouck, E., Arckens, L., Op de Beeck, H. P., & Van den Bergh, G. (2014). Functional specialization in rat occipital and temporal visual cortex. *Journal of neurophysiology*, *112*(8), 1963-1983.
170. Vermaercke, B., Van den Bergh, G., Gerich, F., & Op de Beeck, H. (2015). Neural discriminability in rat lateral extrastriate cortex and deep but not superficial primary visual cortex correlates with shape discriminability. *Frontiers in neural circuits*, *9*, 24.
171. Vinken, K., Vogels, R., & de Beeck, H. O. (2017). Recent visual experience shapes visual processing in rats through stimulus-specific adaptation and response enhancement. *Current Biology*, *27*(6), 914-919.
172. Wang, Q., & Burkhalter, A. (2007). Area map of mouse visual cortex. *Journal of Comparative Neurology*, *502*(3), 339-357.
173. Wang, Q., Gao, E. & Burkhalter, A. (2011).Gateways of Ventral and Dorsal Streams in Mouse Visual Cortex. *Journal of Neuroscience* 31(5), 1905–1918
174. Wang, Q., Sporns, O., & Burkhalter, A. (2012). Network analysis of corticocortical connections reveals ventral and dorsal processing streams in mouse visual cortex. *Journal of Neuroscience*, *32*(13), 4386-4399.
175. Wässle, H., Grünert, U., Röhrenbeck, J., & Boycott, B. B. (1990). Retinal ganglion cell density and cortical magnification factor in the primate. *Vision research*, *30*(11), 1897-1911.
176. Watanabe, M., & Rodieck, R. W. (1989). Parasol and midget ganglion cells of the primate retina. *Journal of Comparative Neurology*, *289*(3), 434-454.
177. Wood, R. J., & Schwartz, E. L. (1999). Topographic shear and the relation of ocular dominance columns to orientation columns in primate and cat visual cortex. *Neural networks*, *12*(2), 205-210.

178. Y-C, T., & Blakemore, C. (1976). Functional organization in the visual cortex of the golden hamster. *Journal of Comparative Neurology*, *168*(4), 459-481.
179. Yu, H. H., Verma, R., Yang, Y., Tibballs, H. A., Lui, L. L., Reser, D. H., & Rosa, M. G. (2010). Spatial and temporal frequency tuning in striate cortex: functional uniformity and specializations related to receptive field eccentricity. *European Journal of Neuroscience*, *31*(6), 1043-1062.
180. Zariwala, H. A., Borghuis, B. G., Hoogland, T. M., Madisen, L., Tian, L., De Zeeuw, C. I., ... & Chen, T. W. (2012). A Cre-dependent GCaMP3 reporter mouse for neuronal imaging in vivo. *Journal of Neuroscience*, *32*(9), 3131-3141.
181. Zhang, Y., Kim, I. J., Sanes, J. R., & Meister, M. (2012). The most numerous ganglion cell type of the mouse retina is a selective feature detector. *Proceedings of the National Academy of Sciences*, *109*(36), E2391-E2398.
182. Zhuang, J., Ng, L., Williams, D., Valley, M., Li, Y., Garrett, M., & Waters, J. (2017). An extended retinotopic map of mouse cortex. *Elife*, *6*, e18372.